Emission and conduction properties of nano-needle diamond under ultra-short laser illumination : Study by field-effect microscopy and energy spectroscopy

Mario Borz

THÈSE

Pour obtenir le diplôme de doctorat

Spécialité Physique

Préparée au sein de « Groupe de Physique de Matériaux, UMR 6634, CNRS, Normandie Université »

Propriétés d'émission et de conduction de nano-pointe de diamant sous éclairement laser ultra-bref. Étude par microscopies à effet de champ et spectroscopie en énergie

Présentée et soutenue par
Mario BORZ

Thèse soutenue publiquement le 21 novembre 2019 devant le jury composé de		
M. Anthony Ayari	Directeur de Recherche, Institut Lumière Matière, Lyon	Rapporteur
M. Arnaud Arbouet	Directeur de Recherche, CEMES, Toulouse	Rapporteur
M. Benoit Chalopin	Maitre de Conférences, Université Paul Sabatier, Toulouse	Examinateur
M. Hamed Merdji	Directeur de Recherche au CEA, Saclay	Rapporteur ou Examinateur, ou Directeur de thèse ou Codirecteur de thèse
M. Bernard Deconihout	Professeur, Université de Rouen	Examinateur
M. Ammar Hideur	Professeur, Université de Rouen	Codirecteur de thèse
Mme. Angela Vella	Professeur, Université de Rouen	Directeur de thèse

Thèse dirigée par Angela VELLA et Hammar HIDEUR, laboratoire GPM et CORIA

UNIVERSITÉ DE ROUEN NORMANDIE

ED PSIME

GPM Groupe de Physique des Matériaux

Acknowledgments

First of all, I would like to express my deepest gratitude to my supervisors Professor Angela Vella and Professor Ammar Hideur. Without their guidance and their encouragements this thesis would have not been possible. They motivated me to work, to improve myself thanks to their deeply knowledge in the research field and through their passion for science. I learned many important lessons and values while working by their side, each day. With their kind hearts, they guided me in both my professional and personal life.

I would also like to thank the member of my jury for spending their valuable time reading my dissertation and attending to the public defense expressing a strong interest through many questions and a proficient discussion after my thesis presentation: Professors Anthony Ayari, Arnaud Arbouet, Benoit Chalopin, Hamed Merdji and Bernard Deconihout.

I am deeply grateful to the GPM laboratory and the University of Rouen for the warm hospitality in these three years. Furthermore I would like to thank our collaborators Professor Alexander Obraztsov, Viktor I. Kleshch for the sample preparation and their contribute in our publications. Also thanks to the LCAR of Toulouse where I spent a period of study: thanks to Benoit Chalopin, Julien Mauchain and Olivier Torresin for welcoming me and working together with passion and curiosity. Thanks to the members of the Coria laboratory: Ammar Hideur and Saïd Idlahcen for the laser system used in the experiments and their immeasurable help. Thanks to the member of the équipe d'instrumentation scientifique: Angela Vella, Ivan Blum, Jonathan Houard, Gerald Da Costa and Laurent Arnoldi for the work done together and their teachings.

Finally, I would like to thank my family: my mother, my father, my sister Michela and my girlfriend Anna. They always supports me, gives me courage in the pursuit of my dreams. A special thanks to my friends in Rouen and in the university with whom I spent my free time during this PhD years: Roger, Anas, Linda, Federica, Alip, Kamal, Rhea, Christian, Sahar, Elena, Danut, Mary Kathryn, Rafat.

Résumé

Le but de cette thèse est de comprendre les changements dans les propriétés électriques et optiques des matériaux à large bande interdite à l'échelle nanométrique par rapport au matériau massif et en présence d'un champ électrique statique intense.

Le diamant en forme de nano-aiguille a été choisi comme matériau d'étude en raison de sa large bande interdite, sa haute résistance aux contraintes externes et sa conduction thermique élevée. Le diamant présente également une résistance électrique élevée, ce qui en fait un bon candidat pour l'étude des modifications de conduction électrique sous des champs électriques et optiques forts.

Afin d'étudier les propriétés de conduction électrique, deux différentes techniques expérimentales ont été utilisées : la microscopie ionique à effet de champ et la microscopie électronique à effet de champ avec et sans éclairement laser. Les observations expérimentales ont été couplées à des modèles de conduction électrique qui décrivent qualitativement et quantitativement les résultats obtenus.

Pour l'étude des propriétés optiques, une microscopie électronique à émission de champ assistée par laser a été réalisée. Dans ce cas, l'étude a été menée dans deux configurations expérimentales : l'une en éclairant l'ensemble de l'échantillon par le faisceau laser et l'autre en focalisant le laser uniquement sur le sommet de la nano-pointe où le champ électrique est augmenté et les électrons sont émis dans le vide.

Les résultats décrivent les propriétés de conduction électrique et d'émission d'électrons des nano-aiguilles de diamant dans l'obscurité et sous un éclairement laser. En tant qu'émetteurs d'électrons, les nano-aiguilles de diamant présentent des avantages par rapport aux pointes métalliques telles qu'une stabilité d'émission et un seuil de dommage plus élevés sous éclairement laser.

Les résultats sont prometteurs pour le développement d'une nouvelle source de photoélectrons pour la microscopie électronique résolue en temps.

Emission and conduction properties of nano-needle diamond under ultra-short laser illumination. Study by field-effect microscopy and energy spectroscopy.

Mario Borz

21/11/2019

Abstract

The aim of this thesis is to understand the changes in the electrical and optical properties of large band-gap materials at the nanoscale in the presence of a huge static electric field.

Diamond nano-needle has been chosen as a study material, thanks to its wide band gap, high resistance to external stress and high thermal conduction. Diamond presents also high electrical resistance, making it a good candidate for the study of electrical conduction modifications under high electric and optical fields.

In order to study the electrical conduction properties, two different experimental techniques were used: Field Ion microscopy and Field Emission Microscopy with and without laser illumination. The experimental observations were coupled with electrical conduction models which describe qualitatively and quantitatively the obtained results.

For the study of the optical properties, laser-assisted Field Emission Microscopy was performed. In this case, the study was performed in two experimental configurations: one by illuminating the whole sample by the laser beam and the other by focusing the laser beam only on the apex of the nano-tip where the electric field is enhanced and the electrons are emitted into vacuum.

The results describe the electrical conduction and electron emission properties of the diamond nano-needles in dark and under laser illumination. As field emitters, diamond nano-needles show advantages compared to metallic tips such as: higher emission stability and higher damage threshold under laser illumination.

The results are promising for the development of novel photo-electron sources for time-resolved electron microscopy.

Contents

List of Figures

Introduction

The work reported in this thesis has been done in the Groupe de Physique des Materiaux (GPM – Group of the physics of materials) laboratory of the university of Rouen (Normandie, France). In particular, I have been assigned in the Equipe de Recherche en Instrumentation Scientifique (ERIS - scientific instrumentation research group), where the Atom Probe Tomography (APT) is studied and developed in order to improve the performance of this technique.

In 2004, the Laser assisted Atom Probe Tomography (La-APT) was developed in ERIS. This powerful technique allows the 3D imaging of nanoscale tips, subjected to a high potential and illuminated by ultrashort laser pulses. The APT needs high electric fields (around 10 V/nm) to be able to evaporate atoms from the surface of the sample as ions. To reach such high electric fields, the samples are prepared in a tip geometry with a nano-metric radius of curvature at the apex to achieve large field enhancement. In the standard APT, the tip is biased by a voltage close to the voltage needed for evaporation while electric pulses are sent on the apex for the purpose of triggering the ion evaporation. Instead, in La-APT, ultrashort laser pulses (below the picosecond pulse duration) are used instead of electric pulses to trigger the evaporation process, with the objective of overcoming the poor transmission of electric pulses in low-conductive materials. These two types of signals (electric or laser pulses) are also used as a reference for the time of flight measurement of the evaporated ions in order to obtain their chemical nature, through time of flight mass spectroscopy. In the case of La-APT, laser pulses increase the apex temperature to achieve atom evaporation.

La-APT presents some limitations in the analysis of non-conductive materials due to two main factors: the poor electrical conductivity of this kind of materials and their low absorption of the laser power. In fact, as predicted by theoretical works, in case of poor electrical conduction, the electric field at the apex of the sample will be reduced drastically by field penetration rendering analysis by APT impossible. The other main problem is related to laser absorption. Since dielectric and insulating materials present a wide band gap, they do not absorb photons with energy lower than their band gap. Thus, these kinds of materials are transparent to laser radiation with energy in the near-

ultraviolet and visible. Without photon absorption, the tip temperature cannot rise and the evaporation cannot take place.

Contrary to theoretical predictions, experimental results showed that La-APT analysis is still possible on semiconductor materials and oxides. So, the aim of this work was to try to understand what factors can influence the feasibility of the analysis. In particular, to see if this type of materials, manufactured in nanoscale shape and under the APT experimental conditions, could work better in term of electrical conduction and optical absorption than the "bulk". In fact, thanks to the high surface to volume ratio exhibited by nano-sized materials, the electrical conduction and the laser absorption can be strongly dependent on the surface states. Moreover, these kinds of material are usually prepared by Focused Ion Beam (FIB) in order to obtain the needed shape and size for APT analysis. This kind of preparation leads to surface amorphization which creates plenty of surface defects.

The ideal material to investigate these mechanisms would be a dielectric which presents low electric conductivity as well as a wide bang gap for a low light absorption coefficient in the visible and UV range. The material that we choose is single crystal chemical vapor deposited diamond. It was provided by our collaborators from the Department of Physics of the M.V. Lomonosov Moscow State University, which prepared the diamonds already in a needle shape with nano-metric apex size, ready for APT and field emission microscopies. These samples are prepared without the use of FIB milling, so the surface is free of implanted surface defects which are not related to the material itself. Diamond is also a challenging material for APT due to its strong covalent bonds between atoms which increases the evaporation field. On the other hand, diamond presents high resistance to the stress induced by high electric field and has good thermal conductivity which reduces the problem related to thermal heat propagation during La-APT analysis. At last, due to its low electric conductivity, the change of the electrical conduction under high electric field and laser illumination can be easily studied.

The first objective for this work has been the study of electrical conduction properties of these diamond nano-needles. The geometric shape of the sample and its nano-metric size affects the electrical conduction as well as its behavior under high electric field compared to the bulk material. In order to perform this study, two different techniques have been used.

The first one is Field Ion Microscopy (FIM) where gas atoms are ionized by the intense electric field present on the apex of the sample. The ions are then accelerated by the field itself toward the detector in order to create a 2D image of the surface of the apex of the sample. Measuring the ion current one can get information about the current flowing through the sample, which is orders of magnitude higher than the current of APT

analysis. Controlling the gas pressure or the applied voltage, a wide range of currents can be explored for the study of the resistivity effects. Moreover, the ultra-fast laser can be used to illuminate the tip during measurements. The illumination conditions can be changed by changing the laser wavelength and power to study the effect of the laser on the conduction mechanisms involved.

The second technique for the study of electrical conductivity is Field Emission Microscopy (FEM) where a negative bias is applied to the sample in order to emit electrons into vacuum. Also for this technique, the sample has to have a nano-metric radius of curvature at the apex to enhance the electric field for electron emission. With the emission of electrons, it is possible to probe even higher and wider range of currents. The FE setup has been used in two detection configuration, using a high-resolution energy spectrometer (Argus Spectrometer) and using a retarding field energy analyzer, which is able to provide a two-dimensional information of the emission pattern thanks to the use of a CCD camera. The Argus spectrometer has been used in static regime (no laser illumination) for the study of the energy spectrum of the emitted electrons while the implementation of the 2D detector has enabled the possibility of monitoring the emission pattern changes between static and laser illuminated regimes.

The second objective of this thesis has been the study of the optical properties of diamond. In more details, the absorption of the laser light induces an increase of temperature which can reach the threshold necessary for ion evaporation in APT. As described in literature, the physical properties can be affected by the presence of the strong electric field necessary for analysis.

Again, two different setups have been used. The first one consists in the use of the laser illumination in the FIM set-up. In this set-up, the laser spot size is large enough to illuminate the whole sample or the major part of it. This allows the study of optical absorption in the part of the sample where the effective electric field is low compared to the effective electric field present at the apex of the sample.

The second setup is the FEM. In this setup, the laser has been used in two configurations, one where the laser is "weakly" focused as in the FIM case to illuminate the majority of the sample and one where the laser is "strongly" focalized on the apex of the tip in order to investigate the illumination effects on the part of the sample where the electric field is enhanced and electrons are emitted into vacuum.

In this context, the FIM analysis allows to highlight the contribution of the defects present inside the material to photons absorption and thus to the change of electrical conduction, while the use of FE leads to point out the multi-photonic effects taking place at the apex of the tip.

In this framework, the correlation between light-matter interaction with the changes

in the conduction mechanisms has been studied in this kind of environment (nano-objects and high electric field). Furthermore, using FEM, the diamond nano-needles have been characterized for the first time as electron field emitters under ultra-fast laser illumination.

This thesis is organized as follows:

Chapter 1 introduces diamond as a material, describing its crystallographic and band structure. The different conduction mechanisms which can participate in electric conduction in dielectrics are discussed including the case where a metal/dielectric junction is present. Then the optical and thermal properties of diamond are introduced before the discussion of its use as electron field emitter. At the end, the diamond growth fabrication process is described.

Chapter 2 describes the experimental setups used in this work. This includes tungsten tip preparation for the calibration of the instruments as well as the diamond sample preparation for analysis. Then, the FIM FlexTAP setup is described in its usage as a conduction measurement tool. Afterward, the FEM setup is introduced along with the two different detection systems, as well as their calibration. Then, the field emission from tungsten tip, in static and under laser illumination is described and discussed for the validation of the experimental setups.

Chapter 3 presents the conduction study performed on the diamond tips with the use of FIM and FEM techniques. In particular, the study of the I-ΔV characteristics in low and high current regimes both in dark and under the laser illumination is presented. The role of the geometry of the diamond samples in the conduction mechanisms is discussed. Conduction models are introduced in order to explain the various factors which influence the current flowing through the samples.

Chapter 4 presents the study of the field emission characteristic of diamond samples. This study has been performed with and without laser illumination and for different beam focalization conditions.

Chapter 1

Electrical and optical properties of diamond and its application as a field emitter

In this chapter, diamond is the main subject of discussion. In particular, we will discuss its physical properties which can lay a role in the case of electron field emission, such as crystal and band structure, electrical conduction mechanisms and its thermal properties. Moreover, we present a general discussion of field emission from diamond field emitters, with a particular attention on studies on diamond needles made by our collaborators, who provided us the diamond needles studied in this work of thesis. At the end of this chapter, the diamond needle fabrication will be addressed.

1.1 Diamond: general information

Carbon (diamond's element), silicon (Si), germanium (Ge) and grey tin (Sn) are all elements which belong to the IV group of the periodic table. These elements have half filled valence n-shells in the electronic configuration (ns^2p^2) where n range from 2 to 5. This s and p states hybridize forming tetrahedral sp^3 bonds. The solid resulting from these elements can crystallize in the so called "diamond cubic" structure [1]. This structure is a face-centered cubic (fcc), with two identical atoms in the coordinates 000 and $\frac{1}{4}\frac{1}{4}\frac{1}{4}$ associated to each point of the lattice, as shown in Figure 1.1. Each atom has 4 nearest neighbors and 12 next-nearest neighbors with a lattice constant of $a = 6.49$ Å.

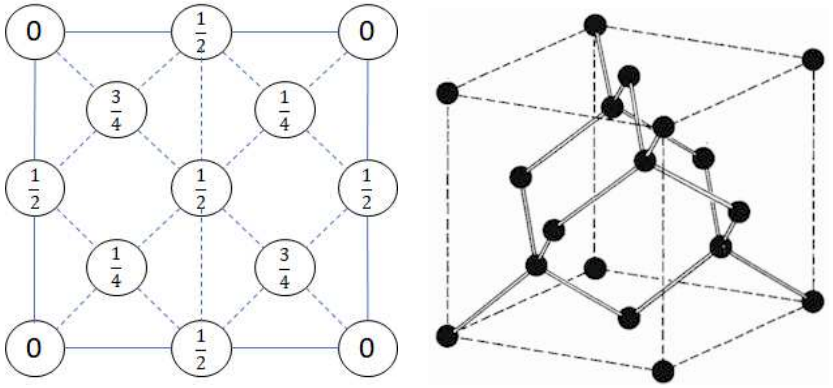

Figure 1.1: On the left the atomic position in the cubic cell of the diamond structure projected on a cube face. Points 0 and $\frac{1}{2}$ are from the fcc lattice while $\frac{1}{4}$ and $\frac{3}{4}$ are in a similar lattice displaced diagonally by one-forth of its length. All lattice points are filled with identical C atoms. On the right, crystal structure of diamond, showing the tetrahedral bond arrangement.

Si and Ge are well known in this form as useful semiconducting materials for device applications. On the other hand, diamond present the strongest atom bonding, which results in extraordinary hardness, high thermal conductivity and high melting temperature. It has a bulk modulus of $4.4 \cdot 10^{11}\ N/m^2$(about 4 times the value for Si) [2]. Furthermore it presents high thermal conductivity, for example the value $410\ W/cm \cdot K$ has been measured for single crystal diamond at $104\ K$, which is the highest thermal conductivity above liquid nitrogen temperature measured [3]. These attractive features drive much experimental efforts to grow different form of diamond like crystals, films and nano-objects.

1.1.1 Electronic band structure

In Figure 1.2, the electronic band structure of bulk diamond is shown, calculated along several symmetry directions. In relation to the valence band (VB), as one can see the crystal presents four valence bands. The lower bands are characterized by primarily s-like states and the upper valence states are p-like with a hybridization in the middle range reflecting the sp^3 bonding. On the other hand, the minimum of the conduction band (CB), which is empty, is located at a different k point from the Γ point ($\vec{k} = (0, 0, 0)$), where the maximum of the VB is situated. This comports that diamond is a material with indirect band gap. This is in agreement with experimental measurements such as optical constant measurements which shows and indirect gap of $E_g = 5.5\ eV$ [4].

The magnitude of the band gap is generally reflected to the bonding properties of the solid since the gap reflects the difference in energy between the bonding and anti-bonding states. Compared to Si and Ge (energy gap of $1.1\ eV$ and $0.76\ eV$ respectively), the

diamond gap of $5.5\,eV$ is a signature that the bonding is more ionic than Si and Ge. One reason is the fact that the p states of diamond penetrate into the 1s region, causing a more attractive potential from the nucleus. This penetration of p states has been proved by the charge densities founded using a pseudo-potential calculation [5].

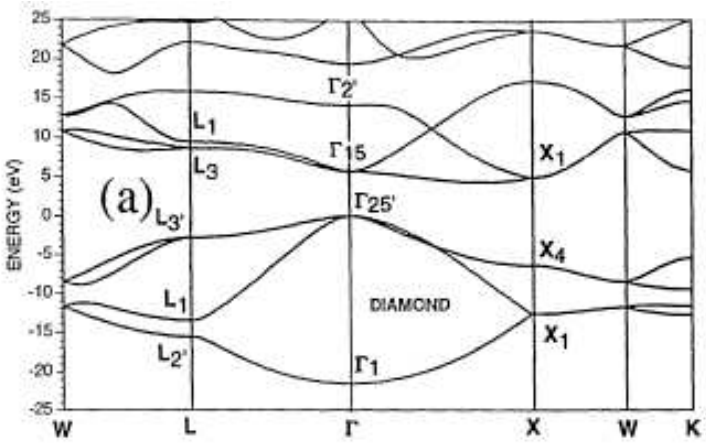

Figure 1.2: Band structure of diamond calculated along several symmetry directions.

1.2 Electrical conductivity of dielectrics

Diamond belongs to the family of dielectrics, which are wide band gap materials (in general above 3 or $5\,eV$) with tightly bonded electrons, presenting low electrical conductivity. They have a full valence band and an empty conduction band at $0\,K$. Above $0\,K$, some electrons are promoted into the CB and they will contribute to the current transport of the material. In a similar way, holes are generated by acceptor impurities leaving vacancies that are left by the excited electrons in the valence band. In general, dielectrics present low electric conductivity (of the order $10^{-20} \sim 10^{-8}\,\Omega^{-1}cm^{-1}$). However, under an intense electric field the current which flows through low dimension dielectric systems is not negligible. In literature, there are many mechanism which explain the flow of charges inside these systems. In the case of dielectrics, the flowing current can be limited by two different factors: the junction of contact between the dielectric material and the metal which is called injection-limited conduction mechanism and the properties of the dielectric itself which are called bulk-limited conduction mechanisms. In some cases, more than one conduction mechanism contributes to the general current which flows in the system [6].

1.2.1 Junction limited conduction mechanisms

The category of injection-limited conduction mechanism includes:

- Schottky (or thermionic) emission;
- Fowler-Nordheim tunneling;
- Thermionic-field emission.

1.2.1.1 Schottky emission

Thermionic field emission consists in a current which is assisted by the lowering of the potential barrier thanks to the electric field in the case of high temperature electrons. The carriers are injected from the metal electrode into the bulk of the dielectric and follow the Schottky theory:

$$J = AT^2 exp\left(-\frac{\varphi - \beta E^{1/2}}{k_B T}\right) \tag{1.1}$$

where A is a constant independent of the electric field E, φ the work function of the dielectric and β is given by:

$$\beta = \left(\frac{e^3}{4\pi\varepsilon_0\varepsilon_r}\right)^{1/2} \tag{1.2}$$

where ε_0 is the permittivity of vacuum and ε_r the optical dielectric constant (or dynamic) of the material, measured at high frequencies. The optical dielectric constant is chosen instead of the static one. This is due to the fact that if the electron transit time from the metal/dielectric interface to the maximum position of the barrier is shorter than the relaxation time, the dielectric does not have enough time to be polarized. The optical dielectric constant is usually smaller compared to the static one since there are more polarization mechanisms which can contribute to the total polarization [7].

The second part of the exponential represents the decrease of the work function in the presence of the applied electric field. According to Equation 1.1, the plot of $ln\,(J/T^2)$ as a function of $E^{1/2}$ gives a straight line where the intercept is the pre-exponential factor and the slope is the term in brackets. Figure 1.3 shows the energy band diagram with a metal/dielectric junction with the metal under negative bias. This mechanism is one of the most observed in dielectrics film, especially at high temperature.

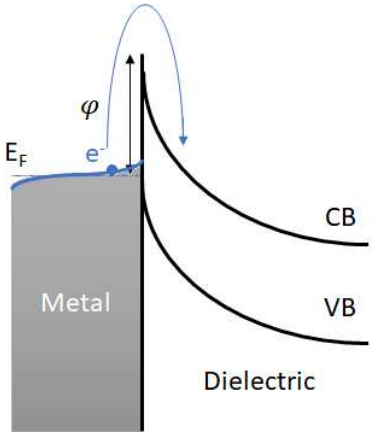

Figure 1.3: Schematic energy band diagram of Schottky emission in a metal/dielectric junction.

1.2.1.2 Fowler-Nordheim tunneling

In a quantum mechanics point of view, an electron wave function can penetrate and pass through a potential barrier if it is thin enough. In this picture, the tunnel probability is not zero. Figure 1.4 shows the schematic diagram of Fowler-Nordheim (FN) tunneling. FN tunneling takes place under high electric field in order to reduce the barrier width, which can be approximated by a triangular barrier, so that electrons can tunnel through. This theory is also widely used in order to explain the field emission of electrons into vacuum from metals. The expression of FN tunneling is given by:

$$J = \frac{e^3}{8\pi h}\frac{E^2}{\varphi} exp\left(-\frac{8\pi(2em_e)^{1/2}}{3h}\frac{\varphi^{3/2}}{E}\right) \tag{1.3}$$

where e is the electron charge and m_e is the electron mass. At low temperature, when the thermionic emission is suppressed, one can obtain the tunneling current using the current-voltage characteristic $(I-V)$ of the device. In the case of FN tunneling, plotting the $ln(J/E^2)$ as a function of $1/E$ results in a linear dependence.

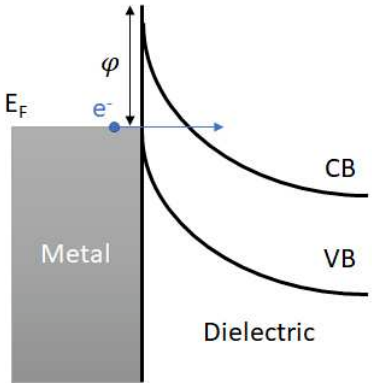

Figure 1.4: Schematic energy band diagram of Fowler-Nordheim tunneling in a metal/dielectric junction.

1.2.1.3 Thermionic field emission

Thermionic field emission is a regime where FN and Schottky emission take place at the same time. In this intermediate regime, electrons have an energy which is between the Fermi level and the CB edge. In this energetic state they tunnel into the CB of the dielectric through FN tunneling (Figure 1.5).

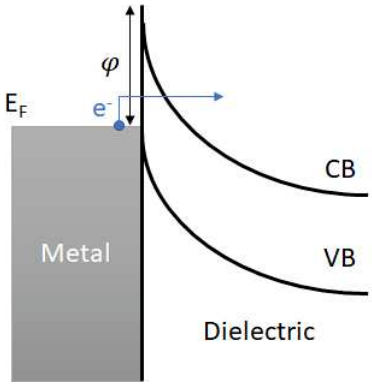

Figure 1.5: Schematic energy band diagram of thermionic-field tunneling in a metal/dielectric junction.

1.2.2 Bulk-limited conduction mechanisms

These types of conduction mechanisms are dependent on the electrical properties of the dielectric itself.

The bulk limited conduction mechanisms are:

- Ohmic conduction;
- hopping conduction;
- space-charge-limited conduction;
- ionic conduction;
- grain-boundary limited conduction;
- Poole-Frenkel conduction.

1.2.2.1 Ohmic conduction

Ohmic conduction is due to the movement of free carriers in the CB and of holes in the VB of the material. This conduction is characterized by a linear dependence of the current with the applied electric field. Even though the band gap of dielectric is large, there will be still a small number of carriers that can be generated by thermal excitation. These electrons can be excited from the VB directly or through impurity levels. The current density can be expressed as:

$$J = \sigma E = n_e e \mu E,\ n = N_C exp\left(-\frac{E_C - E_F}{k_B T}\right) \tag{1.4}$$

where σ is the electrical conductivity, n_e the number of free electrons, μ the electron mobility and N_C the density of states of the conduction band. The magnitude of this current, being the energy gap ($E_g = E_C - E_F$) high, is very small. So that this type of mechanism is visible when there are not other mechanisms which contribute to the global conduction.

1.2.2.2 Hopping conduction

Hopping conduction mechanism describes the tunneling of trapped electrons jumping from a trap site to another inside the dielectric. In Figure 1.6, the schematic energy band diagram for hopping conduction is shown. This type of mechanism can be described with:

$$J = qan_e v\, exp\left(\frac{qaE - E_a}{K_B T}\right) \tag{1.5}$$

where E is the electric field, a is the mean hopping distance, n_e the carrier density in the CB, v the electrons frequency of thermal vibration in the trap sites and E_a is the activation energy. The carrier energy is lower than the barrier between two adjacent traps, but they still contribute to the current through tunneling. The activation energy can be determined by an Arrhenius plot at low electric field and the trap spacing can be obtained by the slope of the linear part in the plot of log(J) as a function of E [8].

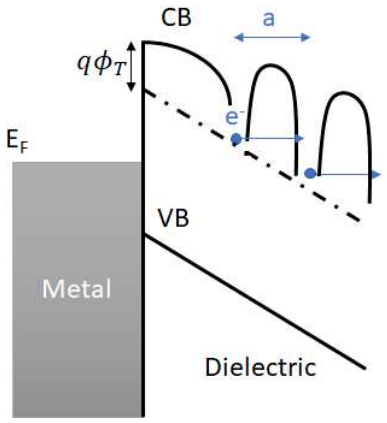

Figure 1.6: Energy band diagram of hopping conduction in a metal-dielectric structure.

1.2.2.3 Space charge limited conduction

Space charge limited conduction mechanism (SCLC) is similar to the transport mechanism present in vacuum diodes. In this case, the carrier are injected from the metal/dielectric junction. In order to SCLC to occurs, the Ohmic contribution has to be small. This can be described saying that the relaxation time of the dielectric has to be large compared to the transit time of the injected carriers in order for the carriers to not decay significantly during the transit and so, to be able to travel across the dielectric. Therefore, a strong injection of carriers is necessary to fill up the traps and observe SCLC (Child's law) [9].

The main factor which limits this type of conduction is the presence of trapping levels, which trap electrons nullifying their contribution to the total current. The plot of the J-V characteristic in log J-log V scale shows three different regimes (Figure 1.7). At low applied voltage, the characteristic is of the Ohmic type ($J_{Ohmic} \propto V$), at intermediate voltage, the SCL current is limited by trap filling (TFL) ($J_{TFL} \propto V^2$) and at high applied voltage, the Child's law ($J_{Child} \propto V^2$) appears. Between the TFL and the Child's law regime a sharp increase of the current takes place.

These three regimes can be described with:

$$J_{Ohmic} = en_0\mu\frac{V}{d} \tag{1.6}$$

$$J_{TFL} = \frac{9}{8}\mu\varepsilon\theta\frac{V^2}{d^3} \tag{1.7}$$

$$J_{Child} = \frac{9}{8}\mu\varepsilon\frac{V^2}{d^3} \tag{1.8}$$

where n_0 is the concentration of free carriers in thermal equilibrium and θ is the ratio between the free carrier density and the total carrier density (free and trapped).

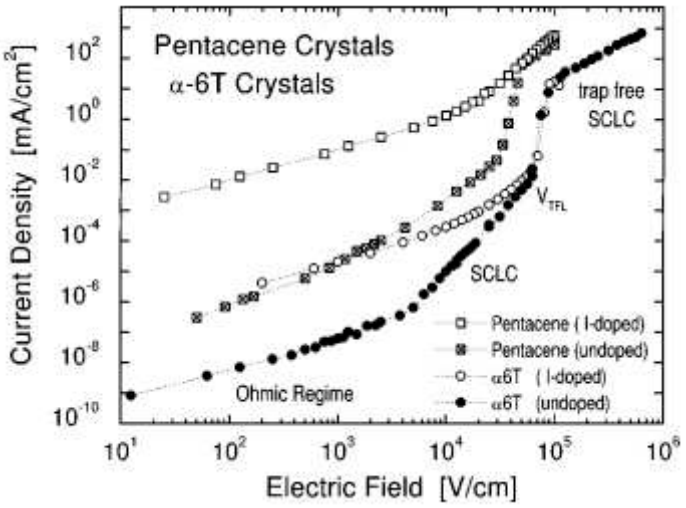

Figure 1.7: Current density vs applied electric field for conduction perpendicular to the surface in unopened and iodine-doped pentacene and a-6T single crystals. SCLC stands for trap filling limited (TFL) while trap free SCLC stands for Child's law. Figure taken from [10].

1.2.2.4 Ionic conduction

Ionic conduction describes the movement of ions under an applied electric field. These ions can derive from lattice defects in the dielectric. The effect of the electric field on these defect energy levels is the hopping of ions which move jumping from one defect to another. This ionic current can be describe as:

$$J = J_0 exp\left(\frac{qaE}{2K_BT} - \frac{q\phi_B}{k_BT}\right) \tag{1.9}$$

where J_0 is a proportional constant, E the electric field, $q\phi_B$ is the potential barrier height and a is the spacing between two adjacent defects. Since the mass of ions is huge

compared to the one of electrons, the ionic current is usually negligible compared to electronic currents.

1.2.2.5 Grain-Boundary-Limited Conduction

In a poly-crystalline material, the resistivity of grain boundaries (GB) could be higher than the one of the grains. In this case, the current could be limited by the presence of the boundaries [11]. This can be described with the use of a potential energy barrier at the GB (Φ_B) which is inversely proportional to the relative dielectric constant. This barrier can be described as:

$$\Phi_B = q\phi_B = \frac{q^2 n_b^2}{2\varepsilon_r N} \tag{1.10}$$

where n_b is the GB trap density and N the dopant concentration. The dielectric constant plays a significant role on the potential energy barrier at the GB.

1.2.2.6 Poole-Frenkel conduction

Poole-Frenkel conduction (PF) is a conduction mechanism similar to Schottky emission, where electrons bonded to trap levels can escape in the CB thanks to thermal excitation. If one considers an electron in a trapping center, the presence of an electric field can reduce the Coulomb potential energy increasing the possibility of its thermal excitation in the CB of the dielectric. In Figure 1.8, the diagram of PF conduction is shown. In the case of a Coulomb attraction potential for an electron in a trap site, the PF mechanism can be described as:

$$J = e\mu N_C E \, exp\left(\frac{-(e\phi_{PF} - \beta_{PF}\sqrt{E}}{k_B T}\right) \tag{1.11}$$

where $N_C$is the density of states in the CB, $e\phi_{PF}$ (Φ_{PF}) is the barrier height of the trap potential and $\beta_{PF} = \sqrt{e^3/\pi\varepsilon_0\varepsilon_r}$ is the barrier lowering coefficient. Since this mechanism implies the thermal activation under electric field, this mechanism is often observed at high temperature and high electric field. The trap potential energy can be obtained through an Arrhenius plot ($log(J/E)$ as a function of $1/T$). On the other hand, plotting the I-V characteristic in the so called "PF coordinates" ($log(J/E)$ as a function of $E^{1/2}$), one can obtain information about the relative dielectric constant ε_r of the material.

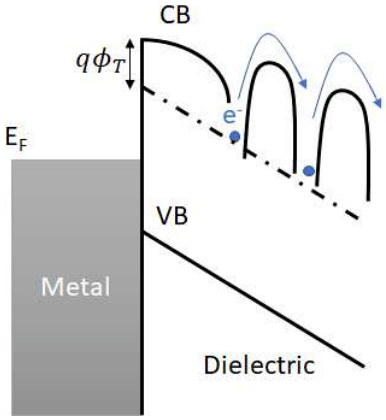

Figure 1.8: Energy band diagram of Poole-Frenkel conduction in a metal-dielectric structure.

1.3 Diamond optical properties

Despite its large band gap ($\sim 5.5\,eV$), diamond can absorb light in the UV, visible and IR spectral regions as a results of the presence of defects, impurities [12].

This defects and impurities in diamond can be in the form of vacancies, substitutional atoms, self-interstitial carbon atoms or interstitial impurities. These impurities and defects are associated with a relaxation of the surrounding atoms in the lattice. These crystal defects and impurities can create discrete levels in the band gap of the material which are the responsible for the optical properties of diamond. In the ideal case, without defects, the band gap is too large for UV and lower frequencies photons to excite electronic transitions.

In general, the main impurities are nitrogen and boron atoms, and their concentration can be controlled in the manufacturing process of synthetic diamond. The importance of these type of defect is clear since they control distinct features in the optical absorption spectra and by the fact that the classification of diamond has two major types of diamond (I and II) based on these impurity levels by Robertson et al. [13].

So, all diamonds are luminescent under irradiation with luminescence spectra presenting many features characteristic of the types of defects involved. Table 1.1 summarizes the main luminescent peaks reported in literature [14, 15, 16].

Position	Name	Comment
>5.5 eV (<225 nm)	Band edge	Indirect gap, observable in defect-free diamond
5.26 eV (236 nm)	band-B nitrogen	four N atoms on substitutional sites symmetrically surrounding a vacancy
4.582 eV (270 nm)	5RL system	interstitial carbon atoms
3.188 eV (389 nm)		an interstitial carbon atom and a nitrogen atom
3.1-2.5 eV (400-496 nm)	band-A nitrogen	a nearest neighbor pair of substitutional nitrogen atoms
2.985 eV (415 nm)	N3 system	three nitrogen atoms on a (111), or three nitrogen atoms surrounding a vacancy
2.499 eV (496 nm)	H4 system	vacancies trapped at nitrogen B-centers
2.463 eV (503 nm)	H3 system	vacancies trapped at nitrogen A-centers
2.156 eV (575 nm)		a vacancy and a nitrogen atom
1.945 eV (637 nm)	NV system	a vacancy trapped at a substitutional nitrogen atom
1.681 eV (738 nm)		defects involving Si impurities and associated vacancies, observed mostly in CVD diamond
1.673 eV (741 nm)	GR1 system	neutral vacancies
1.267 eV (979 nm)	H2 system	negatively charged H3 center

Table 1.1: Major Photo-Luminescence (PL) peaks observed in diamond.

1.4 Diamond thermal properties

In opposition of electrical insulator and wide band gap dielectrics, diamond is known as a good conductor of heat thanks to its strong covalent bonds and low photon scattering. Natural diamond thermal conductivity is measured to be more or less $2200\,W/(m \cdot K)$. This value is higher than five times the thermal conductivity of silver, which is the most thermally conductive metal. In the case of mono crystal diamond, the measured thermal conductivity has been measured above $3000\,W/(m \cdot K)$ at room temperature, while the value increases decreasing the temperature until liquid nitrogen temperature [17].

In a study which precedes this work, a measure of the thermal properties of the diamond nano-needle analyzed during this PhD thesis has been done [18]. The thermal diffusivity found in this work is of $5.5 \pm 0.5\,cm^2/s$ which corresponds to a thermal con-

ductivity of about $1000 \pm 100\, W/(m \cdot K)$ for a temperature below $250\, K$. These values are lower than the bulk case and are in agreement with theoretical prediction on nano-wires [19].

1.5 Diamond in field emission applications

One of the most exciting application of diamond is as electron field emitter. In particular, dielectrics which exhibit negative electron affinity (NEA) surfaces can potentially be used as field-emitters and cold cathodes. Since the field emission depends exponentially on the barrier height, low electron affinity materials are desirable [20].

As may be in the case of diamond, band bending at the surface could lead to the formation of a NEA as shown in Figure 1.9. The energy bands are bent at the surface due to the presence of surface states [21]. The internal excitation and transport properties of the bulk material are not affected since the band bending occurs over tens angstroms from the surface. In the case of NEA, if an electron can diffuse to the surface, it will leave the material freely.

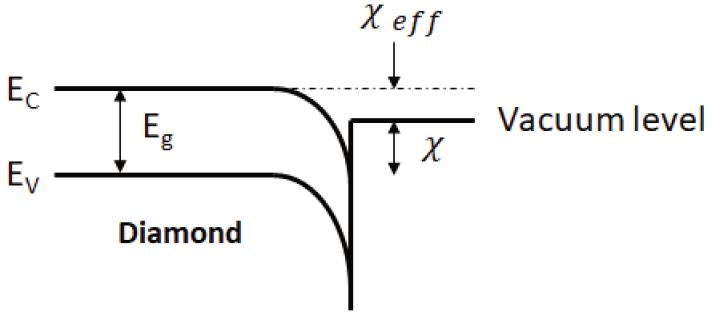

Figure 1.9: Energy diagram in the case of a negative electron affinity due to band bending at the surface.

Field emission from diamond is widely studied, in particular in the case of single crystal, poly-crystalline diamond, diamond like films and diamond coated metallic emitters. Low-field emission from diamond films deposited by chemical vapor deposition (CVD) was observed, without external excitation at electric field lower than $3V/\mu m$ where $5V/\mu m$ are required in the case of tungsten emitters [22]. Furthermore, the field emission from metals degrades in performance. This degradation speed is proportional to the pressure level, where higher pressure corresponds to faster degradation in the emission current. Instead, diamond cold cathodes have been shown to exhibit improved performance in presence of oxygen at a pressure of 0.1 *mbar* [24]. In this picture, diamond cathode devices are promising candidates for robust electron emitters.

Diamond emitters are studied in various forms and crystalline configurations, such as polycristalline diamond or deposited diamond film on substrates. In the work of O. Groning et al., CVD diamond films are shown to be of the Fowler-Nordheim field emission type [24]. In this study, the films are not uniform and the electron emission at low electric field is attributed to the presence of local enhancement due to the inhomogeneous surface structure. So, in the case of deposited diamond films, the rough inhomogeneous surface leads to non-reproducible results due to a wide range of enhancement factors which can take place and different conduction mechanisms. Furthermore, the presence of oxygen and hydrogen treated surfaces (positive and negative electron affinity respectively) does not impact the emission characteristics.

Other studies use diamond as a coating material for classic metal field emitters. In the study carried out by R. Schlesser et al. [25], molybdenum nano-tips coated with undoped diamond have been used. In this case, the emitters resulted in an emission instability and multiple competing emission sites. To overcome this problem, the diamond-coated tips had to sustain an annealing process to reduce the emission threshold along with site competition and increase the emission current stability.

These works show that the surface structure and properties are of vital importance in order to have controlled emission characteristic and reproducibility. In this sense, a protocol in order to grow single crystal CVD diamond needles has been developed by the group of the Department of Physics of the M.V. Lomonosov Moscow State University under the supervision of Professor Alexander Obraztsov. With these samples, the surface characteristics of these needles are more controllable compared to previous works.

1.5.1 CVD diamond needle for field emission

The static field emission from diamond needles has been study by V. I. Kleshch et al. [25]. From the measure of electron kinetic energy and emission current they evinced that the conduction mechanism is of the Poole-Frenkel type. In PF conduction the coefficient β_{PF} of Equation 1.11 can be related with the relative dielectric coefficient of the material ($\varepsilon_r = 9.2$ and 9.6 for two emitters) in the assumption of constant electric field along the axis of the sample. Moreover, they studied the current emission characteristic as a function of the temperature. The current emission tends to saturate at high applied voltages like predicted for the case of non-metallic emitters, due to the penetration of the electric field at the apex which creates a depletion region limiting the emission current [26]. The saturation region of the emission current of Figure 1.10a, according to the theory, is sensitive to external excitation, such as a light source or temperature. The $I - V$ characteristics measured at different temperatures from 300 K to 900 K are reported in Figure 1.10a.

Moreover the current as a function of the inverse of the temperature at constant applied voltage, in Arrhenius coordinates, shows a linear behavior. The slope of the Arrhenius plot is connected to the activation energy of the trap potential of the diamonds ($E_a = \phi_{PF} - \beta_{PF}\sqrt{\Delta V}$).

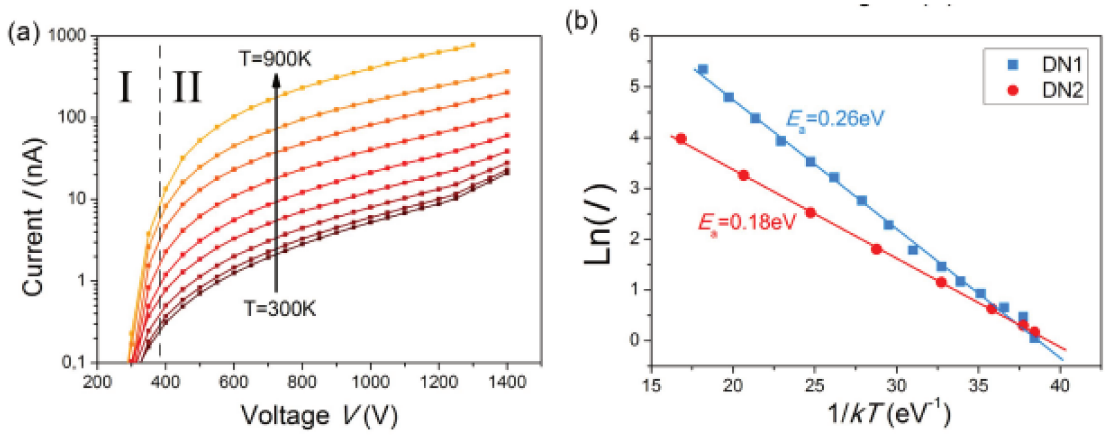

Figure 1.10: Temperature dependence of field emission from a diamond needle: (A) $I-V$ characteristic plotted in semi-log scale; (b) Arrhenius plot of the emission current from two diamond needles at 700 V.

V. Porshyn et al. discussed the electron emission stimulated by laser pulses of about 3.5 ns with a photon energy ranging from 5.9 eV to 3.1 eV [27]. The laser was illuminating the back side of the Silicon wafer which supports the diamond needle with an illumination intensity below 200 kW/cm^2. This laser, with a photon energy of 5.9 eV, led to a pronounced increase of current emission as shown in Figure 1.11. This linear dependence of the emission current as a function of the laser pulse intensity is the signature of the photo-assisted field emission in the diamond needles[28, 29]. However, non linear absorption should be visible for laser intensities in the tenths of GW/cm^2range.

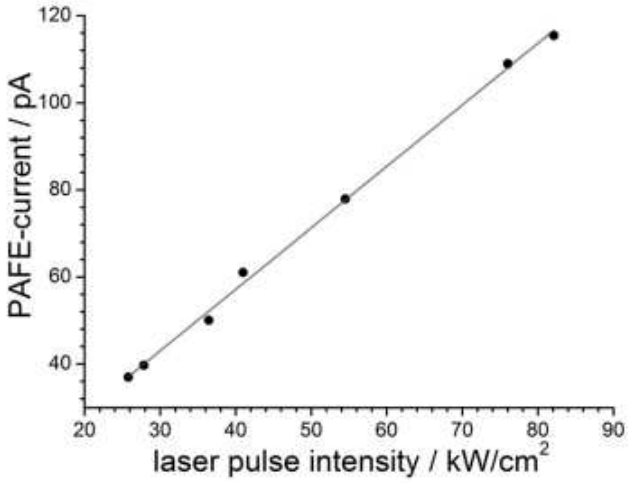

Figure 1.11: Emission current as a function of the laser pulse intensity at an applied voltage of 500 V and a photon energy of 5.9 eV; PAFE stands for photo-assisted field emission.

1.6 Single crystal CVD diamond needles growth process

As said above, single crystal diamond needles have been studied in this thesis work. Our samples were supplied by the team of Professor Alexander Obraztsov of the Department of Physics of Moscow State University. The fabrication process of these diamond needles is widely discussed and explained in literature [30]. These diamond needles are growth by plasma enhanced chemical vapor deposition (PE-CVD). This process consists in the growth of a diamond film on standard silicon (100) wafer. This growth process makes the formation of a poly-crystalline (001) textured diamond film. The substrate is heated up to about 900 $°C$ in a chamber with total pressure of 9.5 kPa with a gas mixture composition $CH_4 : CH_2 = 5 : 95$ with a discharge voltage of about 700 V and discharge current of about 1 A/cm^2 [31]. The duration of this process depends on the desired thickness of the film (and the diamond crystalline length). After growth, the film is thermally oxidized to remove selectively the smallest diamond crystallites, nano-diamond fraction, disordered carbon and graphitic inclusions. This thermal oxidation is made at 650 $°C$ in air for about 2 hours and its schematically shown in Figure 1.12.

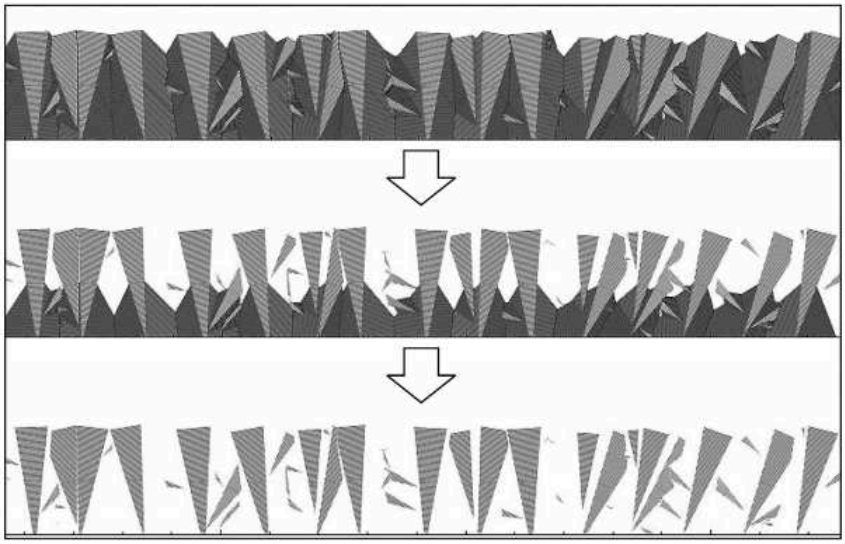

Figure 1.12: Images showing simulation results of the CVD diamond film growth and their selective oxidation.

As a result, single crystal diamonds which remain after oxidation are in a needle shape with a length of up to $> 100\,\mu m$ with a pyramid-like geometry with an apex radius of curvature below the $200\,nm$ and with the axis oriented along the (001) crystallographic direction (Figure 1.13).

Figure 1.13: SEM image of the diamond needles after selective oxidation of the (001) textured polycristalline CVD film.

1.7 Conclusion

In this chapter, an introduction about diamond has been done. In particular about the physical properties of diamond, such as its crystallography properties, electronic band structure, thermal conduction properties. After that, we introduced the main mechanisms which can play a role in the electrical conduction inside dielectrics material with a metal/dielectric junction. Afterwards, we discussed the general characteristics of field emission properties from diamond, in details the studies reported in the literature on field emission from diamond needles analyzed in this work of thesis. To conclude, the method of these diamond needle fabrication has been described.

Chapter 2

Experimental setup and methods

This chapter describes the experimental setups used in this thesis dedicated to field-ion spectroscopy and electron emission spectroscopy. Before the beginning of this thesis, the setup for field-ion spectroscopy was already working in well calibrated conditions for semiconductors and oxides samples. However, the experimental setup for electron emission spectroscopy was not finished, the laser was not installed yet and a new electron detector has just arrived to the laboratory (Argus CU, `www.scientaomicron.com/en/products/344/1110`). After the analysis with the Argus spectrometer, the detector for electrons has been replaced by a retarding field energy analyzer (Low-Energy Electron Diffraction (LEED)), in order to add the 2D pattern of emission to the measurements, which is a key point in our study since the emission pattern is strongly modified under laser illumination.

In this work, tungsten tips have been used as reference for electron emission and for calibration of the electron-energy spectrometers. In the first part of this chapter the samples preparation will be discussed, then the setup for field ion microscopy (FIM) will be described and at the end the field emission microscopy (FEM) setup will be presented with the various detecting systems (Argus spectrometer and LEED). The laser characteristics as well as the sample alignment with the LEED and laser focusing conditions will be detailed. At the end, preliminary results with tungsten will be discussed.

2.1 Nano-tips fabrication and preparation

Tungsten tips has been used for calibration of the setup, since it is a well studied material in field electron emission and field-ion evaporation experiments.

Tungsten (W) is a widely used material as an electron source in various applications, so it is one of the best candidates to calibrate and test instruments. Tungsten is a metal with high melting point, $3695\,K$, ideal for field emission applications with a work function of $\sim 4.7\,eV$.

The W tips are made by electrochemical etching, where a W wire (0.1 mm of diameter, oriented to the [011] direction) is immersed in a solution (0.3% of $NaOH$ in H_2O). Applying a voltage of some volts ($3\,V$) on the solution the wire dissolves until a sharp tip is formed. Using this method, various radius of curvature at the apex of the samples can be obtained (between 10 to $300\,nm$) as well as various cone angle of the tip. With this method, sharp tips have been obtained with their apex oriented in the [011] direction.

2.1.1 Diamond samples preparation for analysis

In order to perform analysis, the diamond needles must be mounted on W wires supports for the analysis chamber. The preparation of the W supports use the same method as for the W nano-wires, but keeping a bigger radius of curvature ($\geq 500\,nm$) for easier attachment of the diamond needles and to avoid electron emission from the W instead of the diamond.

In order to attach the diamond needles on the W wires two main methods have been used:

- glue the needles with the use of a Silver Conductive Epoxy glue using a micro-manipulator under an optical microscope.
- weld the needles using platinum deposition through the use of a nozzle present inside a Scanning Electron Microscope (ZEISS - NVISION40).

The first method, since is done using an optical microscope, has low yield because the microscope is not powerful enough in order to see the radius of curvature of the apex, which in the majority of the cases is bigger than the necessary for electron emission at relatively low voltages. This makes the search for a good candidate for analysis tedious, requiring a long time of sample preparation. Furthermore, the characterization in a Transmission Electron Microscope of the needles to measure the radius of curvature, as well as other geometrical factors (length, cone angle and shape), of the prepared samples is needed 24 hours after in order for the glue to solidify enough for vacuum applications.

On the other hand, the welding with platinum method inside the SEM have the advantage of the possibility of the choice of the needle from the substrate and the platinum weld makes the sample more resistant to the electrostatic stress when the tips are put under high electric fields in FIM and FEM applications. Another pro of the platinum weld, compared to the epoxy glue, is the fact that the sample can sustain temperature above $100\,°C$ during experiments. The drawback of the platinum welding is the time it takes and its complexity. To weld a diamond needle to the tungsten support, the use of a micro-manipulator is necessary, in order to lift the needle from the substrate. To do the lifting, a small platinum weld between the needle and the micro-manipulator is necessary. Afterwards, with the micro-manipulator, the diamond tip is aligned to the tungsten pre-tip support and welded on it. The final stage of the process consists in pulling the micro-manipulator away from the pre-tip in order to break the little weld on the micro-manipulator and leaving the diamond sample on the pre-tip of tungsten. This pulling phase of the process is very risky with the consequence of a possible break of the weld and lose of diamond sample.

2.2 Field Ion Microscope: FlexTAP instrument

A big part of the study of the electrical conduction mechanism in CVD diamond has been done with the use of the Field Ion Microscopy technique. In particular, the instrument used is the so called FlexTAP produced by CAMECA. The particularity of this setup, compared to classical APT machines, is the presence of electrostatic lenses in a vacuum chamber with a flight path much longer than standard machines. These lenses have the function of modulating the ion trajectories inside the chamber in order to have a wide collecting angle (up to 30°) over a long flight time in order to improve the time of flight resolution.

The sample inside the chamber is fixed on a cryogenic device allowing to control its temperature which can be set in the range from 20 to 100 K. The pressure inside the chamber is in the order of $10^{-10}\,mbar$ for APT measurements and a positive bias up to $15\,kV$ can be applied to the sample.

Furthermore, a femto second laser can be used during experiments. This laser has the fundamental wavelength $\lambda = 1030\,nm$ at $50\,kHz$ (at $100\,kHz$ in FIM mode) with a Gaussian pulse duration of about $500\,fs$. In order to generate higher laser frequencies in the visible ($515nm$) and UV ($343nm$) regions, respectively, doubling and tripling processes in nonlinear crystals are used (second and third harmonic generation). The laser beam is polarized on the axis of the tip inside the chamber and focused with external lenses obtaining around $50\,\mu m$ laser beam diameter measured at a radius of $1/e^2$.

The chamber, long 57 *cm* (44 *cm* sample-detector distance in FIM mode), is equipped with electrostatic lenses for the deflection of the ion trajectories (Figure 2.1).

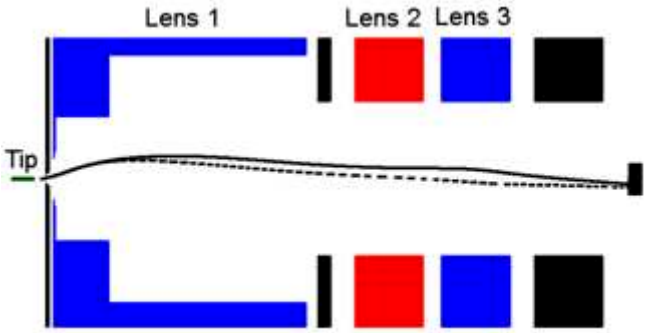

Figure 2.1: Schema of the FlexTAP instrument with numerically simulated ion trajectories for a field of view of 30° in FIM mode. Ions are emitted from the tip at an angle of 12°. Full (dashed) lines correspond to ion trajectories without (with) energy deficit. The relative energy deficit is 2%. The optical elements in black are at the ground potential.

Depending on the voltage applied on the sample, different setting parameters allow to have different angles of view on the detector form (4 to 30°) as well as an increased time of flight that increases with the voltage applied on the first electrode (retarding potential). In FIM mode, different types of gases can be chosen as imaging gas, such as helium, neon and hydrogen. In the scope of this thesis, FlexTAP has been used only in FIM mode, with the use of He gas, at a field of view of 30° and all the three available laser wavelengths have been explored.

As will be discussed in Chapter 3, there are two different methods to measure the energy deficit of the emitted ions. In the case of a non-metallic sample, when there is a flow of current, there is a difference of potential between the base of the tip, where the voltage is applied and the apex of it. This potential difference is translated in a deficit in the kinetic energy of the gas ions generated by the electric field present at the apex. So, the energy deficit is the same amount as the voltage drop that occurs in the analyzed sample.

The first one is based on the simulation of the ions trajectories and aims in the calculation of the ratio between the radius of the image with the radius of the detector. This method is suitable for the measure of low energy deficit up to 5% respect to the applied voltage in the wide field of view of the instrument at 30° (Figure 2.2). In fact, in the presence of a low energy deficit, the electrostatic lenses of the FlexTAP which have the scope of adapting the ions trajectories to arrive on the whole surface of the detector, make the ions to impact the detector not on all its surface but on a circular surface with a lower radius. The ratio between the radius of the image and the radius of the detector gives an

indication of the voltage drop present on the analyzed sample as shown in Figure 2.2.

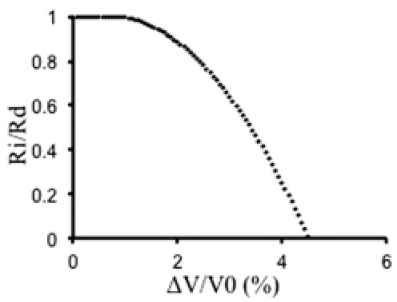

Figure 2.2: Ratio between the radius of the light zone over the radius of all the detector in function of the voltage drop on the apex of the sample.

The second method, where the lenses 2 and 3 are at ground potential, consists in the measure of the minimum applied potential on the retarding lens of the instrument in order to completely block the arrival of ions on the detector (Figure 2.3). This method, on the contrary of the first one, is more suitable in the study of high voltage drops which are higher than the 5% limit of the first method. The potential on the apex of the sample V_{apex} is proportional to the minimum voltage on the retarding lens V_{lens} in order to stop the arrival of the gas ions on the detector: $V_{apex} = V_{applied} - SV_{lens}$where S is a calibration factor. The procedure to obtain the S factor consists in the use of a tungsten tip in FlexTAP using only the first retarding lens, since in the case of metals there is no voltage drop between the base and the apex. At a given applied voltage, the voltage for the cut-off of the ions arrival on the detector is $V_{cut-off} = SV_{applied}$.

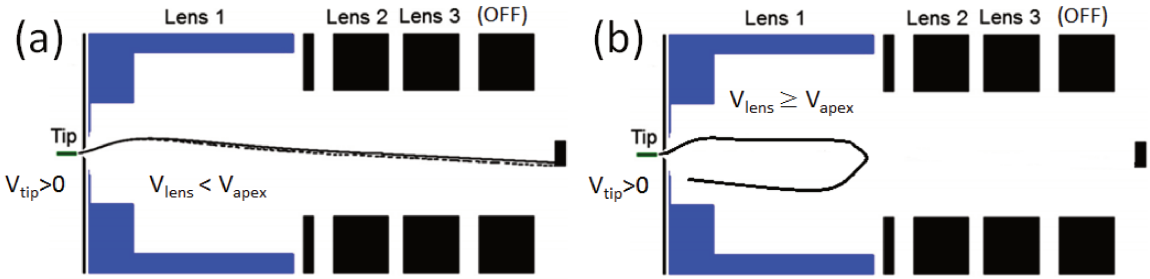

Figure 2.3: (a) FlexTAP schematic where the voltage on the retarding lens is not sufficient to stop the arrival of ions on the detector. (b) The voltage on the lens is high enough and the ions are repulsed back and do not reach the detector anymore.

For the measurements of current flowing through the samples, at first a pico-amperometer (Keithley model 6485 with a $0.4\,\% + 400\ fA$ accuracy in the $2\ nA$ range) has been connected to a grounded ring placed in front of the sample, in order to measure the current generated by the passage of emitted ions, which is the opposite of the current flowing

inside the sample. Unfortunately, this method was not successful because the signal from the ion emission was below the background noise level of the instrument. Therefore, the pico-amperometer has been connected to the phosphorous screen of the FIM detecting system. The pico-amperometer had to be put in floating mode with the use of a transformer since the voltage applied on the phosphorous screen is about 3000 V. With this setup, the exact value of the current cannot be measured, since the gain on the micro-channel plates (MCPs) is unknown, but still, the right trend of the current curve is obtained. The measured current will be higher than the real one flowing through the specimen due to the amplification of the MCPs. This measure has been carried out with the electrostatic lens in the configuration of 30° field of view in order to maximize the current signal.

2.3 Field Emission Microscope

The measurement in FEM mode where made in a spherical vacuum chamber with a pressure between $10^{-9}\ mbar$ and $4 \cdot 10^{-10}\ mbar$. The value of the pressure inside the chamber is very important to minimize sample pollution during electron emission. In fact, a good vacuum pressure is necessary to avoid fast surface contamination on the nano-tip and prevent ionization of particles caught in the laser focus.

The vacuum chamber uses a turbomolecular pump to maintain the pressure and a titanium sublimation pump is used every time the chamber has to been open to the atmospheric air, as well as a baking process. With the use of a cold finger it is possible to cool down the sample to around 80K using liquid nitrogen, while a temperature regulator can set the temperature from 80K to above ambient temperature.

Inside the chamber, the sample is mounted on a micro-manipulator with the ability of moving the tip in all direction (x,y and z). With the use of the micro-manipulator, the tip can be positioned in the correct position required by the various spectrometers and in the focus of the laser beam. For convention, since field emission takes place at negative applied voltages on the samples, the voltages reported in the FEM case are written omitting the minus sign.

2.3.1 Argus detector

The first analyses carried out in the FEM workbench were made with the use of the Argus Spectrometer made by Scienta Omicron (`www.scientaomicron.com/en/products/344/1110`). At the time, the laser system was not available yet, so only measures in dark regime were carried out. This hemispherical analyzer, made for x-ray photo-spectroscopy on flat sample hit by x-ray, presents a $124mm$ mean radius 180° double focusing geometry, with a 128 channels detector equipped with micro-channel plate electron multipliers and a stripe anode detector and 128 individual counters (Figure 2.4).

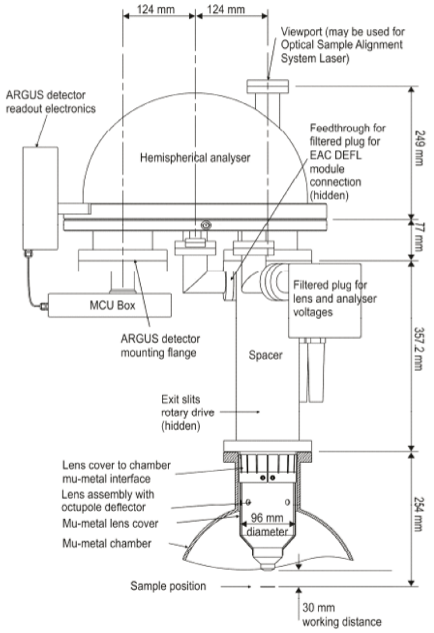

Figure 2.4: Argus Spectrometer schematic with label of the main properties of the detector.

As one can see from Figure 2.4, the detector collects electrons and focus them on the entrance of the hemispherical energy analyzer. It can also accelerate and decelerate the electrons with the use of the entrance lenses and can provide different magnifications and angular acceptances. The in-lenses have also the function to scan the focal point in the plane of the working distance. The entrance lenses and the aperture can be set to allow only a specified cone angle of emission directions. The band pass of the detector can be set in order to count only the electrons which have their kinetic energy in this interval. Furthermore, the detector does not count all the arriving electrons but only a fraction, which is called detector efficiency (between 60 and 80%). In detail, the input lenses collect electrons focusing them onto the aperture and simultaneously adjust their kinetic energy to match the pass energy of the analyzer.

The instrument can operate in two different modes:

- Constant Analyzer Energy (CAE), where the retard lens voltages change to ensure that the electrons enter with the same energy as the pass energy, allowing the hemisphere voltage to remain constant (constant pass energy).
- Constant Retard Ratio (CRR), where the retard lens voltages change in such a way that the kinetic energy of the electrons is reduced by the same fraction while the hemisphere voltage changes to keep the pass energy equal to the kinetic energy of the electrons (not constant pass energy).

With this setup, it is possible to acquire emission energy spectra with an energy interval from 100 eV up to 2000 eV. The drawback of using such a detector, since nano-tips can be considered as point sources for this kind of analyzer, is the fact that a change in the emission pattern of the emitted electrons can lead to a loss of signal. So it is not possible to acquire the 2D pattern emission of the samples. The implementation of laser illumination leads to a significant change of the emission pattern of the sample making the use of this type of detector ineffective for laser assisted field emission.

2.3.1.1 Data acquisition and analysis

With the detector, the software for the use of the analyzer and for the extraction of the data has been provided by Scienta Omicron. For electron spectroscopy measurements we used the so-called software MATRIX. This software allows user to acquire energy spectra and scan images of the emitted electrons. Since our samples are seen as point sources for this type of detector, the 2D scan image system was mainly used in the search of the emitting sample.

The main feature of our interest is the ability of energy spectra acquisition. In particular, with the use of MATRIX, one can acquire multiple spectra at different electron energies which range from 50 eV up to a maximum of 2000 eV. The other parameters which can be set are the energy step (minimum of 0.01 eV), the dwelling time for each measurement point (minimum 10 ms), the magnification mode: low, medium and high which influences on the collecting angle and the mode of acquisition (CAE or CRR) with its resolution. In our case, since the electron emission of the samples is restricted to a limited window of energies of few eV, the best operating mode is CAE since it doesn't modify the resolution with the change of the electron kinetic energy.

Once a sample is ready to be analyzed, since in the case of diamond the emission energy is not known, scans of a wide range of energies are done changing the position of the tip in the xy plane at each acquisition in order to find the correct position of emission as well as the energy of the electrons. Once this is done, scans around the emission energy

are done at higher resolution (low CAE) for the best resolution possible. This process has to be repeated for every applied voltage.

In our case, the acquired emission spectra are also used to study the I-V characteristics. Through the measure of the energy of the Fermi level from the spectra, since it is directly linked to the voltage present on the apex of the sample, being $eV_{apex} = E_F$ where e is the electron charge and E_F is the electron energy of the Fermi level, the measurement of the voltage at the apex is possible. On the other hand, the emission current is directly proportional to the integral of the emission spectrum taking into account the acceptance angle of the spectrometer and the efficiency (between 60 and 80%). Knowing the acquisition parameters, through the emission spectra, the total amount of emitted electrons can be obtained. This value scales proportional with the real emission current.

2.3.1.2 Detector calibration

Since the Argus Spectrometer was a new detection system, a calibration work had to be done in order to validate the measurement procedure and the fidelity of the results obtained with this instrument. In order to do this, tungsten (W) tips have been analyzed since W is a widely studied material for field emission, useful for the validation of the experimental set-up.

Knowing the field emission theory from metals, from the energy emission spectrum it is possible to obtain information about the tunnel probability $\propto exp(C_V \cdot K_E)$ which can be used in order to estimate the spectrometer resolution taking into account that the rising part of the spectrum is related to the tunnel probability of electrons into vacuum and the sharp cut-off at high energy is due to the Fermi-Dirac distribution (F-D) [33]. In the tunnel probability expression:

$$C_V = 2\left(\frac{2me}{\hbar}\right)^{1/2}\frac{\varphi^{1/2}}{E}t(y) \sim 10.25 \cdot 10^9 \frac{\varphi^{1/2}}{V_{apex}\beta} \tag{2.1}$$

where m is the electron mass, φ the emitter work function, E the electric field and β the tip enhancement factor. In Equation 2.1, the effective mass of electron is taken as the free electron one, and with the approximation of the elliptical function $t(y) = 1$ since it slowly varies with y ($t(y)$ is a tabulated function, see Table 1.1 of [34]).

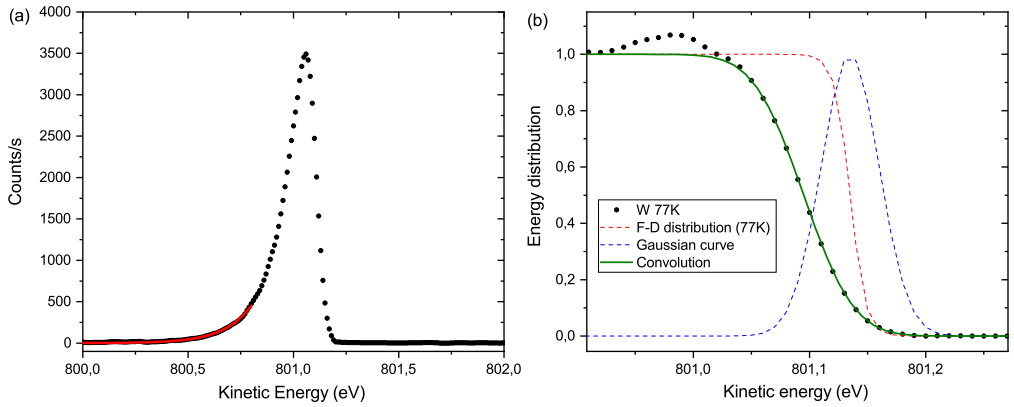

Figure 2.5: (a) Field emission energy spectrum from a tungsten tip of radius $r \sim 70\,nm$ taken at around $V_{applied} = 801\,V$ (FWHM: full-width at half maximum of $0.17 \pm 0.04\,eV$). The red line is the fit of the tunnel probability using the Equation $B \cdot exp(C_V \cdot K_E)$. (b) Density of occupied states calculated from the experimental data of (a). The short dash line represents the F-D distribution at $77\,K$ and the dash line represents a Gaussian distribution which takes into account the spectrometer resolution. The fit in full line is the convolution of the F-D and Gaussian distributions with a spectrometer resolution $a = 40\,meV$.

Normalizing the energy spectrum with the tunneling probability, obtained with a fit on the low energy part of the spectrum (Figure 2.5a), the density of occupied electron states close to the Fermi energy of the emitter can be obtained, see plot points in Figure 2.5b, obtained for a tungsten tip cooled down at around $80\,K$ using liquid nitrogen. It has the typical shape of the F-D distribution. The spectrometer resolution is here taken into account through a Gaussian distribution $exp(-K_E^2/a^2)$ where a is the spectrometer resolution (dashed lines in Figure 2.5b). The density of occupied states of Figure 2.5b (dot points) is then fitted with a convolution of the F-D distribution $\frac{1}{e^{(K_E - E_F)/k_B T}}$ at $77\,K$ (short dash line in Figure2.5b) and the Gaussian distribution. The best fit obtained for a spectrometer resolution of $a = 40\,meV$ is reported in Figure2.5b by a full line.

2.3.2 LEED detector

In preview of a future use of a femto-second laser on the field emission workbench, the Argus Spectrometer has been replaced by a Low-Energy Electron Diffraction (LEED) spectrometer. The schema of this detector is shown in Figure 2.6.

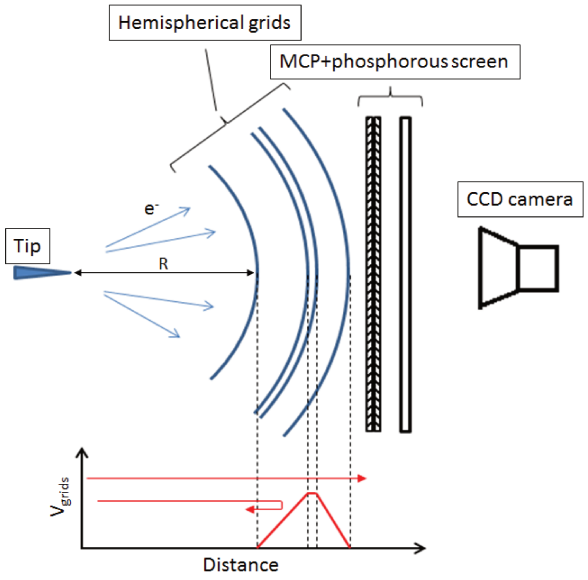

Figure 2.6: LEED schematic with the main elements of the detector. $R = 3.5\,cm$ is the working distance and radius of the hemispherical grids

In this type of microscope, one is interested in the emission properties of the samples in relation to various parameters, such as the sample temperature, the voltage applied on the base of the tip and eventually, laser illumination. In order to analyze the emission properties, the knowledge on the emission current as well as the electron kinetic energy is needed. In order to visualize and count the electron impacts, a sensitive CCD camera is placed after the phosphorous screen. The kinetic energy of the electron is measured with the use of hemispheric grids placed in front of the sample at a working distance of $R = 3.5\,cm$ which is the geometrical center of the hemispheric first grid. The grids are hemispherical in order to create a decelerating electric field parallel to the electron trajectories to minimize aberrations. The first and the last grid that the electrons encounter is at ground potential while the two internal are biased by a positive voltage which creates a decelerating potential which decreases the kinetic energy of the arriving electrons. The plane of the detector is located at a distance of about $6.5\,cm$. The detector is composed of a stack of two micro channel plates (MCPs) mounted in chevron configuration, coupled with a phosphorescent screen, each of $8\,cm$ in diameter. A voltage of $290\,V$ is applied to the entrance of the first MCP, in order to post accelerate electrons and ensure a high detection yield even for low energy electrons. A flat grid at ground potential is placed

before the detector in order to ensure that the post acceleration field is homogeneous. The bias across the MCPs is 1410 V and the bias between the MCPs output and the phosphorescent screen is 1090 V.

The kinetic energy of the emitted electrons is directly related to the voltage present on the apex of the sample ($K_E = eV_{apex}$ where K_E is the kinetic energy, V_{apex} the voltage on the apex and e the electron charge). So, when the kinetic energy of the electrons is lower than the voltage on the grids, the electrons do not have sufficient energy to pass through the grids and are rejected backward. Monitoring the arrival of electrons on the detector while increasing the voltage on the grids, one is able to measure their kinetic energy. The energy resolution of the spectrometer, in the optimal working conditions, is of 0.2% of the kinetic energy of the electrons.

2.3.2.1 Current and kinetic energy measurements

Behind the detector grids, a double micro-channel plate (for signal amplification) is placed before a phosphorous screen in order to have a 2D image of the emission pattern. The image on the phosphorous screen is acquired with the use of a CCD camera.

The kinetic energy of the electron is measured with the use of the hemispheric grids in front of the sample. These grids are biased by an increasing voltage from 0 to αK_E, where α is a proportional factor $1.01 \leq \alpha \leq 1.35$. Monitoring the arrival of electrons on the detector by increasing the voltage on the grids, we can measure their kinetic energy.

On the other hand, the current is measured by counting the single electrons arriving on the detector per unit of time (1 electron correspond to $1.602 \cdot 10^{-19} C$). This is done setting the MCPs voltage to saturation regime and with the use of the CCD camera a sequence of images is obtained where single spots correspond to single electrons (Figure 2.7). The images are on a grey scale with pixel level ranging from 0 (black) to a maximum of 255 (white, saturation). The image acquisition time can be set with a minimum of 1 ms, where its duration depends on the working conditions. For reliable measurements, we found that 10 ms gives the best signal to noise ratio with a noise current in dark of about $3 - 5\, counts/s$.

The data acquisition and treatment are done using custom software where all the necessary parameters can be adjusted. For image treatment, only grey level above 20 are considered in order to reduce the noise signal.

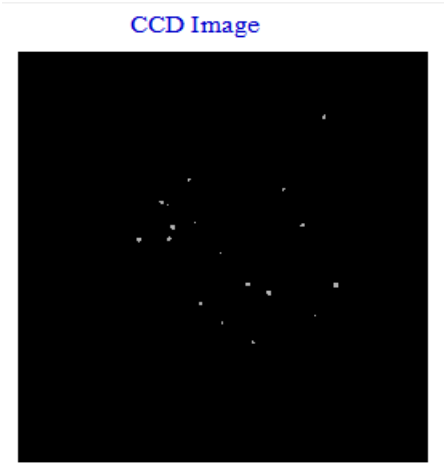

Figure 2.7: CCD camera image of 10 ms duration of emission from tungsten. Each individual spot correspond to the arrival of one electron on the detector.

In Figure 2.8, are reported two images obtained for a laser assisted emission from a diamond tip at a laser peak intensity of $I_{peak} = 27\,GW/cm^2$ and for two different applied voltages of $V_{tip} = 100\,V$ and $280\,V$, respectively. Several spots of different sizes are visible. The number of spots (N_{spots}) was counted using a routine that determined the position of local intensity maxima, each maximum corresponding to a spot. The current is calculated by : $I = \frac{eN_{spots}}{t_{image}}$, where t_{image} is the acquisition time of the CCD. One can notice that the different spots can have different intensities. This can be due to the natural distribution of spot intensities inherent to the functioning of MCP based detectors. But it is also possible that for large number of counts on a single image, some high intensity spots might actually correspond to multiple spots that are too close to each other to be discriminated. This effect would cause the measured number of counts to be underestimated at high currents. However, even if two spots are not discriminated, they should still both contribute to the total image intensity, so this should therefore be reflected on the value of the average intensity per spot. In order to quantify this effect, we calculated the distribution of the ratio $\frac{Intensity_{image}}{N_{spots}}$ for all the images recorded in the two experimental conditions of Figure 2.8a-b, which corresponds to a current of 10^3 and $10^4\,Counts/s$, respectively. An increase of about 20% was calculated for the images of Figure 2.8. This means that the number of detected spots is underestimated of about 20% at emission currents near saturation.

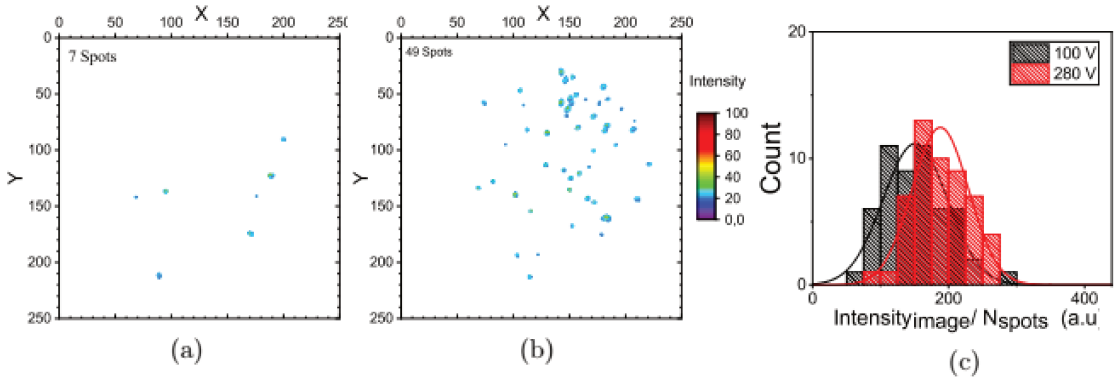

Figure 2.8: Electron hit-map as imaged by the CCD camera. Only the signal with a pixel intensity above 20 over 255 is displayed. The laser intensity is 27 GW/cm^2 and the applied voltage is (a) $V_{tip} = 100\,V$ and (b) $V_{tip} = 280\,V$. The acquisition time is 10 ms per image.(c) Distribution of the ratio $\frac{Intensity_{image}}{N_{spots}}$ for all the images recorded in the experimental conditions of (a) and (b).

With this information, the emission energy spectrum can be calculated through the derivation of the Count/s curve in function of the kinetic energy curve (Figure 2.9). As we can see from the spectrum, a FWHM width of $1.2 \pm 0.1\,eV$ is obtained. If, to this width, $0.2\,eV$ is subtracted, being $0.2\,eV$ the typical width of tungsten field emission spectrum (Figure 2.5), the difference in resolution of $1\,eV$ is comparable to the 0.2% of the applied voltage ($V_{applied} = 510\,V$). So, compared with the Argus detector, using the LEED leads to a lower resolution of the emission energy spectra.

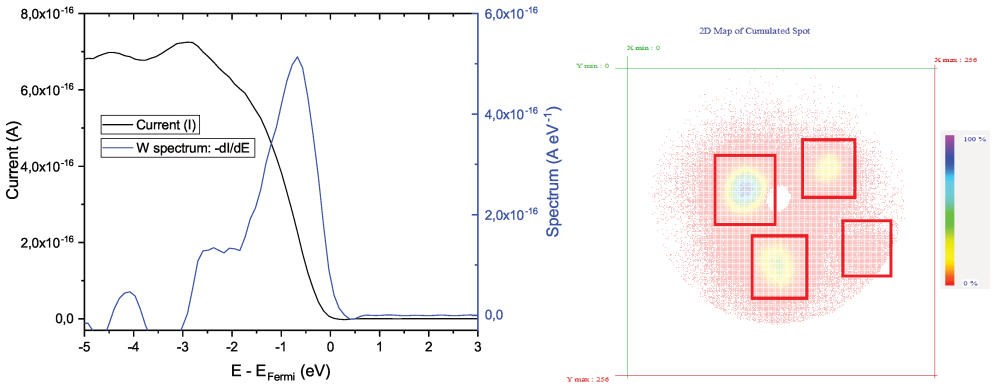

Figure 2.9: On the left: in black counts/s of emission electrons from a tungsten tip while in blue the kinetic energy spectrum calculated derivating the counts/s curve (FWHM of $1.2\,eV$, lower resolution compared to the Argus case of Figure 2.5) The data are obtained analyzing only the left pole on the pattern. On the right: emission pattern taken at $V_{applied} = 510\,V$. The four typical emission poles of tungsten are visible.

2.3.2.2 Sample alignment

In order to have the best performance, the alignment of the sample with the detector is crucial. In fact, a non optimal alignment of the specimen with the grids induces aberrations of the electron trajectories which lead to a potentially distorted emission pattern and a decrease in the energy resolution of the emission spectra.

Before the analysis on diamond samples, tungsten has been used to find the right working position of the samples in order to perform experiments. With the help of simulation of the trajectories of the electrons, the effects of misalignment can be predicted.

Our sample holder can be moved in the 3D space with the use of micro-manipulators. Figure 2.10 shows the calculated electron trajectories from a well aligned tip where no aberrations on the trajectories can be seen. These trajectories have been calculated with the use of MATLAB assuming the electrons with a initial kinetic energy of $300\,eV$ moving from the initial position and the internal grids are biased with a $299.5\,V$.

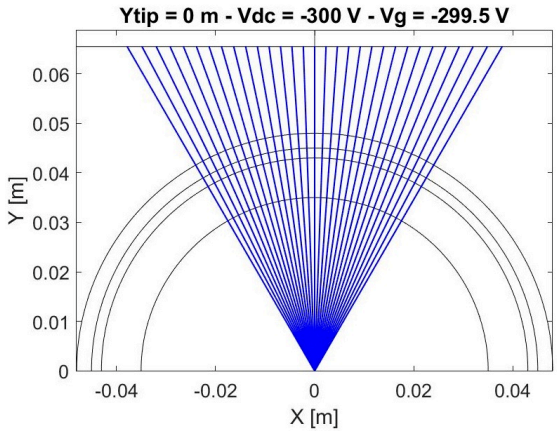

Figure 2.10: Electron trajectories from a well aligned electron source. No aberrations of the electrons trajectories.

On the other hand, Figure 2.11 shows the aberration of the electron trajectories when the tip has a position offset on the X or Z directions respect to the central position of the detector, where Y is the axis corresponding to the distance between the grids and the working position. In this configuration, the image on the detector is distorted laterally.

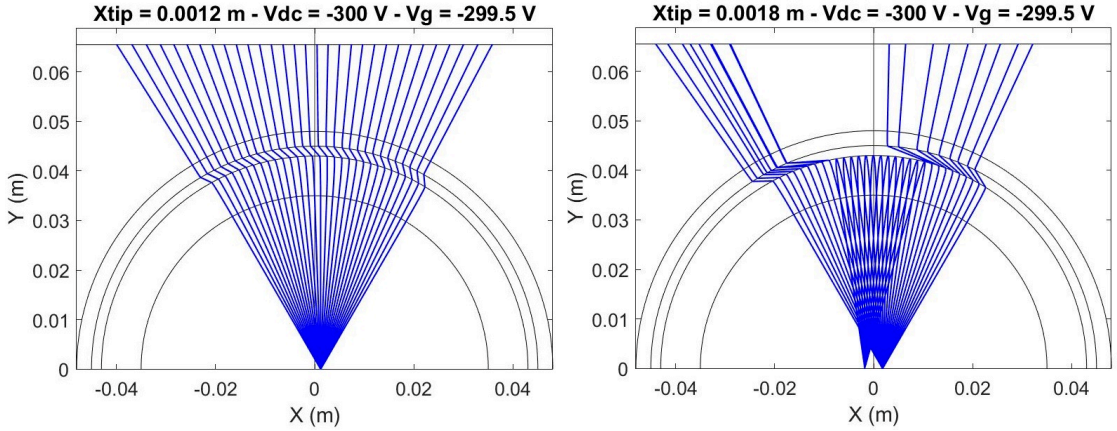

Figure 2.11: Electron trajectories with a source offset in the X (or Z) axis of 1.2 mm and 1.8 mm respectively when the grid potential is near the kinetic energy of the incoming electrons ($V_{grids} = 399.5V$). As one can see, a bad X or Z axis alignment brings aberrations on the electron trajectories. In the 1.8 mm case, the grids create sufficient potential to reject some of the electrons.

Finally, Figure 2.12 shows the electron trajectories in the case of Y misalignment where the trajectories are distorted in circular symmetry.

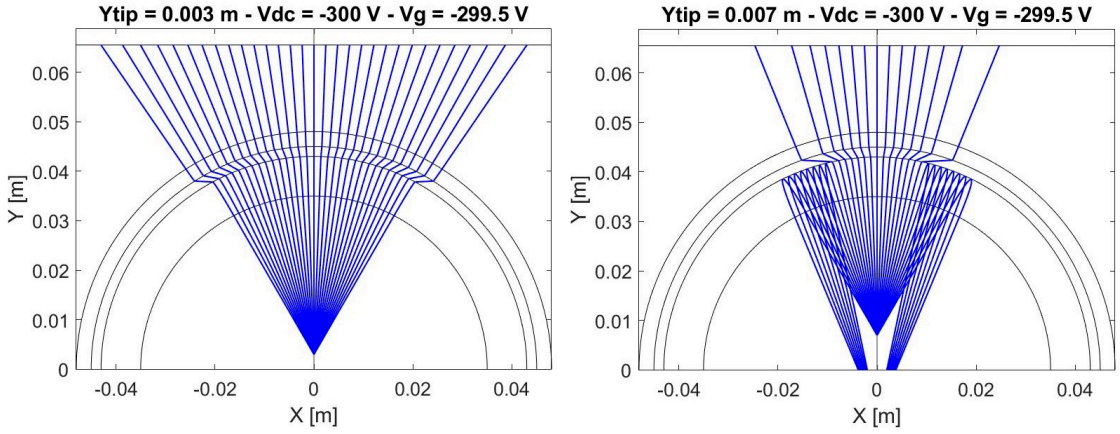

Figure 2.12: Electron trajectories with a source offset in the Y axis of 4 mm and 8 mm respectively when the grid potential is near the kinetic energy of the incoming electrons. As one can see, a bad Y axis alignment brings aberrations on the electron trajectories and induces backward rejection of some electrons.

With the knowledge of the typical aberrations in the case of a non-aligned sample, we were able to align the tip watching directly the changes in emission pattern moving the tip in the 3D space. Indeed, in the case of lateral misalignment, increasing and decreasing the potential applied on the grids the emission pattern disappears and reappears first from lateral position and then on the center completely. On the other hand, with a misalignment in the distance between sample and grids, increasing and decreasing the

potential on the grids lead to a disappearance and appearance of the emission pattern from the external or the center depending on the direction of the misalignment.

Another mean to align the tip is to find the position at which the emission pattern disappears at the highest potential on the grids. In fact, in the case of misalignment, the electrons are rejected from the grids at a lower potential respect to their kinetic energy.

So, with the use of these two methods, the right working position has been found for the various samples before each set of analysis, testing and validating the method and protocol on tungsten emitters.

2.3.3 Fiber laser

After the implementation and calibration of the LEED detector, an ultra-fast fiber laser system has been added to the workbench. The laser has been developed in collaboration with the CORIA laboratory.

The schematic diagram of the laser system used to drive this experiments is shown in Figure 2.13.

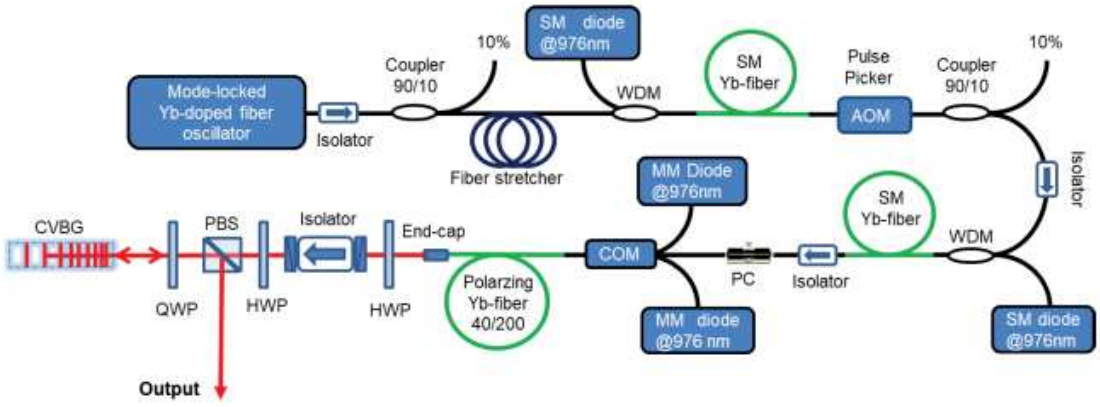

Figure 2.13: Experimental set-up of the fiber-based chirped-pulse amplifier system. WDM : Wavelength-division-multiplexer; COM : pump and signal fiber combiner; PBS : polarization beam splitter; CVBG : chirped volume Bragg grating; PC : polarization controller; QWP : quarter wave-plate; HWP : half wave-plate.

The pump laser is a 3 μJ class ultra-fast ytterbium-doped fiber-based chirped-pulse amplifier system operating at 1040 nm. The system is seeded by a home-made all-fiber oscillator operating in the dispersion-managed soliton regime and delivering a stable pulse train at 18 MHz repetition rate. A fiber Bragg-grating is used for intra-cavity dispersion management. This SESAM-based mode-locked laser provides a typical parabolic shaped spectrum with pre-chirped pulses of 13 ps duration and 15 nm spectral width (see Figure 2.14). The output is measured using a second harmonic generation-based autocorrelator (inset of Figure 2.14). The autocorrelation is well fitted assuming a Gaussian pulse shape

with 9.2 ps width (FWHM). Figure 2.14b shows the radio-frequency (rf) spectrum of the signal in 400 kHz span. The rf-spectrum of inter-mode beat notes presents an excellent signal-to-noise ratio of $> 75\,dB$. It exhibits only one noise substructure at low frequencies ($< 5\ kHz$). The amplitude fluctuations associated to this substructure are lower than 0.4% RMS. The seed pulses were further stretched to approximately 250 ps by means of a long passive fiber. To access the high energy regime, a fiberized acousto-optical modulator (AOM) was placed prior to the main power amplifier in order to lower the fundamental repetition rate down to 900 kHz.

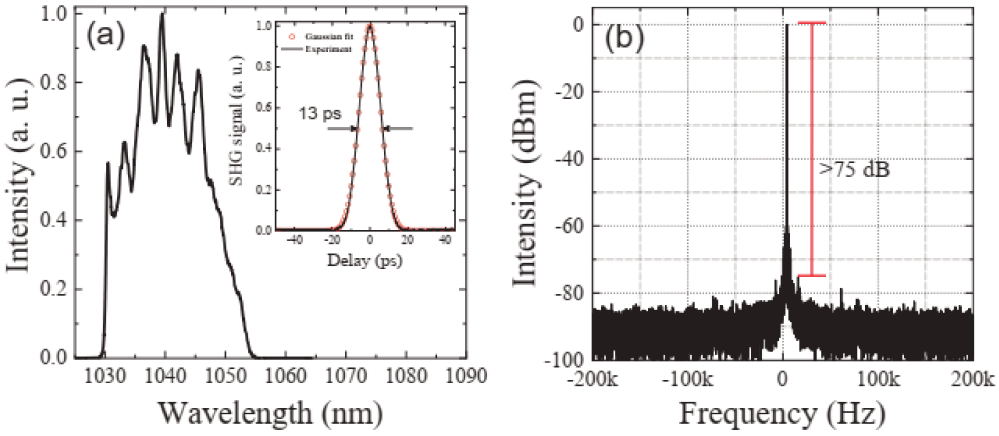

Figure 2.14: Mode-locked Yb-fiber seed oscillator outputs : (a) Optical spectrum and autocorrelation (Inset) and (b) radio-frequency spectrum at 400 kHz span and 20 Hz resolution bandwidth

Two core-pumped Yb-doped fiber pre-amplifiers were used to compensate the losses in the stretcher and AOM. The power amplifier is based on a cladding-pumped heavily ytterbium-doped polarizing large mode area microstructured fiber with 40 μm core diameter and 200 μm pump cladding. The pump and signal are coupled into the gain fiber through a fiber combiner thus offering a highly integrated laser configuration. A polarization controller is used to match the beam polarization with the LMA (large-mode-area) gain fiber polarization axis thus ensuring a linearly-polarized amplified pulses. The amplified pulses are then dechirped in a chirped volume Bragg grating compressor to less than 600 fs duration. We note that the residual pump is removed using a dichroic mirror which is not shown in Figure 2.13. The Fiber Chirped Pulse Amplification (FCPA) system performances remains very stable for repetition rates lying between 0.9 to 18 MHz with a maximum output power of 2.5 W which corresponds to more than 2.7 μJ. The laser outputs for an average power of 2 W and different repetition rates are depicted on Figure 2.15. We note that the amplified pulses suffer from gain narrowing within the amplification stages as well as from some spectral clipping at short wavelengths. The output spectral width is lower than 8 nm. So, the output pulse duration varied between

500 and 700 fs when decreasing the repetition rate from 18 to 0.9 MHz (see Figure 2.15). The pulse-to-pulse amplitude fluctuations measured at the amplifier output remains lower than 1% RMS. To reach even lower repetition rates, a free-space AOM is included at the laser output, enabling the repetition rate to be divided by a factor up to 1000 with an achievable minimum repetition rate of 1 kHz. The contrast measured at the laser output is higher than 10.000 thus limiting the impact of inter-pulse residual noise.

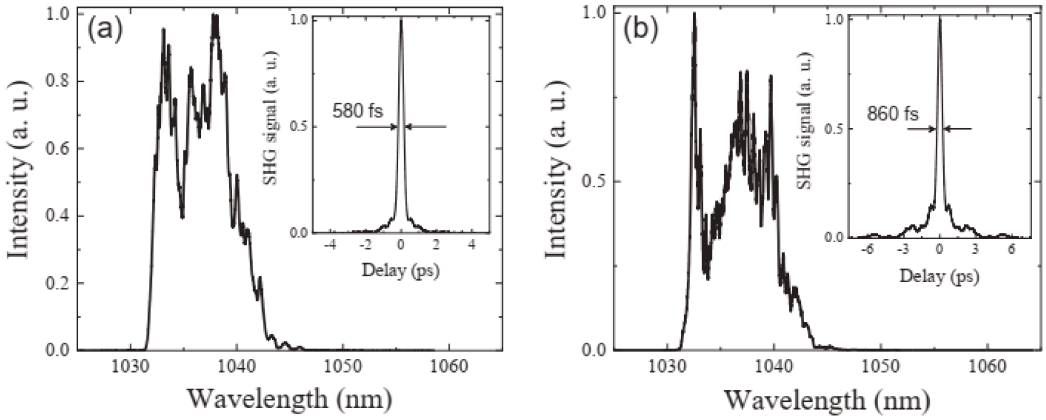

Figure 2.15: Amplifier outputs at an average power of 2 W for 18 MHz (a) and 900 kHz (b) repetition rates. Insets correspond to the measured autocorrelation traces.

At the output of the laser, prior its entrance in the vacuum chamber, a half-wave plate as been placed to control the linear polarization angle between the laser and the tip axis. Also a variable density filter has been position on the laser path in order to modulate the laser mean power.

2.3.3.1 Laser alignment

Once the sample is aligned properly with the detector following the procedure described above, the laser system has been initially aligned on the apex of the tip with the use of lenses placed outside the vacuum chamber. In particular a set of two lenses enlarge the beam waist to a measured value of 10 mm, while at the entrance of the chamber a lens with a focal length of $f = 300\,mm$ gives a laser beam waist at the focal point of 45 μm (diameter at $1/e^2$). This focal beam waist is large enough to illuminate a big part of the sample. The alignment is also checked using the diffraction pattern seen by a long-distance microscope objective on a CCD camera mounted on a window of the vacuum chamber. Confirmation of the exact alignment is corroborated by rotating the polarization of the laser beam. As stated by Barwick et al. [35], when correctly aligned, electron emission is negligible for polarization perpendicular to the tip axis, as will be presented in Chapter 4.

In a second time, a hemispherical golden mirror with focal length of 5 mm has been inserted inside the chamber in order to reduce the laser beam waist at the focal point to illuminate only the apex of the samples. This mirror can rotate with the use of micro-manipulators in order to optimize the laser alignment. With the use of this mirror, a theoretical focal beam waist of 5 μm has been calculated for a laser wavelength of $\lambda_{IR} = 1040\, nm$.

2.3.4 Static emission from tungsten tips

In order to validate the field emission workbench, a preliminary study has been done on tungsten tips. Since this material has been largely studied in literature as a field emitter, both in static and under laser illumination regimes, it provides a good reference in order to validate the experimental set-up.

Since tungsten is a metal, the field emission characteristic should follow the Fowler-Nordheim (FN) law:

$$J(V) = \beta^2 V^2 exp\left(-\frac{\alpha}{\beta V}\right) \tag{2.2}$$

where α is a constant of Equation 1.3 and β the electric field enhancement factor ($E = \beta V$).

2.3.4.1 Argus spectrometer

As discussed above, with the use of the Argus spectrometer, energy emission spectra are acquired. From the emission spectra taken at different applied voltage, the $I - V$ characteristic curve of the sample can be obtained. Knowing the emission current at different bias voltages, applying the natural logarithm Equation 2.2 can be reformulated as

$$ln\left(\frac{J(V)}{V^2}\right) = -\frac{\alpha}{\beta} \cdot \frac{1}{V} + constant \tag{2.3}$$

where the ratio $\frac{\alpha}{\beta}$ can be obtained from the slope of the curve plotted in "Fowler-Nordheim coordinates": $ln\,(J/V^2)$ as a function of $1/V$. Figure 2.16 shows the FN plot from tungsten using the Argus spectrometer. The FN curve shows a linear behavior typical of metal samples.

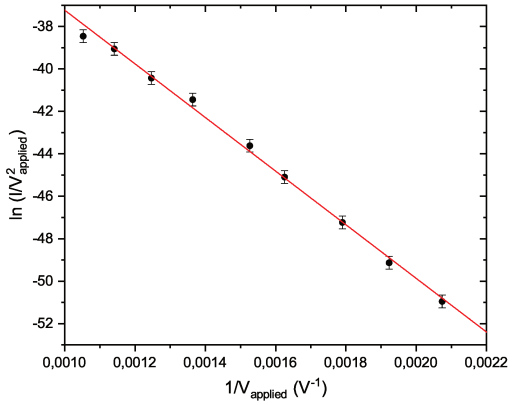

Figure 2.16: $I - V$ characteristic represented in FN coordinates of the emission from a tungsten tip, the applied voltage is increased from $480\,V$ to $950\,V$.

On the other hand, on the left of Figure 2.17 different normalized spectra represented respect to the Fermi level are shown. Increasing the applied voltage, the energy spectrum width increases. This is a consequence of the increase of tunnel probability at higher applied voltages which reduce the barrier potential $U(x)$ of the metal/vacuum junction (see schema of Figure 2.17).

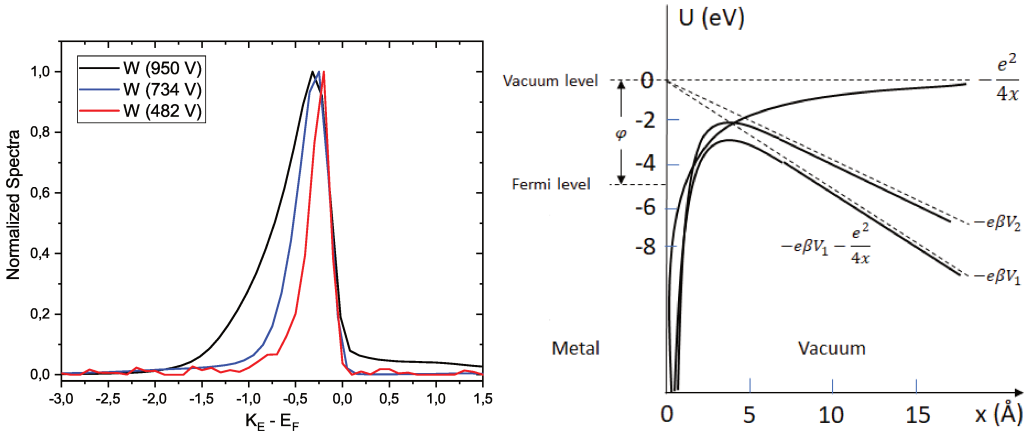

Figure 2.17: On the left, normalized energy emission spectra from tungsten taken at different applied voltages. On the right, the potential energy of electron $U(x)$ as a function of the distance x from the metal surface. $-e\beta Vx$ is the external applied potential, φ the work function and V the applied voltage with $V_1 > V_2$.

2.3.4.2 LEED detector

After the analysis done with the Argus spectrometer, the LEED detector has been mounted in order to record the emission pattern in preview of the implementation of a laser system which can lead to modification of the emission pattern.

Also in this case, the tungsten tips have been tested in the FN coordinates in order to check the reproducibility of the results with the new detection system. Figure 2.18

shows the FN curve and emission pattern from tungsten in static regime with the use of the LEED detector. Also in this case, the FN curve is linear as expected in the case of metallic emitters, showing the good operation of the new detecting system. Furthermore, the emission pattern presents the four emission poles typical of tungsten samples.

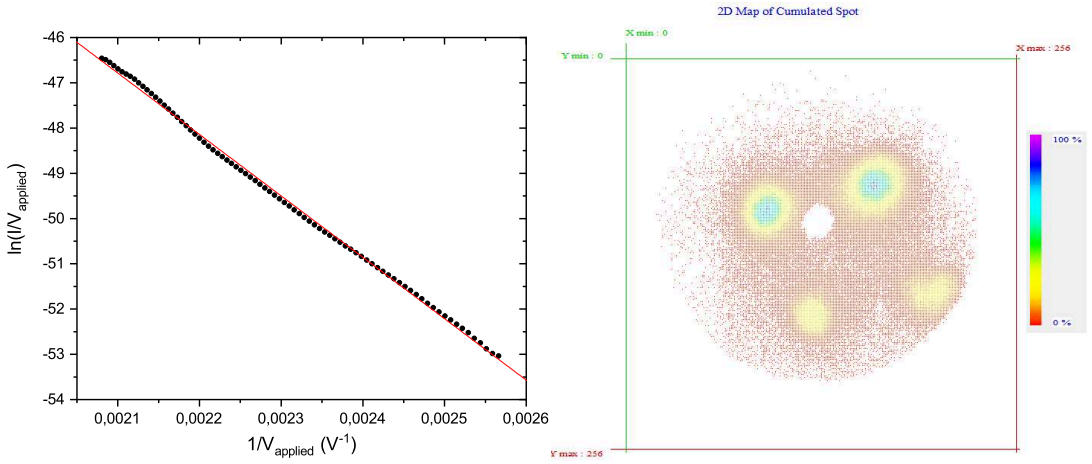

Figure 2.18: On the left, $I-V$ characteristic represented in FN coordinates of the emission from a tungsten tip, the applied voltage is increased from $390\,V$ to $480\,V$. On the right, emission pattern obtained accumulating the electron arrival during the FN measurement shown on the left.

2.3.5 Laser assisted field emission from Tungsten

With the implementation of a laser system on the electron emission workbench, the emission properties from tungsten have been monitored as a function of the laser peak intensity. In particular the modification of the emission can be characterized in the $I-V$ curves plotted in the FN coordinates as well as by monitoring the changes on the electron energy spectra and emission pattern.

2.3.5.1 Measurement with the external lens

The first series of measurements done have been carried out with the use of an external lens, as described above, which gives a laser focus on the apex of about $45\,\mu m$ in diameter (measured at $1/e^2$). The first measure consist in the monitoring of the emission changing the laser polarization angle respect to the sample axis. This type of graph gives an indication of the well alignment on the apex of the tip since, since the laser assisted field emission depends on the laser polarization angle:

$$J \propto (E_{laser} cos(\theta))^{2n} \tag{2.4}$$

where θ is the polarization angle respect to the tip axis and n is the number of mean absorbed photons, where emission at perpendicular polarization gives an indication of thermal effects due to the laser [36].

In Figure 2.19 the emission current dependence as a function of the laser polarization angle is reported. These measurements have been taken at low applied voltage ($V_{applied} = 100\,V$) where only the laser effect is visible. At this low voltage, with a relatively high laser peak intensity ($I_{laser} = 40\,GW/cm^2$), the emission is on the right side of the detector (emission pattern of Figure 2.19).

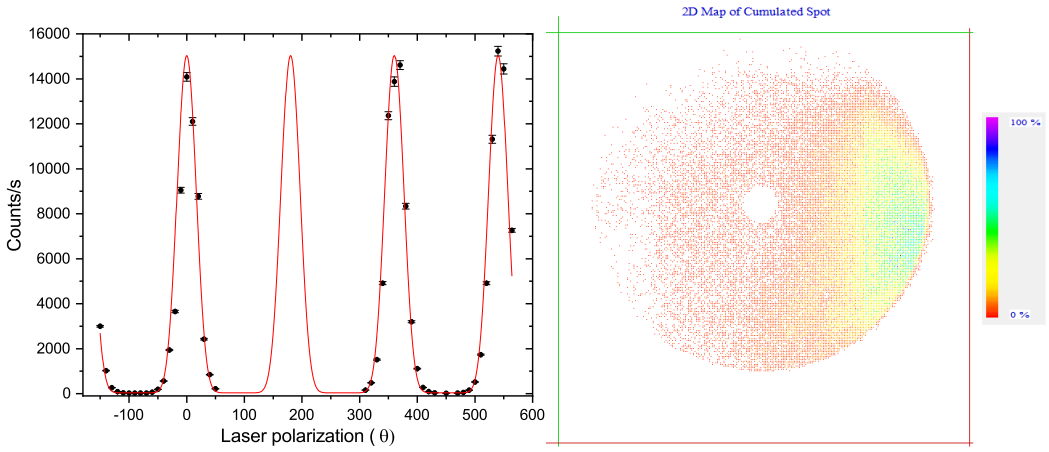

Figure 2.19: Laser assisted field emission from tungsten as a function of the laser polarization and relative emission pattern, taken at $V_{applied} = 100\,V$ and laser peak intensity $I_{laser} = 40\,GW/cm^2$. The fit is done with a $\propto cos^{2n}(\theta)$ curve where $n = 6$ indicating a 6 multi-photon absorption process.

In these conditions, laser assisted FN curves have been taken for different intensities of the laser as shown in Figure 2.20. As one can see from the graph, at high applied voltages ($V_{applied} > 400\,V$) the FN curve shows a linear behavior while at low applied voltage ($V_{applied} < 250\,V$) and high laser intensity the FN curve becomes constant. This suggests the presence of two different emission regimes which was already observed by Yanagisawa et al. [37]. At high voltages, where the FN is linear, the regime is of the photo-assisted emission type while at low voltages the emission is of the multi-photon type. These two emission regimes are schematized in Figure 2.21. From the emission pattern, one can see that at low laser intensity, the emission is from the 4 emission pole typical of the static field emission of tungsten while at high laser intensity the multi-photon emission on the right side of the detector starts to appear, as in the case of the polarization curve taken at low voltage of Figure 2.19.

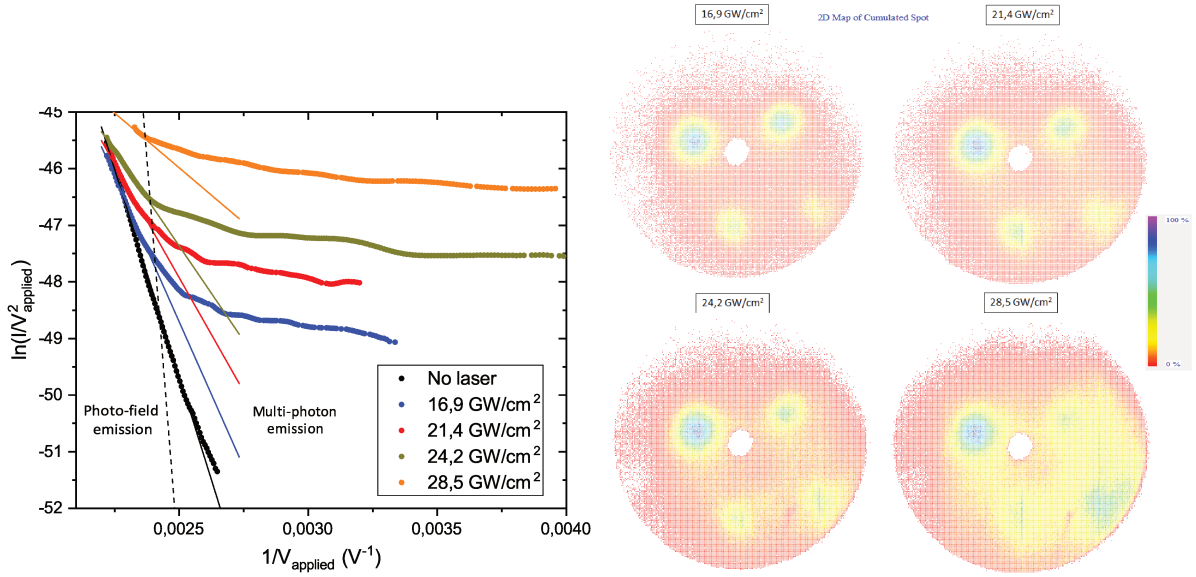

Figure 2.20: Laser assisted FN curves as a function of the laser peak intensity and relative emission patterns.

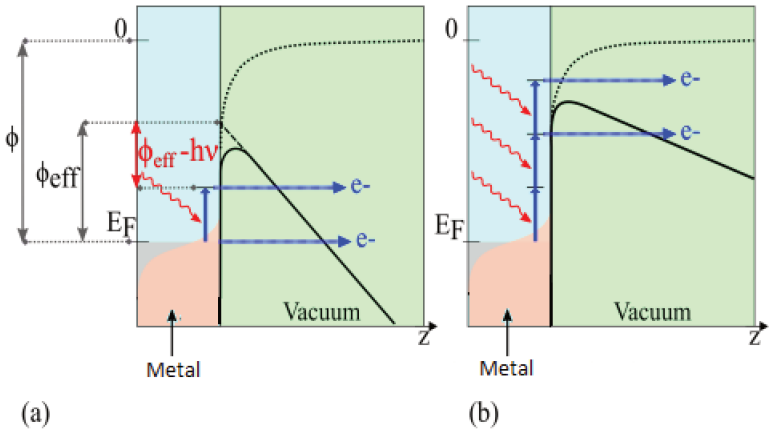

Figure 2.21: Laser assisted electron emission processes: (a) photo-assisted field emission; (b) multi-photon field emission.

On the other hand, electron energy spectra were taken under laser illumination at high applied voltage and low applied voltage in order to check the photo-assisted field emission and multi-photon field emission respectively. Figure 2.22 shows the emission spectrum under 33.3 GW/cm^2 of peak intensity at $V_{applied} = 300\ V$ with the respective emission pattern. As one can see from the emission pattern, even though the applied voltage is under the emission threshold of 350 V with no laser illumination, the four emission poles typical of tungsten static emission are visible as well with hmulti-photon emission (right part of the detector). This means that the laser has the effect of decreasing the effective work function of the emitter (as shown in Figure 2.21a) , which results in an

emission from the poles. Furthermore, a part of multi-photon emission is present as well. This is reflected also on the emission spectrum where the electron energy goes up to 6 multi-photon absorption.

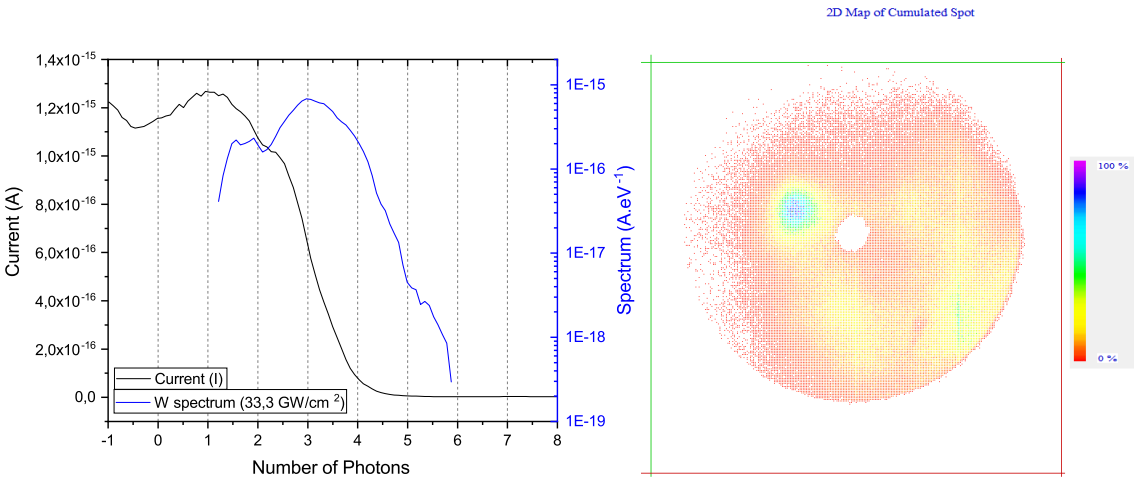

Figure 2.22: Field emission spectrum under laser illumination with $I_{laser} = 33.3\,GW/cm^2$ and at $V_{applied} = 300\,V$ and relative emission pattern. The abscissa is calculated using $(K_E - E_F)/\hbar\nu_{laser}$ in eV with $\hbar\nu_{laser} = 1.2\,eV$.

The same study has been done also at low applied voltage $V_{applied} = 30\,V$ in order to isolate the multi-photon emission (Figure 2.23). In this case, from the emission pattern of Figure 2.23 only emission on the right side of detector is visible. Moreover, the energy spectrum indicates a 4 to 6 multi-photon absorption process.

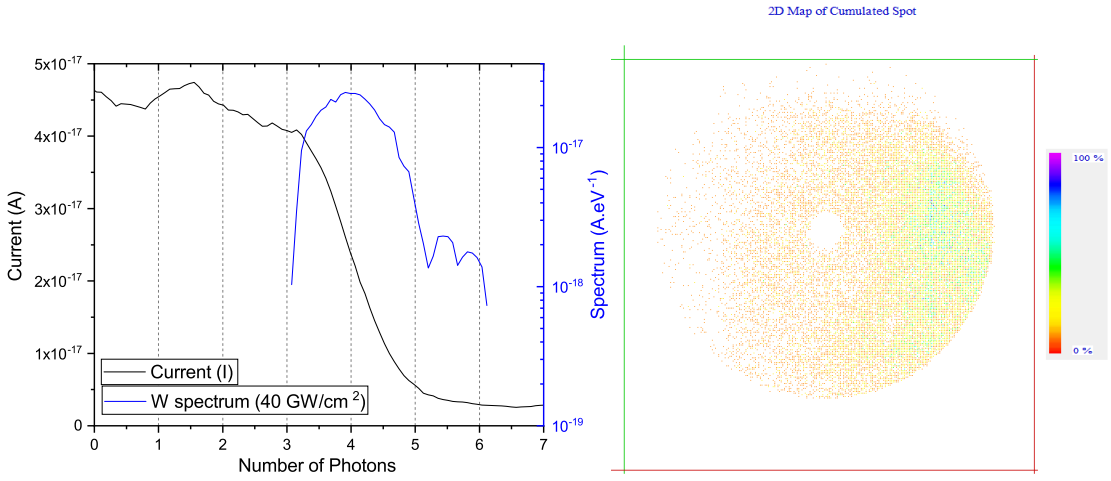

Figure 2.23: Field emission spectrum under laser illumination with $I_{laser} = 40\,GW/cm^2$ and at $V_{applied} = 30\,V$ and relative emission pattern. The abscissa is calculated using $(K_E - E_F)/\hbar\nu_{laser}$ in eV with $\hbar\nu_{laser} = 1.2\,eV$.

2.3.5.2 Measurement with the internal mirror

After the study with the use of an external lens, a hemispheric mirror has been implemented inside the vacuum chamber in order to achieve a smaller beam size in the focus point. With the use of this mirror, a beam waist of 5 μm is achievable. The use of a more focused laser gives some advantages respect to a broader beam waist, such as higher laser intensity, better focalization on the tip apex which in the case of non conducting materials, the possibility of illuminating only the tip apex, do not influence the conductive behavior of the bulk part of the samples.

Before laser-assisted field emission, this tip has been characterized in static regime (FN and emission pattern of Figure 2.24).

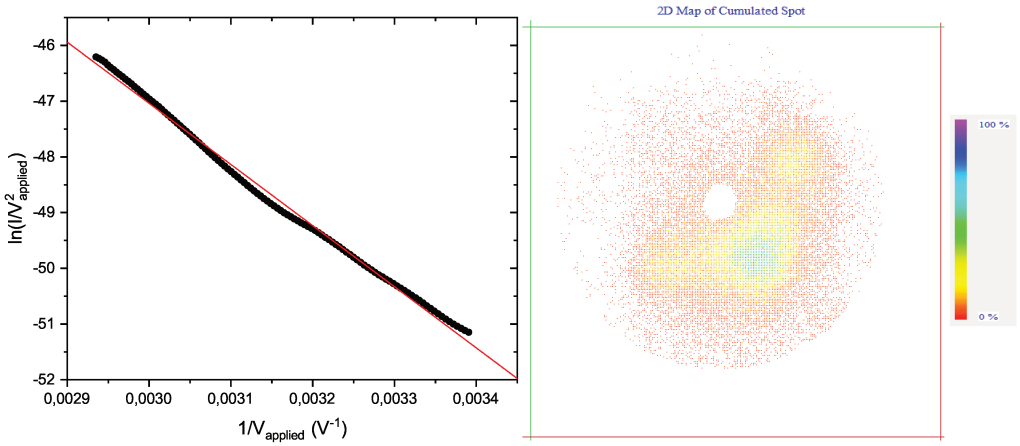

Figure 2.24: On the left, $I-V$ characteristic represented in FN coordinates of the emission from the tungsten tip used in the laser measurements with the internal mirror, the applied voltage is increased from $290\,V$ to $340\,V$. On the right, emission pattern obtained accumulating the electron arrival during the FN measurement shown on the left.

Figure 2.25 shows the emission curve as a function of the laser polarization angle. Also in the mirror case, the polarization behave $\propto cos^{2n}(\theta)$ indicating good alignment and no thermal effects [35]. As we can see, the laser has the effect of enhancing the emission from the tungsten poles with the appearance of a new one on the upper left which could not be activated in static regime.

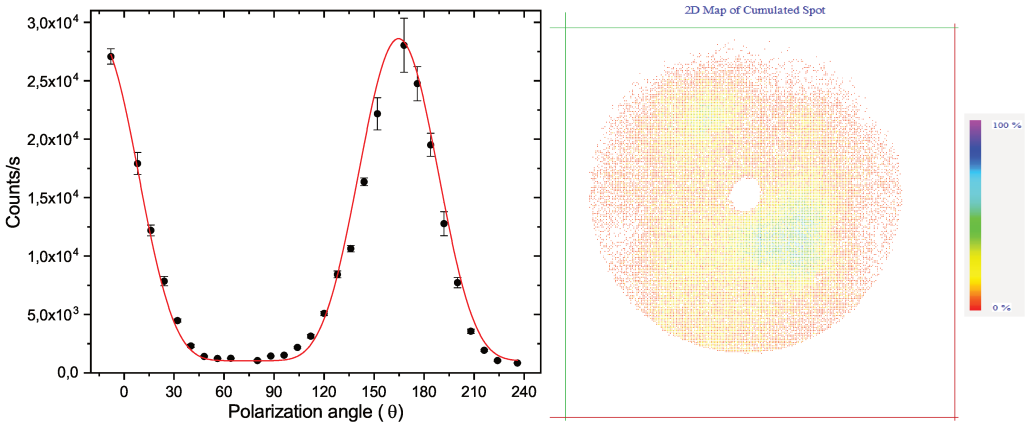

Figure 2.25: Laser assisted field emission from tungsten as a function of the laser polarization and relative emission pattern, taken at $V_{applied} = 300\,V$ and laser peak intensity $I_{laser} = 50\,GW/cm^2$. The fit is done with a $\propto cos^{2n}(\theta)$ curve where $n = 3$ indicating a three photon absorption process.

Also in this case, energy emission spectra have been acquired as shown in Figure 2.26. From the emission pattern we can see that the fluence increase through a tight focalization of the laser beam results in an increase of the emission from the static poles.

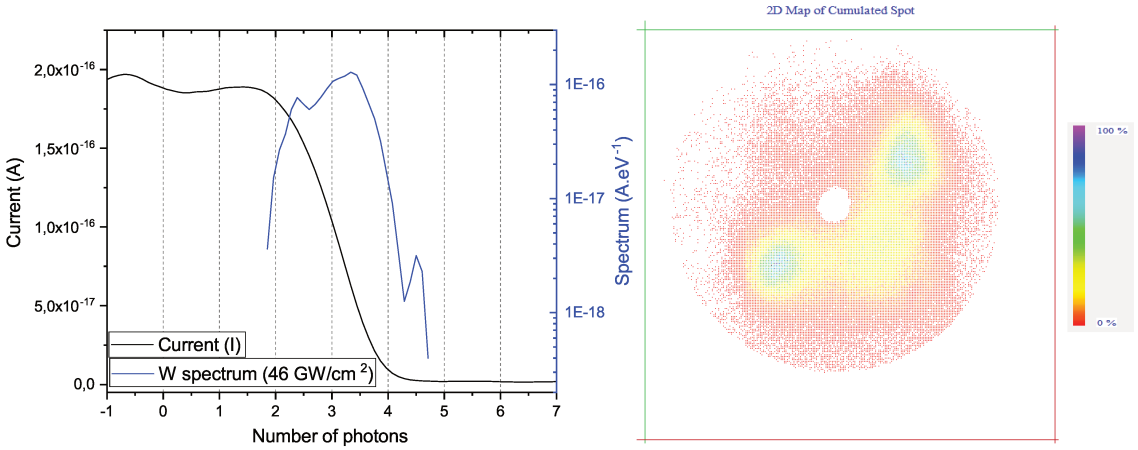

Figure 2.26: Field emission spectrum under laser illumination with $I_{laser} = 46\,GW/cm^2$ and at $V_{applied} = 350\,V$ and relative emission pattern. The abscissa is calculated using $(K_E - E_F)/\hbar\nu_{laser}$ in eV with $\hbar\nu_{laser} = 1.2\,eV$.

This is confirmed from the emission pattern recorded under laser illumination at low voltage where the static emission is not present, as shown in Figure 2.27. In fact, even though the applied voltage is much lower than the static threshold ($390\,V$), the static emission poles appear in the emission pattern.

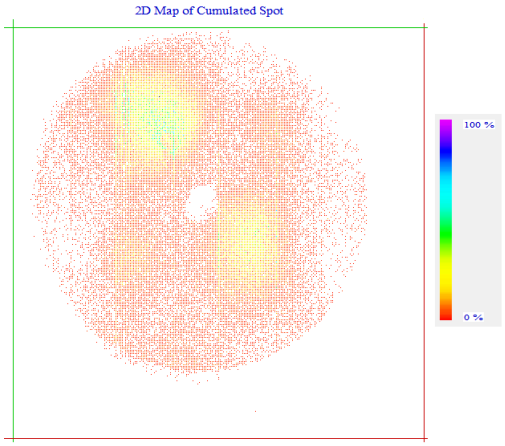

Figure 2.27: Emission pattern from tungsten with a laser peak intensity of 90 GW/cm^2 and applied voltage of 80 V.

2.4 Conclusions

In this chapter, the various experimental set-ups used in this work have been described. In particular, the first setup is a FIM (FlexTAP) where the electrical conduction mechanism of CVD diamond is studied. This instrument was already set for the study of non-conductive materials through the use of electrostatic lenses in order to measure the ion energy deficit which is directly related to the potential present on the apex of the sample. A pico-amperometer has been connected to the phosphorous screen of the detector to measure the flowing current from the sample.

The second setup is a FEM used in the study of the field emission properties of CVD diamond. This instrument was not operative at the start of this thesis. In fact, the new Argus detector had just being mounted at the beginning of this work. This high resolution detector has been set and calibrated with the use of tungsten emitters. The main objective with this type of detector was to characterize the static field emission from CVD diamond samples.

In a second time, a LEED detector has substituted the Argus detector in order to obtain both the 2D information of the emission pattern as well as the emission energy spectrum in the preview of the implementation of a fiber laser for the study of laser assisted field emission from diamond. Also in this case, the experimental protocol and method has been validated with the use of tungsten nano-tips.

Chapter 3

Study of the electric conduction of CVD diamond

In order to understand better the limitation of the laser assisted-Atom Probe Tomography (la-APT) on non-metal samples, the need of a better understanding of the conduction properties and matter-laser interaction is of vital importance. In fact, this technique needs high electric field (around 10 V/nm) and laser pulses in order to evaporate atoms from the surface of the sample. La-APT has been developed in 2004 with the use of ultra-short laser pulses (below the picosecond pulse) with the aim of overcoming the limitation of the classical APT restricted to good conductor materials.

3.1 Laser assisted-Atom Probe Tomography: issues on non-conductive materials

The atom probe tomography, designed by Muller et all. [33], is a very powerful technique useful in the identification of atomic composition as well as atomic position of micro- and nano-objects. This technique has been developed on the base of the Field Ion Microscope invented by the same Muller [38].In order to work, ATP needs high electric field (around 10 V/nm) in order to be able to evaporate atoms from the surface of the sample to analyze. To achieve this kind of electric field, the sample to analyze are usually prepared in a tip geometry with a nano-metric radius of curvature at the apex in order to have a large field enhancement thanks to the lighting rod effect. The first models of APT microscopes used short electric voltage impulse to raise the apex electric field over the threshold for ions evaporation and for the triggering of the time of flight measurement. Time of flight mass spectrometry is used to determine the mass/charge ratio (chemical nature) of evaporated ions. On the other hand, through the measurement of the position

of impact of the vaporized atoms on the detector, their starting position inside the sample can be obtained. With this information (chemical nature and position inside the sample) a 3D reconstruction of the object can be achieved.

On the other hand, with the use of ultra-fast laser pulses, the application restricted only on good conductors materials has been extended to semi-conductors and insulators as well. Figure 3.1 shows the schema of la-APT, FIM and FEM functioning.

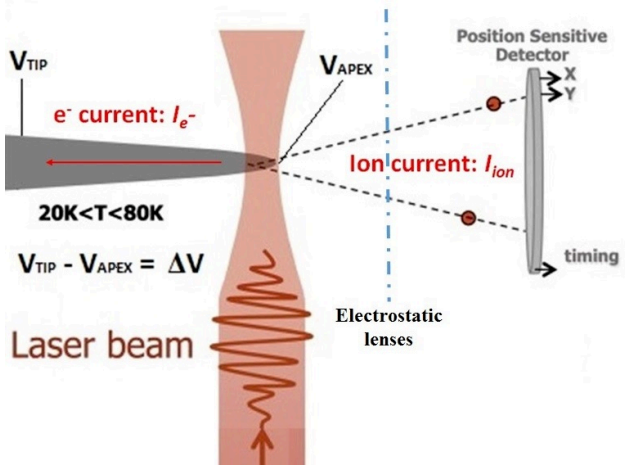

Figure 3.1: Schematic diagram of a la-APT, FIM and FEM chamber. In the case of standard APT, electron pulses substitute the laser ones. In the case of field emission, the voltages are negative for electron emission.

In the case of electrical conductors, the evaporation of atoms triggered by laser pulses, has been explained by thermal excitation of field evaporation [39]. However, in the case of semi-conductors and insulators, the La-APT results to strongly depend on the optical, thermal and electrical conduction properties of the nano-metric scale sample [40]. Furthermore, the presence of a high electric field applied on the sample could lead to modifications of these properties, such as the conduction band structure which is directly related to the optical and electric properties of wide band gap materials. With the intent of an optimization of the La-APT results on semi-conductors and insulators, the choice of the best analysis conditions in term of laser wavelength, power, electric field strength and evaporation rate, is essential [41].

For this reason, it is of great importance a better knowledge of the effects of high fields on nano-metric scale objects, in term of changes in electronic states, carrier transport and optical excitation. Several phenomena on the effect of high field on solids have been addressed theoretically and experimentally, but the understanding of the dramatic changes in the response and properties of dielectrics submitted to high electric fields is lacking. The use of La-APT could lead to new observation of behaviors induced by the high electric field in nano-metric scale dielectrics [42].

3.2 Previous works on the energy deficit

Previous work have already addressed the problematic that the poor conductivity of semiconductors and dielectric could reduce the performances of the ATP. In detail, poor conductivity can be at the origin of the energy deficit and the energy dispersion of the emitted ions.

3.2.1 The dielectric model

Non-conductive samples in APT can be modeled as dielectric materials mounted on a metallic support. This hypothesis has been addressed in literature by different authors which through simulations [43, 44], obtained a lower electric field on the apex of the sample compared with the metallic case caused by a field penetration inside the dielectric (figure 3.2). This penetration is more elevated for materials with higher relative dielectric constant ε_r. However, experimental observation pointed out the fact that such strong penetration of the field does not occur, making this type of materials analyzable in la-APT. In fact, other studies have been made in order to explain the discrepancy between theoretical prediction and experimental observation [42]. In this picture, a new effect has been added to explain the experimental observations, such as a self-induced screening on the surface of the electric field by the electric field itself. In details, the strong electric field generated by the voltage applied on the samples is strong enough to give the few carriers inside the material enough kinetic energy to ionize new carriers by impact ionization process. These new carriers gain also kinetic energy to contribute to the impact ionization creating an avalanche effect. So, the carrier density becomes large enough to screen the electric field at the surface. This screening of the electric field can change also the optical absorption of the sample, even for sub-band gap photon energies, giving them metal-like optical absorption properties which explain the above prediction performance of la-APT analysis. With this explanation, laser pulses do not create carriers on the apex surface in order to screen the field allowing their analysis. Instead, laser pulses are seen as carrier creators inside the bulk of the material, where a low density of carriers should still remain. In this way, laser pulses should have the effect of decreasing the resistivity of the tip. Since the voltage drop due to the resistivity effects strongly depends on the current flowing inside the sample, this effect is strongly evident in FIM measurements where the current involved are more than 10^4times higher than APT. In the case of high resistivity materials, as for example MgO, where in APT have been measured a drop of some Volts by Chen et al. [40], in FIM analysis could lead to a voltage drop above the hundreds.

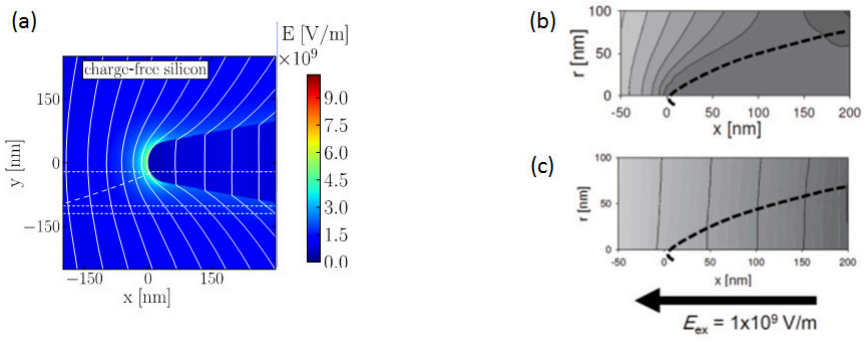

Figure 3.2: (a) simulation of the distribution of the electric field (color map) on a silicon tip under an electric potential [44]. Simulation of the electrostatic potential under an external electric field of $10^9\,V/m$ in the case of a (b) metal tip and (c) MgO without holes [45].

3.3 Field Ion Microscopy as a mean to study electrical conduction properties

In order to study the conduction properties of large band gap materials under high electric field we chose to use Field Ion Microscopy (FIM), the "father" of the APT technique. FIM operates with the use of an image gas (usually hydrogen, helium, neon and argon), which is ionized by the high electric field present on the apex surface of the sample to analyze. This ionized gas is repulsed by the positive voltage present on the apex of the sample toward the detector of the microscope creating a 2-dimensional image of the surface of the specimen. Being the electric field is not uniform on the apex surface, but stronger on the atoms sites, the image on the detector reflects the atom distribution thus allowing an atom by atom image of the surface (Figure 3.3).

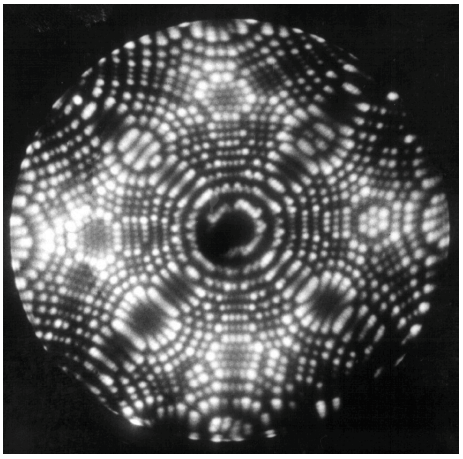

Figure 3.3: Field ion microscope image of Platinum. Each tiny bright spot, related where the electric field is more enhanced, corresponds to a platinum atom. This image was taken from the sample cooled to liquid He temperature with imaging gas of He-Ne mixture.(image taken from `https://www.flickr.com/photos/74624435@N00/315745462/`)

At the same time, a laser beam can be also focused on the sample, where it is used for the evaporation of surface atoms in the case of APT measurements. Furthermore, the working conditions of FIM are the same as in the case of APT, in terms of low temperatures ($20 \div 100\ K$) and high electric field and laser illumination.

In our case, the main reason of using FIM, is that the current flowing through the sample, which is the opposite of the current of the ions hitting the 2D detector, is orders of magnitude higher than the current present in APT analysis. This allows the probing of a wider range of current, in order to study the resistivity effects. Also, the FIM mode allows the study of the conduction properties in dark, since it is not necessary the use of the laser as in the case of the atom probe mode. Lastly, the FIM can be used also as a non-destructive technique, since APT requires the evaporation of atoms for the analysis which results in a destruction of the sample.

The FIM measurements has been done with the use of the FlexTAP instrument, which has been described in Chapter 2.

With the use of the FlexTAP, which can be used to measure the kinetic energy of the ionized gas, it is possible to measure the voltage drop (ΔV) present on non-conductive tips, since the bad electrical conductance of dielectrics could lead to a difference between the applied voltage on the sample base and the actual potential present on its apex. The kinetic energy of the ion gas which fly to the detector, $K = -neV_{apex}$ where n is the ionization number and e is the elemental charge, can be measured with the use of the retarding lens present in FlexTAP. In fact, the voltage applied to the retarding lens necessary to stop the arrival of ions is the same as the voltage present on the apex where the gas ionization takes place. This voltage present at the apex can be measured with a

resolution of 0.1 % of the voltage applied on the retarding lens. On the other hand, in order to measure the current, a pico-amperometer has been connected to the phosphorous screen of the FIM detector in FlexTAP. Moreover, the laser present in the FlexTAP setup can be used to illuminate the tip during measures with different laser wavelength and power (ultra violet UV, green and infra-red IR) to study the effect of it on the conduction properties.

3.4 FIM measurements on CVD diamond

As already discussed in Chapter 1, the dielectric material chosen for this study is CVD diamond. In this instrument, different analysis has been carried out on different diamond tips. At the beginning of this thesis, the means for a measure of the current flowing during analysis was not present, so the measurements were focused on the influence of the laser illumination on the voltage drop along the tip.

In a second time, with the implementation of a pico-amperometer on the detector of the FIM mode of FlexTAP, the $I - \Delta V$ characteristic of CVD diamond have been studied as a function of different parameters, such as the chamber gas pressure, temperature, applied voltage and laser illumination.

3.4.1 Change in the voltage drop in function of the laser illumination

As discussed above, at the beginning of this thesis, since a measure of the ion current was not possible, FlexTAP has been used to monitor the evolution of the voltage drop on the samples in function of the laser power, as well as a study in function of the laser wavelength.

The sample used in this preliminary study is shown in Figure 3.4.

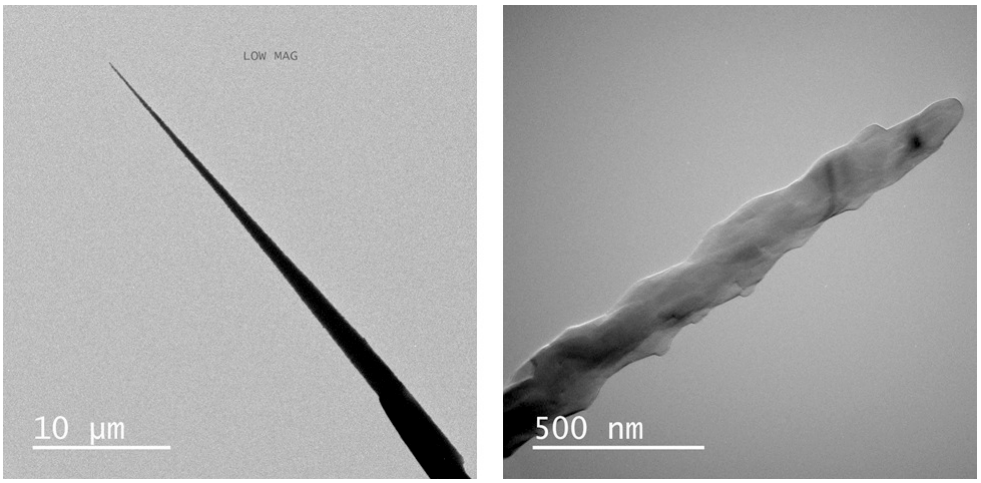

Figure 3.4: Diamond B6, length $\sim 40\,\mu m$, tip apex $\sim 35\,nm$.

The potential present on the apex of the sample V_{apex}, where the ionization of the imaging gas takes place, can be measured with the use of the retarding lens (more details in Chapter 2).

The measures were done at a constant pressure of He gas in the chamber, $p_{He} = 1.8 \cdot 10^{-5}\,mbar$, at temperature $T = 80\,K$ and a constant applied voltage on the base of the specimen $V_{applied} = 7.43\,kV$. As shown in Figure 3.5, when the diamond is illuminated by the laser, the voltage drop $\Delta V = V_{applied} - V_{apex}$ along the sample decreases with the increase of the laser intensity. Assuming that the laser illumination creates a mean density of carriers Δn_{laser}, knowing the geometrical shape of the diamond and some of its properties such as its carrier mobility μ_c, an estimation of its resistance R and its dependence with the laser intensity can be made with the use of the following equation:

$$R = \frac{L_{tip}}{e\mu_c n_c S_{tip}} \tag{3.1}$$

where L_{tip} is the length of the tip ($\sim 40\,\mu m$),$S_{tip} = \pi r_{apex} r_{base}$ the mean cross section for a cone shape geometry and n_c the carrier density. This relation is valid in the assumption that the resistive effect is of the Ohmic type. In this model, since $n_c = n_0 + \Delta n_{laser}$, it is evident that the increase in carrier density due to the laser illumination decreases the resistance of the sample, which is translated in a decrease of voltage drop, as shown in the experiments of Figure 3.5. Also, knowing the flowing current, an estimation of the number of laser-generated carriers could be possible.

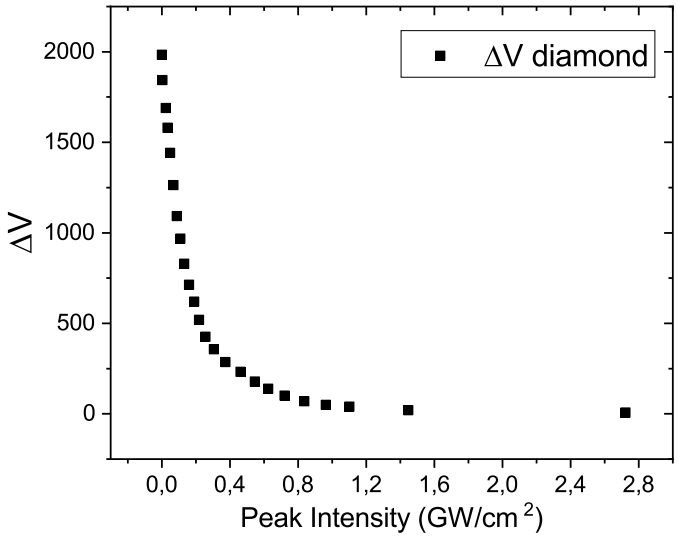

Figure 3.5: Voltage drop of a diamond sample in function of the laser peak intensity at constant applied voltage $V_{applied} = 7.43\,kV$, pressure $p_{He} = 1.8 \cdot 10^{-5}\,mbar$. The laser has a wavelength $\lambda = 343\,nm$, at laser frequency $100\,kHz$ with pulse duration of $500\,fs$.

In order to estimate the flowing current, we based ourselves on precedent studies on p-doped Si made by Arnoldi et al. [46], where a similar study has been carried out. In his case, knowing the exact properties of their sample, they found a flowing current of $I \sim 300\,pA$. Comparing to Arnoldi et al. experiments, due to a similar geometry of the sample and a similar emission points in the FIM images (Figure 3.6), it is justified to affirm that the current in our case is of the same order of magnitude. Using this order of magnitude of current, using the voltage drop in dark we obtain a diamond resistivity $\rho = RS_{tip}/L_{tip}$of the order of $10^6\,\Omega\,cm$ which is in agreement of the literature value $\rho \sim 10^6\,\Omega\,cm$ for CVD diamond [47], where $R = \Delta V/I$.

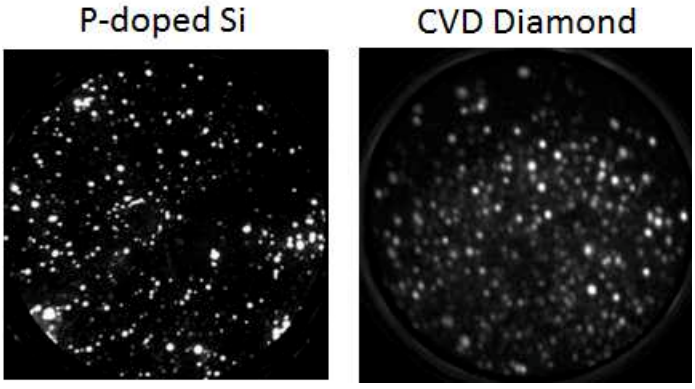

Figure 3.6: On the left, FIM image of p-doped Si [46]; on the right, FIM image of diamond B6 sample.

With the knowledge of the variation of the voltage drop with the laser intensity, using the Equation 3.1 described above, it is possible to calculate the number of carriers inside the sample ($n_c = n_0 + \Delta n_{laser}$) in function of the laser intensity (Figure 3.7), where the value of the carrier mobility has been deducted from literature works [48, 49].

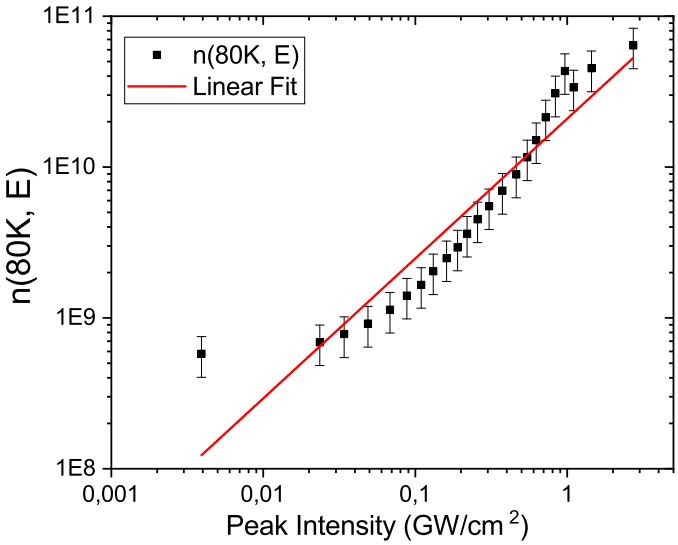

Figure 3.7: Carrier density as a function of the laser peak intensity with the assumption of Ohmic conduction and constant current.

As we can see from the graph, the slope is 0.9 ± 0.1 indicating a 1 photon absorption process. The use of a linear fit is justified by the fact that a constant current approximation makes the points of the curve deviate from the expected behavior. Also the fact that the carrier mobility μ_c is considered to be constant could lead to further errors, while with the change of the internal electric field the carrier mobility also undergoes modifications [49]. Furthermore, the electric field penetration in dielectrics could be high enough and trigger non-Ohmic conduction mechanisms, as will be demonstrated in the following sections.

Since the band gap of diamond is around $5.47\,eV$, we suppose that the absorption process takes place in intra-band levels induced by trap levels and impurities in the material [50].

3.4.2 Change of the voltage drop in function of the laser wavelength

After the study of the dependence of the value of the voltage drop on the laser intensity, other analyses have been carried out changing the laser wavelength. In particular, using the second harmonic generation and the fundamental harmonic of the laser, the dependence of the voltage drop at $\lambda = 515\,nm$ and $\lambda = 1030\,nm$ of laser wavelength has been carried out. For this analysis, another diamond sample has been used (Figure 3.8).

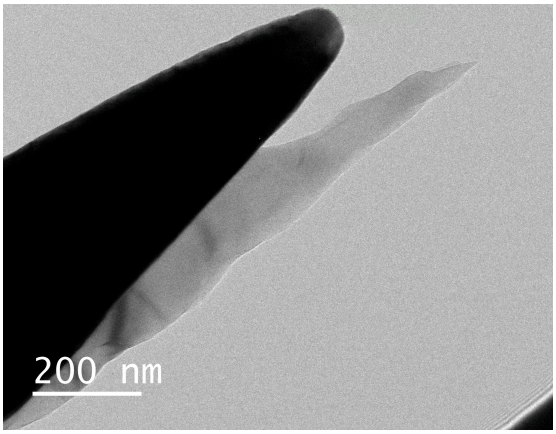

Figure 3.8: Diamond B2.

In this case, being the FIM image at lower potential (around $3\,kV$), and being the voltage drop less big (up to 5% of the applied voltage) respect to the previous case of the sample diamond B6, the method of the radius of the FIM image, as presented in the previous chapter, has been used.

With the measure of the ratio between the radius of the light zone over the radius of all the detector it was possible to monitor the voltage drop along the sample Diamond B2 (Figure 3.9). From Figure 3.9 is clear that the IR laser wavelength ($1.2\,eV$) is much less effective respect to green and UV light. This is probably due to the presence of defect levels inside the Energy Band Gap of CVD diamond ($E_g = 5.47\,eV$) which are easier to excite by photon of higher energy as green and UV compared to IR light where a multi-photon process is necessary [51, 52]. On the other side, the effect on the reduction of voltage drop along the diamond seems similar in the cases of green and UV light illumination (Figure 3.9).

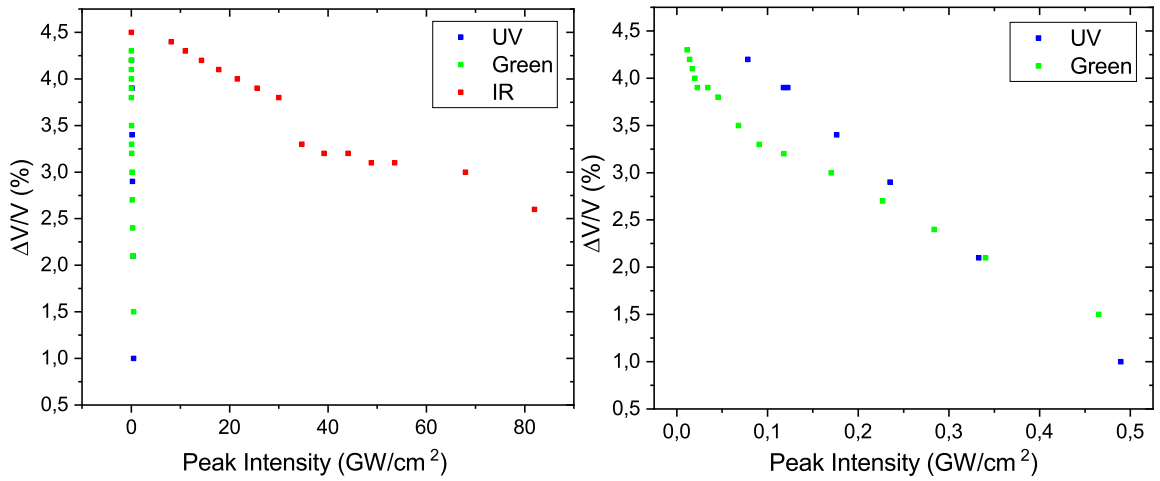

Figure 3.9: Left: voltage drop in function of laser peak intensity for UV ($\lambda = 343\,nm$), green ($\lambda = 515\,nm$) and IR ($\lambda = 1030\,nm$) laser. Right: voltage drop in function of laser power for UV and green laser ($V_{applied} = 7.43\,kV$, laser frequency $100\,kHz$ with pulse duration of $500\,fs$).

3.5 I-V measurements on CVD diamond using FIM

With the implementation of a pico-amperometer connected to the phosphorous screen of the FIM detector, the I-V characteristic of the specimens has been acquired in function of different parameters, such as the chamber gas pressure, temperature, applied voltage and laser illumination.

For these studies, the sample shown in Figure 3.10, has been welded on a tungsten support with the use of Pt in Focused Ion Beam (FIB). As it is clear from the picture, the diamond has been mounted along the W side, in order to have the possibility of screen the metal-diamond junction and check if it plays an important role in the case of laser illumination, since in FlexTAP the laser spot size is big enough to illuminate the whole diamond sample (about $50\,\mu m$ of laser spot size radius at $1/e^2$).

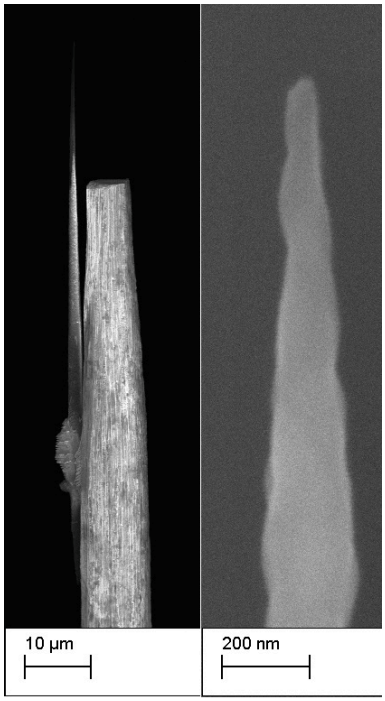

Figure 3.10: Diamond HJ, length $L_{tip} \sim 50\,\mu m$ from the welded point, part outside the shadow of W pre-tip $\sim 22\,\mu m$, tip apex $\sim 20\,nm$.

3.5.1 I-V characteristic

Using the same method as in the case of the sample B6, the voltage present at the apex of the tip V_{apex} has been measured as well as the current flowing through the tip I_{tip},thanks to the pico-amperometer on the phosphorous screen, in order to investigate the conduction properties of the diamond needles. As explained above, this I_{tip} is equal to the rate of gas atom ionization at the surface of the apex. The current flowing through the sample can be controlled by changing the gas pressure inside the chamber, where higher pressure is translated in a higher ionization rate, or by increasing the applied voltage on the tip $V_{applied}$, where a higher field on the surface of the apex increase the probability of gas ionization.

With the combination of these two methods, a wide range of current can be probed (Figure 3.11).As its clear from the graph in Figure 3.11, there is no difference in the measurements done by varying the gas pressure inside the chamber and the applied potential since the two measurements overlap.

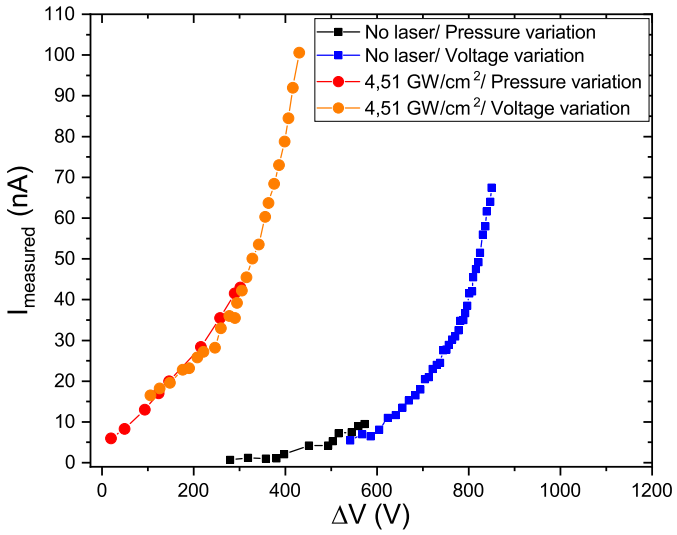

Figure 3.11: Variation of the measured current $I_{measured}$ as a function of the voltage drop ΔV at $T = 80\ K$.

In this case, the measured current $I_{measured}$ is well higher than the real current flowing through the specimen I_{tip}because of the amplification due to the presence of MCPs before the phosphorous screen of the detector. The measured current is proportional to the real current flowing inside the tip, through the following relation:

$$I_{measured} = A_{FOV} \cdot G_{MCP} \cdot I_{tip} \tag{3.2}$$

where $A_{FOV} = 0.3$ is the proportional factor due to the field of view of the instrument (not all the ionized gas ions are collected on the detector) and $G_{MCP} \in [10^6; 10^7]$ is the gain factor of the MCPs (value based on the data-sheet from the manufacturer).

The I-V characteristics of the diamond tip were measured using FIM both in static emission regime (dark) and dynamic emission regime (under laser illumination). These measurements were carried out probing all the possible range of current (Figure 3.12). The I-V characteristics of the diamond needle are clearly non-linear, but in the small current regime of Figure 3.12(b) the characteristics is closer to linear, similar to the case observed in other isolating materials such as MgO [53]. This linear dependence have increased slope with the increase of the laser power. So in this region of low current the conduction is Ohmic with a voltage drop ΔV which is directly proportional to the current flowing through the sample.

3.5.2 Conduction mechanism

In order to explain the non-linear behavior of the $I - \Delta V$ characteristic in Figure 3.12(a), different conduction mechanisms have been considered such as Schottky barrier effect

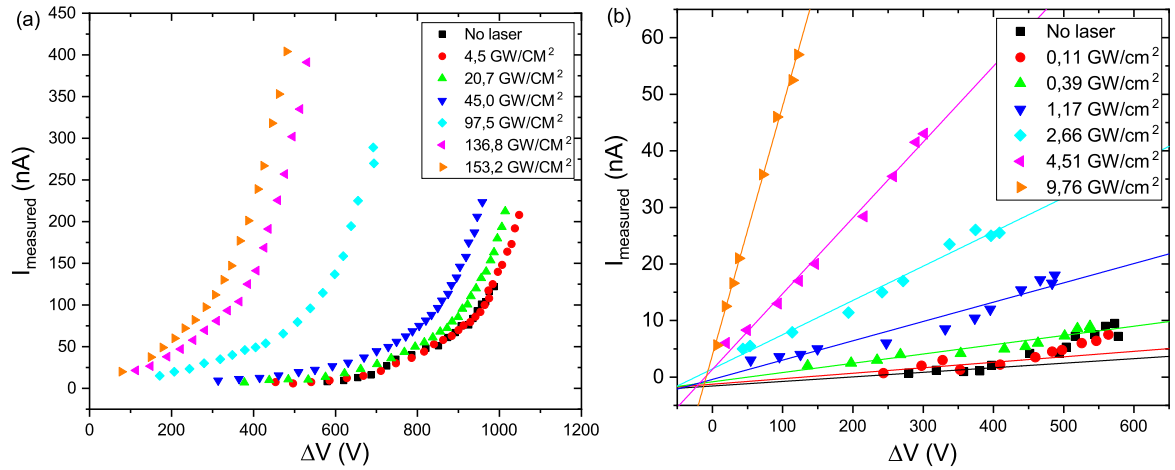

Figure 3.12: $I - \Delta V$ characteristic at $T = 80K$. (a) variation of $V_{applied}$ between 5 and 10 kV at different laser intensities powers (IR $\lambda = 1030\,nm$, and $p_{He} = 4 \cdot 10^{-5}\,mbar$); (b) variation of p_{He} between $10^{-7}$and $5 \cdot 10^{-5}$at $V_{applied} = 5\,kV$and different IR laser powers. The linear fit are of the function $I_{measured} = (1/R_{measured})V_{apex}$, $R_{measured}$ varying from $120 \pm 34\,G\Omega$ (no laser) to $1.8 \pm 0.2\,dG\Omega$ ($28\,mW/cm^2$).

(SB), Fowler-Nordheim injection (FN), Space charge limited conduction (SCLC), SCLC with Poole-Frenkel effect (SCLC+FN), Poole-Frenkel conduction (PF) and Hill's law (HC) [54]. All these different models related to electric conduction in dielectric has been fitted with the analysis data, giving the best fit for the Poole-Frenkel conduction, supported also on previous work on bulk diamond and diamond nano-needles [55, 26]. The Poole-Frenkel conduction, seen as a promotion of carriers into the conduction band by thermally stimulated jumping over a potential barrier thanks to the high electric field, can be written as:

$$I \propto \Delta V \cdot \exp\left(\frac{\beta_{PF}\sqrt{\Delta V} - \phi_{PF}}{k_B T}\right) \tag{3.3}$$

where β_{PF} is the barrier lowering coefficient and ϕ_{PF} is the barrier height of the trap potential related to impurities inside the material.

Since the data fit with the PF model of conduction, the $I - \Delta V$ characteristic should give a linear behavior in the so called "PF coordinates": $\ln(I_{tip}/\Delta V)$ as function of $\sqrt{\Delta V}$. In Figure 3.13, the same data as in Figure 3.12(a) are reported in PF coordinates. In PF coordinates, for each laser intensity, the evolution of $\ln(I_{measured}/\Delta V)$ in function of $\sqrt{\Delta V}$ is linear for high voltages, while at low voltages this behavior becomes non-linear. This allows to conclude that at low voltages, the electrical conductivity deviates from a purely PF law. In fact, as shown in Figure 3.12(b), at low voltages there is an Ohmic contribution, which explains the horizontal asymptotic trend of the data of Figure 3.13(a). In particular the ratio $I_{measured}/\Delta V$, which is proportional to the conductance

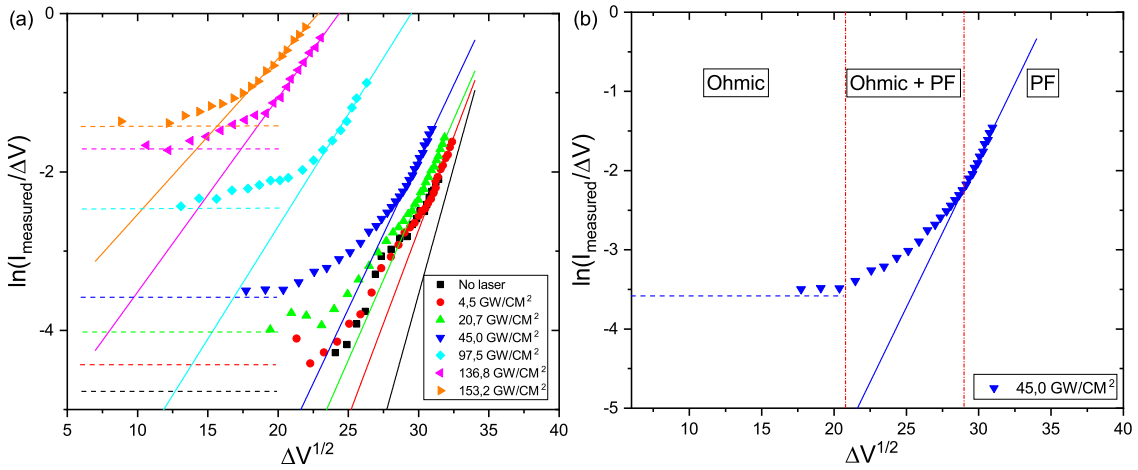

Figure 3.13: (a) I-ΔV characteristic of the data presented Figure 3.12(a) represented in PF coordinates at $T = 80\ K$, $p_{He} = 4 \cdot 10^{-5}\ mbar$ at different laser intensities(IR $\lambda = 1030\ nm$) and varying $V_{applied}$ from 5 to 10 kV. The lines correspond to linear fits by the function :$ln(I_{measured}/\Delta V) = A + B\sqrt{\Delta V}$; (b) conduction zones corresponding on purely Ohmic conduction (left part), mixed Ohmic-PF conduction (central part) and purely PF conduction (right part).

of the sample, does not depend on the electric field and it is reported in Figure 3.13(a) as horizontal dash lines, for each laser intensity.

Since we found two different electric conduction mechanisms, the current flowing inside the sample can be written with the following equation:

$$I_{measured} = \frac{\Delta V}{R_{measured}} + A\Delta V exp\left(B\sqrt{\Delta V}\right) \tag{3.4}$$

where $R_{measured}$, A and B are parameters which depend on the material and geometry of the sample. The first addend corresponds to the Ohmic law while the second is related to Poole-Frenkel conduction model.

3.5.2.1 Conduction mechanism modellization

These two-conduction mechanisms can be modeled as a two parallel resistances: one constant resistance (Ohmic) and one differential resistance which is field-dependent (PF), as shown in Figure 3.14.

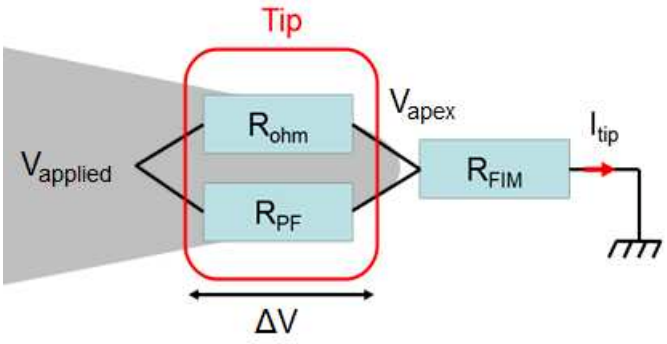

Figure 3.14: Electrical equivalent modellization for the conduction process inside diamond nano-needles.

Using Equation 3.4 to fit the data reported in Figure 3.13(a), we obtain unrealistic values of the parameters $R_{measured}$, A and B. This is due to the fact that the conduction process can be described by Equation 3.4 only when the internal electric field is constant over the entire sample, such as in the case of flat layers or nano-wires with constant cross-section. In our case, due to the needle shape of the diamond samples, the field distribution is not uniform along the specimen. Therefore, the transition between Ohmic and PF conduction in Figure 3.13(a) is smoother than what is reported in literature for bulk diamond, as shown in 3.13(b), where the three regions corresponding to the purely Ohmic, purely PF and mixed conduction are identified, for a given laser intensity. For each value of laser intensity, the $R_{measured}$ parameter is obtained from the fit of the data in Figure 3.12(b), while the parameters A and B are obtained from the data in Figure 3.13(a).

3.5.2.2 Geometrical consideration in the conduction model

In order to describe the field distribution along the diamond needle, we propose a one-dimensional (1-D) model of the conduction process inside the sample, considering its geometrical shape. The needle (with a radius on the apex r_{apex} and a shank angle α) can be described as an assembly of small cylinders of height dz and radii $r(z)$ as represented in Figure 3.15. After neglecting the surface contribution to the conduction, the first step in our modellization is to consider a constant resistivity $\rho_{measured}$ for all the cylinders. Considering that at high applied voltages the electric field is screened at the surface, on a depth of less than 1 nm, we assume a constant carrier density in every cylinder equal to the equilibrium value for the material [42].

With these suppositions, in the case of a truncate cone, we calculate the tip resistance using:

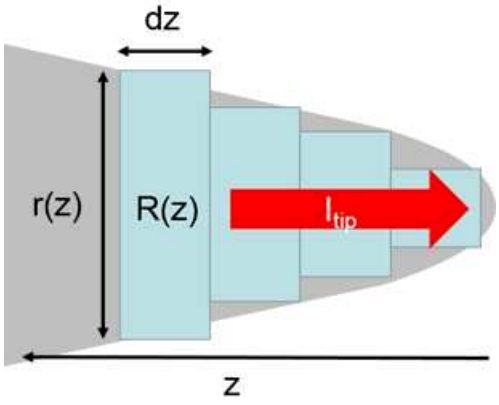

Figure 3.15: 1-D schematic of the tip for the conduction model. Each cylinder of radius $r(z)$ has an electrical resistance $R(z)$.

$$R_{measured} = \frac{\rho_{measured}}{\pi r_{base} r_{apex}} L_{tip} \tag{3.5}$$

where r_{base} is half the thickness at the base of the needle and L_{tip} is the length of the sample.

As discussed above, fitting the experimental data we obtain the parameters $R_{measured}$, A and B, for each laser intensity. In dark, without laser illumination, the value of $R_{measured}$ is $120 \pm 34\, G\Omega$. Considering the geometry of the sample ($r_{apex} = 50\, nm$ $L_{tip} = 50\, \mu m$ and $\alpha = 2°$), a value of $\rho_{measured} = 357 \pm 100\, \Omega\, m$ is calculated from Equation 3.5.

The resistivity of the diamond needle is then given by $\rho_{diamond} = \rho_{measured}/A_{FOV} \cdot G_{MCP}$. Based on the MCP data-sheets, G_{MCP} varies between 10^6 and 10^7. Hence, for $A_{FOV} = 0.3$, $\rho_{diamond}$ varies between 10^6 and 10^7 $\Omega\, cm$ which is in agreement with the values reported for annealed CVD diamond in the literature [47, 56].

From the value of $\rho_{measured}$, we are able to compute the local value of ohmic resistance for each cylinder:

$$R(z) = \frac{\rho_{measured}}{\pi r^2(z)} dz \tag{3.6}$$

as represented in Figure 3.16, where $z = 0$ corresponds to the apex of the sample.

Note that the apex region (first few microns) is more resistive than the base region.

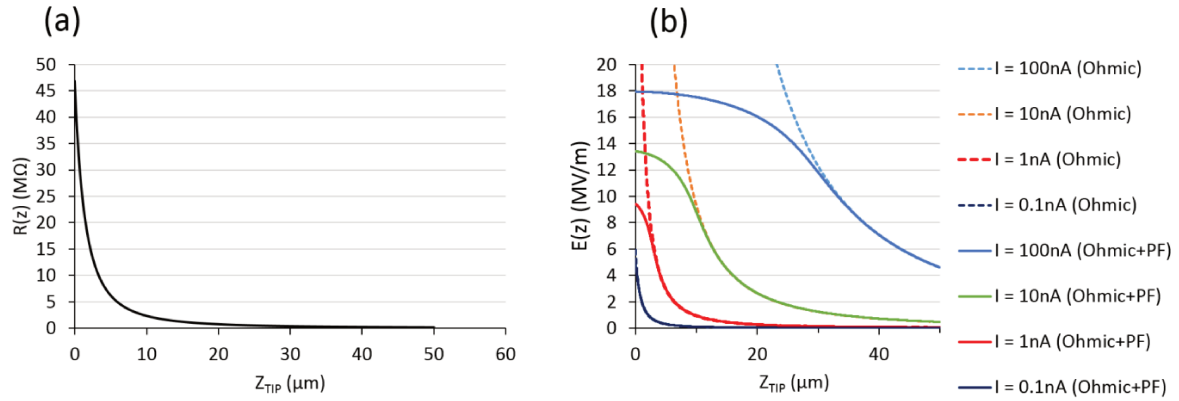

Figure 3.16: (a) Distribution of the resistance $R(z)$ along the tip calculated using Equation 3.6 using steps of $dz = 1\,nm$. (b) Full lines: electrical field distribution E(z) inside the diamond needle for different $I_{measured}$, as calculated using Equation 3.7 with $R_{measured} = 127\,G\Omega$, $A_0 = 1.8 \cdot 10^{-12}$ and $B_0 = 0.035\,V^{-1/2}$. Dashed lines: electric field corresponding to the same values of the current considering only the Ohmic conduction ($A_0 = 0$ and $B_0 = 0\,V^{-1/2}$).

As proven for the case of nano-wires, also in the case of nano-needles, the experimental parameters A and B vary with the tip length as: $A = A_0/L_{tip}$ and $B = B_0/L_{tip}^{1/2}$, where A_0 and B_0 are intrinsic values that depend on the material. The electric field in each cylinder is given by $E(z) = \Delta V(z)/dz$ where $\Delta V(z)$ is the potential difference between the two bases of each cylinder of height dz.

Replacing in Equation 3.4 $R_{measured}$with $R(z)$, ΔV with $\Delta V(z) = E(z)dz$, A with A_0/dz and $B = B_0/\sqrt{dz}$ the current flowing through the specimen (same current flowing inside every cylinder) can be written as:

$$I_{tip} = \frac{\Delta V(z)}{R(z)} + A_0 \frac{\Delta V(z)}{dz} \cdot exp\left(B_0 \sqrt{\frac{\Delta V(z)}{dz}}\right) = \frac{E(z)dz}{R(z)} + A_0 E(z) \cdot exp\left(B_0 \sqrt{E(z)}\right) \tag{3.7}$$

The electric field reported in Figure 3.16(b) has been calculated with the use of Equation 3.7 for different values of current, where $z_{TIP} = 0$ correspond to the position of the apex of the needle. As shown in Figure 3.16(b), different current depending behaviors are reported:

- At low currents ($I_{measured} \leq 10^{-10}\ A$), the field distribution follows the resistance distribution of Figure 3.16(a). The conduction is purely Ohmic and the PF contribution is negligible.
- At average currents ($10^{-10}\ A < I_{measured} < 10^{-7}\ A$) the electric field starts to be strong enough to promote trapped carriers to the conduction band: the PF conduction becomes the main conduction process in the region near the apex of the needle. At the base of the needle, the Ohmic conduction still dominates. The depth where the PF process is dominant increases with the current.
- At high currents ($I_{measure} > 10^{-7}\ A$), the electric field is strong enough to make the PF conduction dominant on a large part of the tip. The Ohmic conduction remains significant only near the base of the tip.

These three current-dependent behaviors correspond to the three areas discussed previously and reported in Figure 3.13(b). The continuous variation of the slope in PF coordinates is the consequence of the local variation of the resistance R(z) inducing a variation of the internal electric field. This transition zone between the two conduction processes with the increase of the current strongly depends on the sample geometry, therefore, it will be different for each needle.

3.5.3 Absorption law and Ohmic resistance

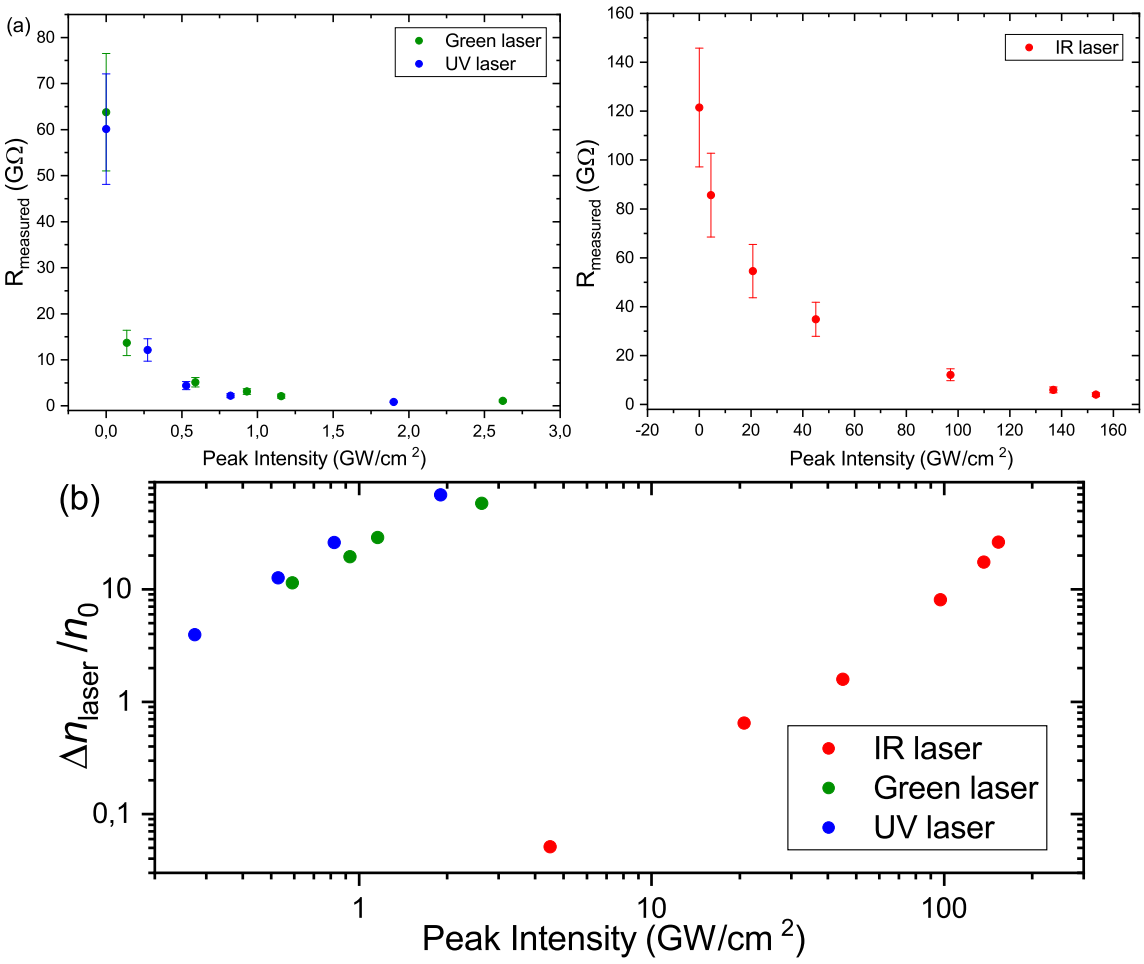

Figure 3.17: (a) Evolution of the measured resistance of the diamond needle at $T = 80\,K$, $p_{He} = 4 \cdot 10^{-5}\,mbar$ for different laser peak intensity and wavelengths (Green,UV on the left and IR on the right). (b) Evolution of $\frac{\Delta n_{laser}}{n_0}$ defined in Equation 3.10 for different laser peak intensity and for the three different wavelengths.

From the value of $R_{measured}$, we can obtain the Ohmic resistance of the tip using the relationship:$R_{tip} = R_{measured} \cdot A_{FOV} \cdot G_{MCP}$.

However, we do not know the exact value of the gain G_{MCP} , therefore we will not discuss the absolute value of the resistance but its variation under laser illumination. As reported in Figure 3.17(a), the resistance decreases under laser illumination, for all three wavelengths (IR, green and UV).From the obtained value for the measured resistance, it is possible to extract the free carrier density inside the material in the absence of laser illumination (n_0) and the excess carrier density induced by the laser (Δn_{laser}). During FIM experiments in FlexTAP, laser pulses of 500 fs duration are sent to the tip with a repetition rate of 100 kHz. Each laser pulse generates a certain density of excess carriers (electrons and holes) whose temporal evolution depends on the photo-absorption and

recombination processes. As already discussed above [46], the carrier density accumulates after several pulses up to a certain equilibrium value $n_c = n_0 + \Delta n_{laser}$ and then it remains constant.

In the case of a cylindrical geometry:

$$R_{measured} = \frac{R_{tip}}{A_{FOV} \cdot G_{MCP}} = \frac{L_{tip}}{e\mu_c n_c S_{tip}} \cdot \frac{1}{A_{FOV} \cdot G_{MCP}} \tag{3.8}$$

and considering that at no laser illumination $n_c = n_0$, the excess of carrier density due to the laser illumination can be expressed as a function of the resistances with and without laser illumination:

$$\Delta n_{laser} = \left(\frac{1}{R_{measured}} - \frac{1}{R_{nolaser}} \right) / \left(A_{FOV} \cdot G_{MCP} \cdot e \cdot \mu_c \cdot \frac{S_{tip}}{L_{tip}} \right) \tag{3.9}$$

Knowing that the only difference between$R_{measured}$ and $R_{nolaser}$ is the difference in the carrier density ($n_{nolaser} = n_0$while $n_c = n_{measured} = n_0 + \Delta n_{laser}$), the ratio between the excess carrier density (created by the laser) and the initial free carrier density (without laser) is:

$$\frac{\Delta n_{laser}}{n_0} = \left(\frac{R_{nolaser}}{R_{measured}} - 1 \right) \tag{3.10}$$

For each laser intensity and laser wavelength, the values of this ratio have been calculated and reported in Figure 3.17(b).

Visible and IR light absorption in diamond involves lattice defects and multi-photon processes. For an absorption process corresponding to the N-photon absorption, the excess carrier density varies proportionally with the laser intensity to the power N: $\Delta n_{laser} \sim I_{laser}^N$. In order to identify the absorption process which occurs in our operating range, we use the slope of $ln\left(\frac{\Delta n_{laser}}{n_0}\right)$ as a function of $ln(I_{laser})$, as shown in Figure 3.17(b). For IR illumination, the value of the slope is $N = 2.0 \pm 0.5$ while for Green and UV illumination $N = 1.5 \pm 0.5$. These values show that for these three wavelengths one and two-photon absorption processes occur in the diamond nano-needle. The band gap of diamond is about $5.47\,eV$ and the photon energy is 1.2, 2.4 and $3.6\,eV$, for IR, Green and UV light, respectively. Therefore, the absorption process is incompatible with a direct valence-conduction band transition. We can conclude that the absorption process is driven by intra-band levels induced by impurities and trapping levels inside the band gap [50, 56].

It would have been interesting to investigate higher laser powers to check for a possible saturation of the absorption of these levels. Unfortunately, above the experimental conditions, the heating of the sample starts to reduce the ionization rate of He atoms significantly and also leads to the direct field evaporation of the C atoms from the specimen.

3.5.4 Laser induced heating

As explained previously, the PF exponential factor B can be extracted from the experimental data. These values are reported on Figure 3.18(a) for different values of the laser intensity and the three wavelengths of the laser. Without laser illumination, B is the same for all datasets: $0.50 \pm 0.05\ V^{-1/2}$ but this value evolves as function of the laser illumination.

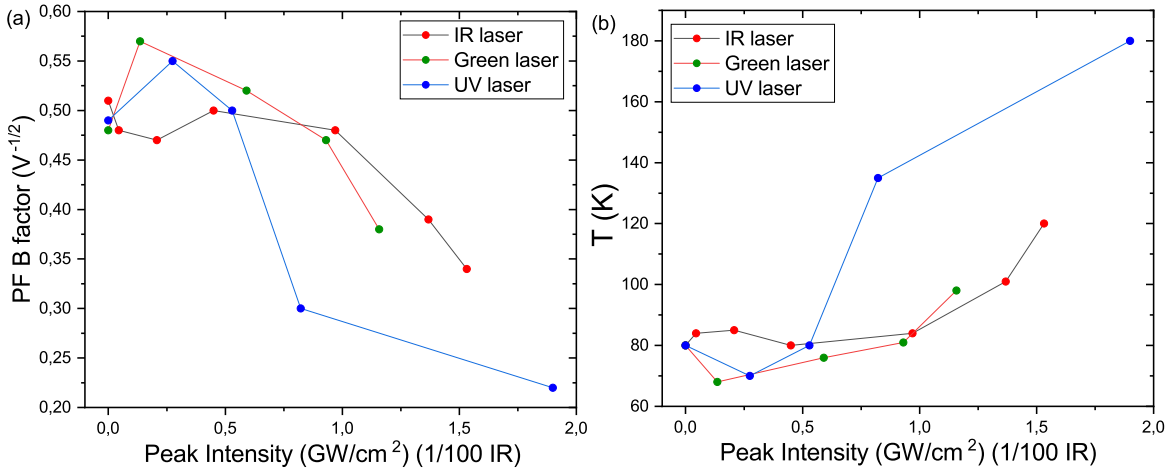

Figure 3.18: (a) Evolution of the Poole-Frenkel factor B and (b) evolution of the temperature T estimated using Equation 3.12, as function of the peak laser intensity and wavelength.

Considering the PF equations, the B factor can be written as$B = B_0/L_{tip}^{1/2}$ where $B_0 = \beta_{PF}/k_B T$ with

$$\beta_{PF} = \sqrt{(e^3/\pi\varepsilon_0\varepsilon_r)d_{PF}} \tag{3.11}$$

where ε_0 is the dielectric constant of the material and d_{PF} the length of the region affected by the PF mechanism. Therefore, B is inversely proportional to $k_B T$. As reported in Figure 3.18(a), the B factor first increases as a function of the laser energy, for UV and green light, or remains constant for IR light. This increase could be related to the geometry of our sample (needle shape) and to the local competition between the two conduction mechanisms (PF and Ohmic conduction). For laser intensities higher than $0.5\,GW/cm^2$ in UV/Green and $100\,GW/cm^2$ in IR, we can see a decrease of the factor B. Considering Equation 3.7, the factor B is inversely proportional to $k_B T$ and also linked to the resistance R through the field distribution $E(z)$. When R decreases, the depth d_{PF} where the PF conduction is dominant is reduced and as a consequence the value of B increases giving $B \propto (T/d_{PF})^{1/2}$. At low laser intensity, the variation of R is fast (Figure 3.17(a)), which can explain the initial increase of B observed for Green and IR wavelengths.

The following decrease of the factor B with the laser intensity is translated in an increase of the temperature since at this laser illumination the variation of R is negligible giving a constant d_{PF}.

Therefore the evolution of T as a function of I_{laser} can be obtained from the values of B as reported in Figure 3.18(b). The variation of the sample temperature after the interaction of the laser can be calculated from the values of B under laser illumination (B_{laser}) and in the dark ($B_{nolaser}$) using the following equation:

$$\frac{\Delta T}{T_0} = (\frac{B_{nolaser}}{B_{laser}} - 1) \tag{3.12}$$

where $T_0 = 80\ K$.

The evolution of T as function of I_{laser} is reported on Figure 3.18(b). At the lowest laser power, the calculated values of T are constant or decrease due to the antagonistic effect of the increase of T and the decrease of the resistance. With the strong approximation of a linear increase of temperature with the laser intensity, where the influence of R is negligible, we obtain $T \sim \alpha I_{laser}$. With the value of α is possible to have an estimation of the mean temperature during conduction starting from $80\ K$. A temperature increase ΔT up to $120\ K$ for UV and Green illumination is reported. These values are in good agreement with previous estimations done in literature using different experimental set-up [18]. Moreover, such a high temperature increase of $100\ K$ can change carriers concentration significantly [55]. Therefore, the two mechanisms: photo and thermal-excitation of carriers will act simultaneously.

3.5.5 Trap level ϕ_{PF} in CVD diamond

Another parameter to discuss is the $A = exp\left(\frac{-\phi_{PF}}{k_B T}\right)$ parameter of the PF Equation 3.3, from which can be extracted the value of the characteristic level barrier of the trap level ϕ_{PF} inside our diamond samples. In order to do this, the above estimation of the temperature is necessary to plot $ln(A) \propto \phi_{PF}/k_B T$ as a function of $1/k_B T$ as reported in Figure 3.19. Reminding the uncertainties from the above assumptions in the estimation of the temperature and the estimation of the value of the factor A, a linear trend appears. From the slope of this trend, an estimation of the the trap level can be done finding $\phi_{PF} = 0.2 \pm 0.1 eV$, which is a comparable value found for the same sample in literature[26].

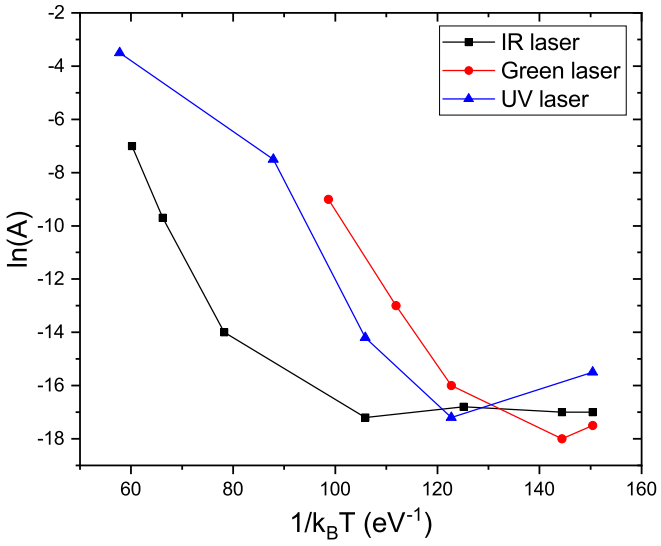

Figure 3.19: Variation of the $ln(A)$ as function of the inverse of the temperature fitted from the variation of B from Figure 3.18

3.5.6 I-V characteristic for a tip with different geometry

In the same conditions, another diamond sample has been analyzed with the FlexTAP instrument. This sample differs with the previous one for its geometrical factors, while its intrinsic properties are kept constant, such as the dielectric constant ε_r, the resistivity ρ, the trapping level Φ and the trap density. In particular, this sample is shorter with a length of $\sim 20\,\mu m$, with radius of the apex of $< 20\,nm$ and lower shank angle of $1^\circ \pm 0.25^\circ$ (other tip has a shank angle of $2^\circ \pm 0.25^\circ$).

As shown in Figure 3.20(a), the transition between the Ohmic regime and the PF conduction is much more sharp for the shorter sample than the previous case (Figure 3.20(b)), and takes place at lower internal electric field ($\Delta V \sim 150\,V$ for the short tip while $\Delta V \sim 400\,V$ for the longer one).

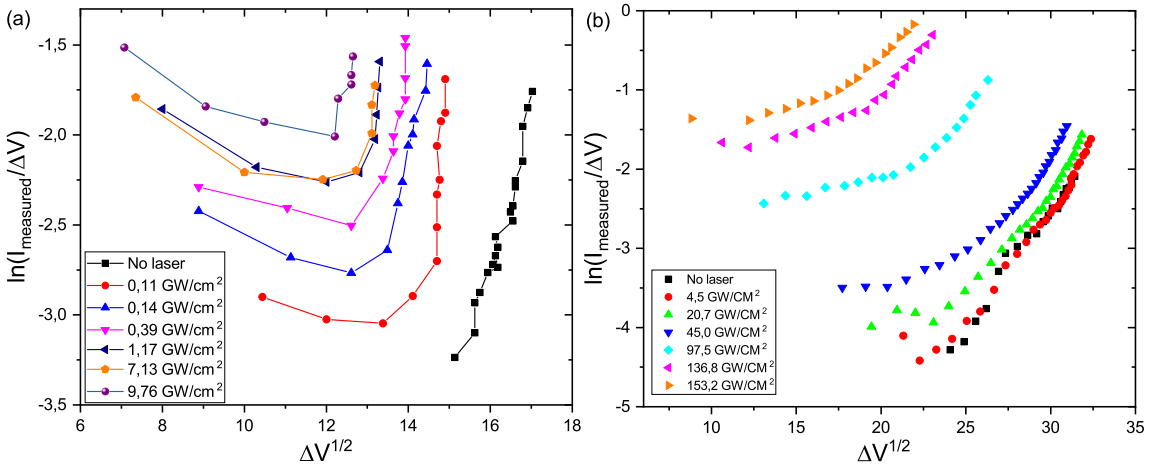

Figure 3.20: $I - \Delta V$ characteristic represented in PF coordinates of the two analyzed diamond needles for different IR laser peak intensities at $T = 80\,K$. (a) Shorter tip (length $\sim 20\,\mu m$, apex $< 20\,nm$, shank angle $1° \pm 0.25°$),$V_{applied} = 8\,kV$ andp_{He} between $10^{-6}$and $5 \cdot 10^{-5}\,mbar$; (b) Previous tip (length $\sim 50\,\mu m$, apex $\sim 20\,nm$, shank angle $2° \pm 0.25°$), $V_{applied}$ between 5 and $10\,kV$.

In order to discuss the difference in the behavior of the two tips, the two conduction mechanisms inside the needle have to be taken into account. Since there is a competition between the two conduction processes, the distance d_{PF} in Equation 3.11, does not correspond to the sample length in the case of a conical geometry due to the strong geometrical effects related to the variation of the resistance inside a cone (Figure 3.16(a)). The depth where the PF conduction takes place is mainly influenced by the shank angle of the cone and the current that flows inside the sample. So, for a needle-like shape, Equation 3.7 can be rewritten as follows:

$$I_{tip} = \frac{E(z) \cdot S(z)}{\rho} + A'(T, \phi_{PF}) \cdot E(z) \cdot exp\left(B'(T, \varepsilon_r) \cdot \sqrt{E(z)}\right) \tag{3.13}$$

with $A' = \frac{AL_{tip}}{exp\left(\frac{\phi_{PF}}{k_B T}\right)}$, $B' = \frac{e^{3/2}}{k_B T \sqrt{\pi \varepsilon_0 \varepsilon_r}}$ and where $S(z)$ is the section of the tip along the z direction.

Regarding Figure 3.20, the conduction mechanism without laser illumination is PF because the resistivity is so high that a small flowing current induces an internal electric field strong enough to free carrier from the trap levels. On the other hand, the laser illumination generating free carriers reduces the resistivity making possible the investigation of the threshold where the two conduction mechanisms compete to the conduction. For the shorter tip, this transition is sharp while for the longer tip it is smoother. Comparing the voltage drop between the two needles in the case of the same flowing current (same gas pressure) a ratio $^{\Delta V_2}/_{\Delta V_1} = 0.72 \pm 0.05$ is found which implies that the radius of curvature at the apex r_2 is larger than r_1 of approximately the same ratio. Furthermore, we know

that Tip1 is shorter and has a lower shank angle. Considering these geometrical factors and Equation 3.13 we can conclude that:

- a smaller radius of curvature implies a higher resistance at the apex with the consequence that the PF conduction is dominant at lower currents. Note that the internal electric field has to be at a certain intensity in order to activate PF conduction.
- A shorter tip has a lower voltage drop threshold required for the PF conduction. In fact the same electric field is necessary which means that shorter tips need less voltage drop to achieve it.
- A smaller shank angle reduces the variation of $R(z)$ making the transition between Ohmic and PF conduction faster. In fact, a nano-wire with 0 shank angle presents a homogeneous internal electric field and constant $R(z)$.

The experimental observation of the two different samples are in agreement with these three points, such as lower voltage drop threshold and sharper transition for the smaller tip.

Another difference to consider is the fact that at low voltages, in the case of laser illumination, for the shorter tip the ratio $I_{measured}/\Delta V$, which is proportional to the conductance of the sample, is not constant as it should be in the case of Ohmic conduction (Figure 3.20(a)). In PF coordinates, the $ln(I_{measured}/\Delta V) = -ln(R_{measured})$ is plotted in function of the voltage drop and in the case of Ohmic conduction is constant due to the fact that the Ohmic conduction is field independent. Moreover, the contribute of the PF conduction decreases the effective resistivity of the sample, meaning that $-ln(R_{measured})$ should increase. In Figure 3.20(a), at low voltage drop there is the opposite trend, that is $-ln(R_{measured})$ decreasing with the increase of ΔV. These behaviors can be taken into account with the use of an different possible process that has not been taken into account in the rest of this study due to its limited influence and its difficulty in a quantification from our results. In CVD diamond, where a high density of deep trap is reported (between 0.55 and 0.4 eV with a density up to $10^{16}\ cm^{-3}$), the probability of a free carrier to be trapped is a function of the rate of generated carriers and the applied electric field [55]. It is also reported that the density of occupied trap increases with the electrical field until the field $E_{PF} = 10^5\ V/m$. For $E > E_{PF}$, the strong field detraps the carriers and induces the Poole-Frenkel conduction. Below this value, since there is an increase of trapped carriers, the density of free carriers decreases with the increase of the internal electric field leading to an increase of resistivity of the sample before the prevalence of the PF effect at high electric field.

3.6 Field Emission Microscopy for the study of electrical conduction properties

The other technique largely used in this work of thesis is Field Emission Microscopy (FEM), where it is studied the emission of electron into vacuum with the application of a negative bias voltage on the samples which have the same geometrical shape as in the case of FIM (nano-objects with radius of curvature at the apex below the hundred of nanometers). As described in Chapter 2, this instrument has been used with the use of different detectors and also with the use of femto-second laser pulses in the IR domain.

A collaboration with colleagues of the LCAR laboratory of the University of Toulouse has shown the possibility of the study of diamond electrical conduction using field emission. In this case the conduction characteristic of diamond tips has been studied in static regime while interesting emission effects with IR laser illumination ($\lambda = 1030\,nm$, $300\,fs$ pulse duration) has been discovered.

Afterwards with the use of the Argus Spectrometer in static regime (without laser illumination), which had to be calibrated in a preliminary study on Tungsten, the electron energy deficit can be measured along with the emitted current retrieving also here the $I - \Delta V$ characteristic of the specimens.

With the use of FEM, the range of exploitable currents is even wider respect to the FIM case and the emission law of electron into vacuum is well known (Fowler-Nordheim theory FN), as opposite to the ionization process which takes place in FIM analysis. Also as in the case of FIM, FEM analysis is a non-destructive technique compared to APT. Another difference with FIM measurements is that FEM does not need cryogenic temperatures of the sample but can theoretically operate at all temperatures.

3.7 FEM on CVD diamond

As for the case of FIM, various diamond tips have been observed in FEM. A first study has been done in collaboration with the LCAR laboratory of the University of Toulouse. The experimental set-up in Toulouse is equipped with a vacuum chamber with a pressure of the order of $\sim 10^{-10}\, mbar$. The samples, prepared in Rouen, are mounted on three dimensional nano-positioning translation stages, used for the positioning of the sample into the laser focus. A femto-second IR laser ($\lambda = 1030\, nm$, 300 fs pulse duration) illumination can be applied on the apex of the diamond needle with the use of a spherical silver mirror (focus length of $4.5\, mm$) inside the chamber. This mirror allows a laser focus waist of around $5\, \mu m$. A pinhole of $700\, \mu m$ is positioned in front of the specimen and the emission current can be measured counting electrons with a multi-channel plate or with the use of a pico-amperometer connected to the tip holder. The electron kinetic energy can be obtained with the use of a flat retarding field spectrometer which has poor resolution resulting in the measure of only the mean kinetic energy instead of the specific shape of the energy spectrum. At high currents, the measure of it can be done with the use of a pico-amperometer isolated from the ground potential and plugged on the sample.ollo9

In the GPM laboratory, other diamond needles have been studied in static regime (no laser illumination) with the use of the Argus Spectrometer. This high resolution detector, beside the measure of the voltage drop and emission current, can acquire high resolution spectra adding the shape of the spectrum to the available information.

3.7.1 Diamond conduction studies in Toulouse laboratory

The first study on diamond conduction with the use of FEM has been made in the LCAR of Toulouse. In these series of measurements a diamond tip prepared with Platinum welding has been used (Figure 3.21).

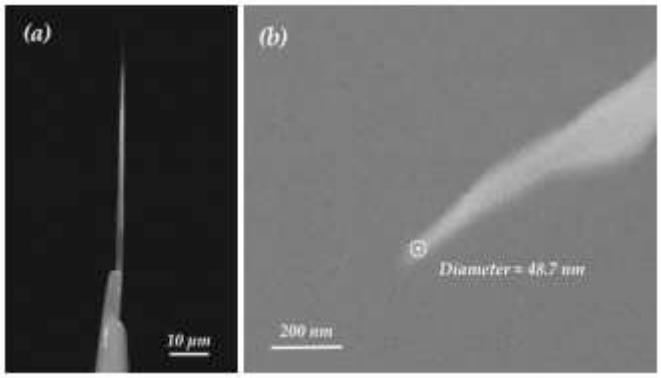

Figure 3.21: SEM images of the diamond needle used in Toulouse. (a) Needle welded on tungsten using FIB. (B) apex image with radius estimation. Length $\sim 70\,\mu m$, tip apex $\sim 20\,nm$.

Compared to FIM, in field emission the applied voltages are negative. For simplicity, all the following voltages, if not specified, are negative but will be written omitting the minus sign.

Before each series of measure, the tip have been cleaned with the use of a positive voltage of $2.5\,kV$ (maximum available) in order to evaporate the dirt accumulated on the surface of the sample, aided by a laser illumination. This method showed no evidence of tip modifications thanks to the high transparency of diamond to IR light.

As in the case of FIM, the tip showed a voltage drop $\Delta V = V_{applied} - V_{apex}$ during electron emission. At first we measured the emitted electric current as well as the electron kinetic energy as a function of the applied potential. With the knowledge of the $I - \Delta V$ characteristic it is possible to obtain, as done in the FIM case, the conduction mechanism of the specimen. On the other hand, since the law for electron emission is well known and studied (Fowler-Nordheim), it is possible to also obtain the emission characteristic of the diamond nano-needle. As said above, the voltage present on the apex of the tip is directly obtainable through the mean energy of the kinetic energy spectrum, while the current can be obtained by MCP counting for low current and with the use of a pico-amperometer which has an error, given by the background noise, of few tens of pA. Doing so, the $I - \Delta V$ characteristic can be plotted as well as the emission current as a function of the applied voltage (Figure 3.22).

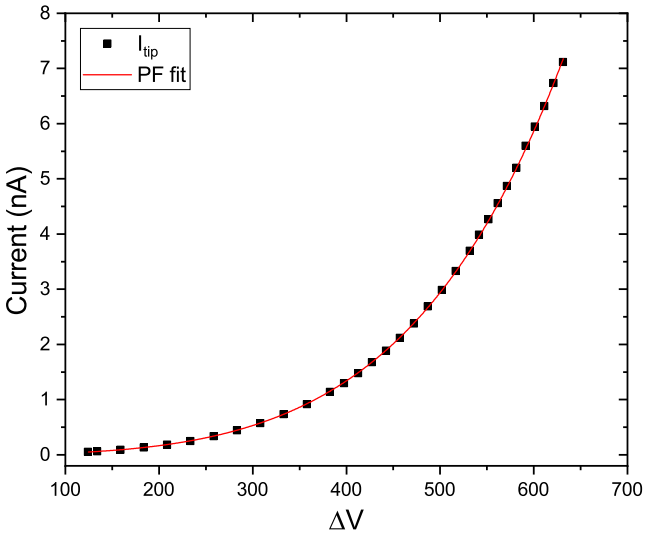

Figure 3.22: $I - \Delta V$ characteristic of the diamond needle F16, taken at ambient temperature and with a variation of $V_{applied}$ between 400 and 1400 V.

From the graph in Figure 3.22, it is evident that the emission current rises exponentially with the applied voltage. As in the case of FIM, we tried to fit the data with various models finding also in this case the best fit for PF mechanism of conduction.

Another interesting curve to plot is the evolution of the voltage drop in function of the applied voltage (Figure 3.23).

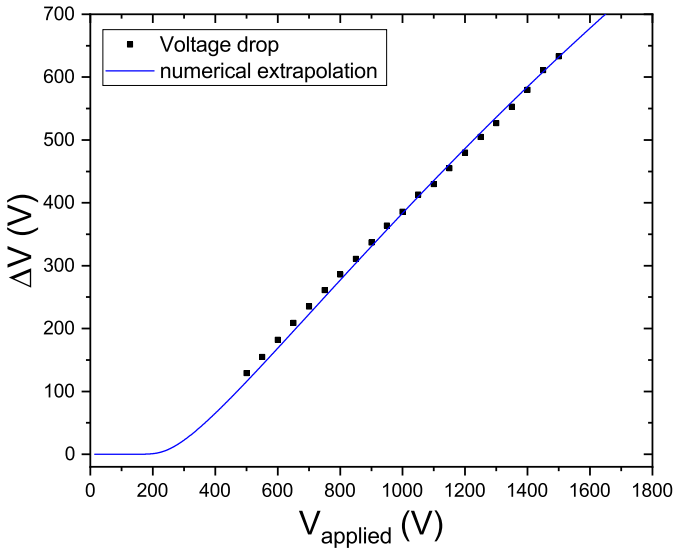

Figure 3.23: Measurement of the voltage drop ΔV as a function of the applied voltage $V_{applied}$ and corresponding computed values from Equation 3.16.

From this graph, it is clear to note that the evolution of the voltage drop follows a linear behavior with a slope of 0.497 ± 0.003 and a negative intercept of $(-134 \pm 3)\, V$.

3.7.1.1 Conduction model

As in the previous case with the measurements made by FIM, we can use a simple model in order to explain the evolution of the current and the voltage drop respect to the applied voltage. We know that two different mechanisms are simultaneously taking place in the emission process. Inside the diamond sample we have the PF conduction mechanism taking place, while at the diamond-vacuum junction the FN emission behavior occurs.

These two effects can be modeled as two resistances in series, in which the same current I_{tip} is flowing as shown in Figure 3.24.

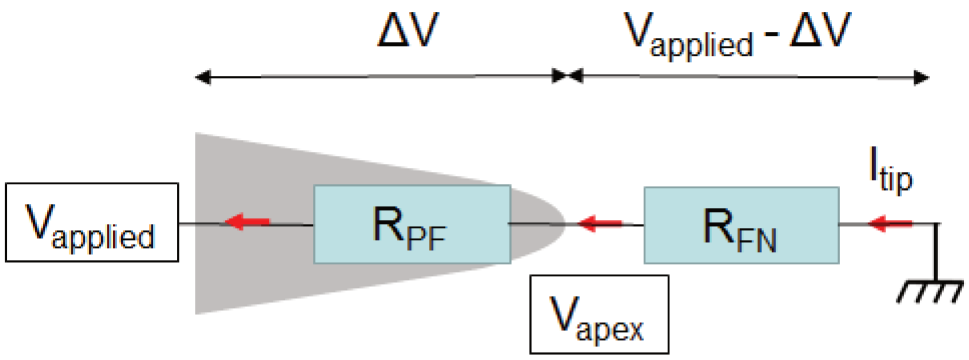

Figure 3.24: Electrical equivalent model for the emission current from diamond nano-needles. The PF and FN dipoles are in series so that the emitted current obeys both laws with corresponding potential difference ΔV and $V_{apex} = V_{applied} - \Delta V$ respectively.

As discussed above, the conduction inside the diamond needles, without laser illumination, follows the PF law of conduction which can be expressed as:

$$I_{tip} = A\Delta V \cdot exp(B\sqrt{\Delta V}) \tag{3.14}$$

where A and B are parameters which depend on the tip characteristic and temperature.

On the other hand, at the diamond-vacuum junction, electrons are emitted into vacuum by field emission with a FN behavior which depends on the electric field present on the apex of the tip E_{FN}. As in the case of metallic emitters, we can link the electric field to the potential present on the apex of the tip, taking into account the voltage drop, writing $E_{FN} = \beta(V_{applied} - \Delta V)$. β (expressed in m^{-1}) is a parameter which describes the field enhancement at the apex of the sample. In first approximation, we can consider β to be constant not depending on $V_{applied}$ or ΔV. This is a strong hypothesis since a dielectric emitter could lead to field penetration and the presence of PF conduction which, as discussed above, leads to a non homogeneous electric field inside the sample (Figure 3.16(b)). This non-linearity of the field, since it depends on the current flowing inside the

sample, can affect the shape of the equipotential lines at the apex translating in a possible modification of the β factor. We can therefore write the FN current as:

$$I_{tip} = CV_{apex}^2 \cdot exp\left(-\frac{D}{V_{apex}}\right) \tag{3.15}$$

where C and D are parameters which depend on the local work function φ on the apex of the sample and it enhancement factor β and can be considered approximately constants.

Since these two phenomena are present simultaneously and the emission current is also the current flowing through the diamond, we can write:

$$I_{tip} = A\Delta V \cdot exp(B\sqrt{\Delta V}) = CV_{apex}^2 \cdot exp\left(-\frac{D}{V_{apex}}\right) \tag{3.16}$$

Using Equation 3.14 and 3.15, the experimental data of the $I - \Delta V$ characteristic are plotted in PF coordinates as well as in the so called "Fowler-Nordheim coordinates": $\ln\left(I_{measured}/V_{applied}^2\right)$ as function of $1/V_{applied}$, where in the case of field emission a linear behavior is expected, and they are shown in Figure 3.25I:.

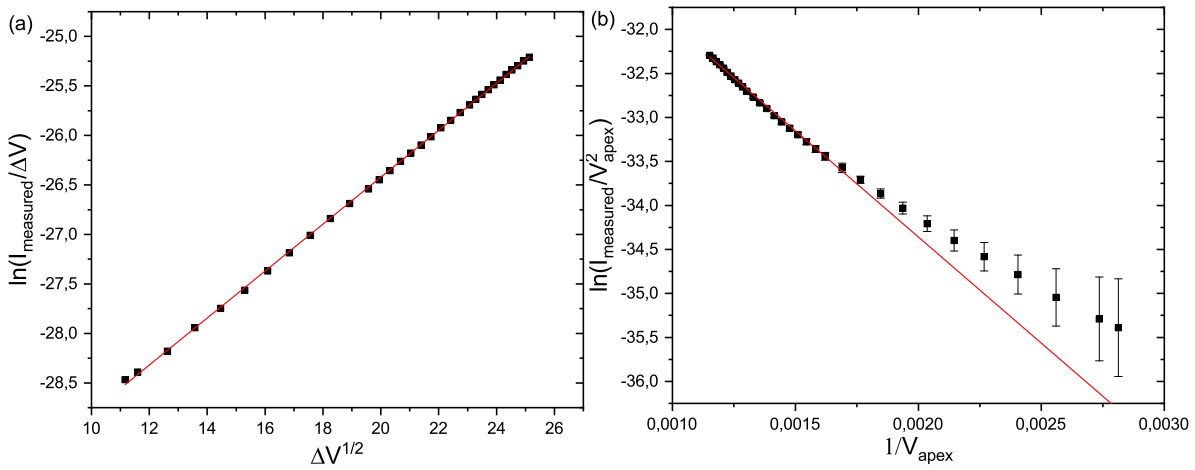

Figure 3.25: (a) $I - \Delta V$ characteristic of the data presented in Figure 3.22. (a) Represented in PF coordinates. (b) The same data plotted in FN coordinates as a function of V_{apex}which is linked to the electric field at the diamond-vacuum junction.

The PF fit gives $A = (2.9 \pm 0.3) \cdot 10^{-5}\, nA/V$ and $B = (0.238 \pm 0.004)\, V^{-1/2}$ while the FN fit gives $C = (1.5 \pm 0.7) \cdot 10^{-4}\, nA/V$ and $D = (2410 \pm 50)\, V$. Using these values of the parameters A, B, C and D Equation 3.16 can be numerically solved in order to find the expected value of ΔV as a function of $V_{applied}$. This estimation of the expected voltage drop can be visualized by the solid line of Figure 3.23, as well as the fit of the PF and FN plots shown in solid lines in Figure 3.25. As one can see, this estimation of ΔV and the fits of the PF and FN plots are in good agreement with the measurements. A little

discrepancy is present in Figure 3.25 between the fits and the experimental data which can be related to modification of the value of the β factor which is considered constant in Equations 3.15 and 3.16.

As similarly done in the FIM case, from the fit of the PF plot, some numerical value for physical parameters on the diamond tip can be obtained. Equation 3.3 gives the Poole-Frenkel expression for the flowing current where $\beta_{PF} = \sqrt{(e^3/\pi\varepsilon_0\varepsilon_r)d_{PF}}$. The fit parameter $B = \beta_{PF}/k_BT$ can be used in order to find an estimation of $\varepsilon_r d_{PF} \sim 150\,\mu m$. Taking into account the bulk value of the diamond dielectric constant $\varepsilon_r = 5.7$ [57] we obtain a $d_{PF} \sim 27\mu m$ as the region inside the tip near the apex where the PF effect takes place. Since d_{PF} appears to be shorter than the sample dimensions, this discrepancy can be explained by the presence of amorphous conductive carbon layers on the surface which makes a part of the tip conductive, since there is no evidence of a contribution by Ohmic conduction.

On the other hand, the FN parameter

$$D = \frac{4\sqrt{2m}}{3\hbar e}\varphi^{3/2}\upsilon(y)\frac{1}{\beta} \tag{3.17}$$

where m is the mass of the electron and $\upsilon(y)$ a slowly varying mathematical function of the Nordheim parameter $y = \frac{1}{\varphi}\sqrt{\frac{e^3\beta V_{apex}}{4\pi\varepsilon_0}}$ [58]. Many modern papers on field emission assume the $\upsilon(y)$ to be constant and equal to 1, which could lead to an error in the prediction of the current density by a factor 100. In this work, we assume a value $\upsilon(y) = 0.58$ which is the value obtained for a material with $\varphi = 4.5$ under an electric field $E = 5\,V/nm$ [59]. From other works on the work function of diamond $\varphi \sim 5\,eV$ and the value $D = 2410\,V$ from the fit of the FN plot, we obtain $\beta \sim 1.8 \cdot 10^7\,m^{-1}$. If one takes into account only the tip geometry in order to estimate the enhancement factor β, since in first approximation $\beta = 1/(kr_{apex})$ with the coefficient $k \sim 5$ for long tips supported on a distant conducting base and placed near the anode [60], with the radius of the apex of our tip $r_{tip} \sim 20nm$ the value $\beta = 1 \cdot 10^7\,m^{-1}$is obtained. These two values are different from each other. This can be explained by the fact that the analysis data are in a range of applied voltage where the current is saturated compared to the metallic case because of the field penetration effect and a possible presence on a depletion region on the apex of the tip. This produces a limitation in carriers supply which reduce the increase of current with the applied voltage resulting in a saturation of the FN curve. At lower voltages, where the FN curve is linear, has a higher slope resulting in a lower enhancement factor β which its value will be closer to the one estimated from the geometry of the emitter. In many experimental cases on non conducting materials, this low voltage linear region has so low emission current and sometimes the sensitivity of the apparatus is not enough to see it.

Since the current follows the PF mechanism and the FN emission regime (Figure 3.24), two differential resistances can be defined for the two mechanisms:

$$R_{PF} = \Delta V / I_{tip} = (1/A) \cdot exp(-B\sqrt{\Delta V}) \tag{3.18}$$

and

$$R_{FN} = V_{apex} / I_{tip} = \frac{1}{CV_{apex}} \cdot exp\left(\frac{D}{V_{apex}}\right) \tag{3.19}$$

Calculating these two differential resistances using the values for A, B, C and D from the previous fits, the evolution of these two resistances can be calculated as a function of the applied voltage $V_{applied}$ as shown in Figure 3.26.

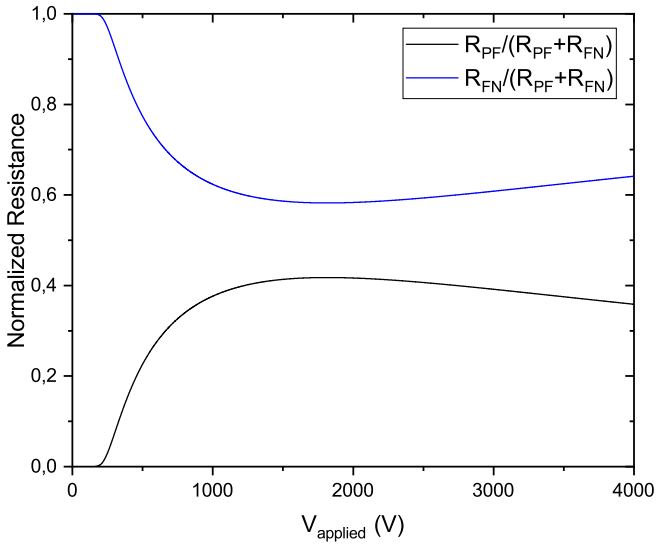

Figure 3.26: Normalized differential PF and FN resistances as a function of the applied voltage $V_{applied}$.

As shown from the graph, between 1000 and 2000 applied volts, the two resistances are almost constant contributing in the same order to the limitation of the current. However, at low applied voltage the current is given almost by the FN resistance which is dominant, since the voltage drop is not big enough to make the PF effect relevant.

At high applied voltages, above 2000 V, instead the graph shows that the PF resistance start to slowly decrease indicating that in this regime the FN mechanism is becoming more relevant.

3.7.1.2 Influence of the parameters to the conduction

As shown by our model, the emission characteristic from diamond, is strongly dependent on the parameter A, B, C and D. A change of these parameters is directly linked to a change of balance between PF and FN in field emission. As shown by other authors,

the PF mechanism is affected by the temperature of the sample through the parameter $B = \beta_{PF}/k_B T$ [26]. Unfortunately, in the experimental setup of Toulouse, it is not possible to cool down or heat up the samples inside the chamber to monitor the evolution of the current with the temperature. Even though an experiment of this type is not possible, through numerical estimation of the voltage drop as a function of the applied voltage is possible to see the effect that each parameter brings to the voltage drop and current behavior. Figure 3.27 shows various curves of the voltage drop as a function of the applied voltage for different value of the factor B (Figure 3.27(a)) and of the factor D (Figure 3.27(b)) keeping constant the other three parameters.

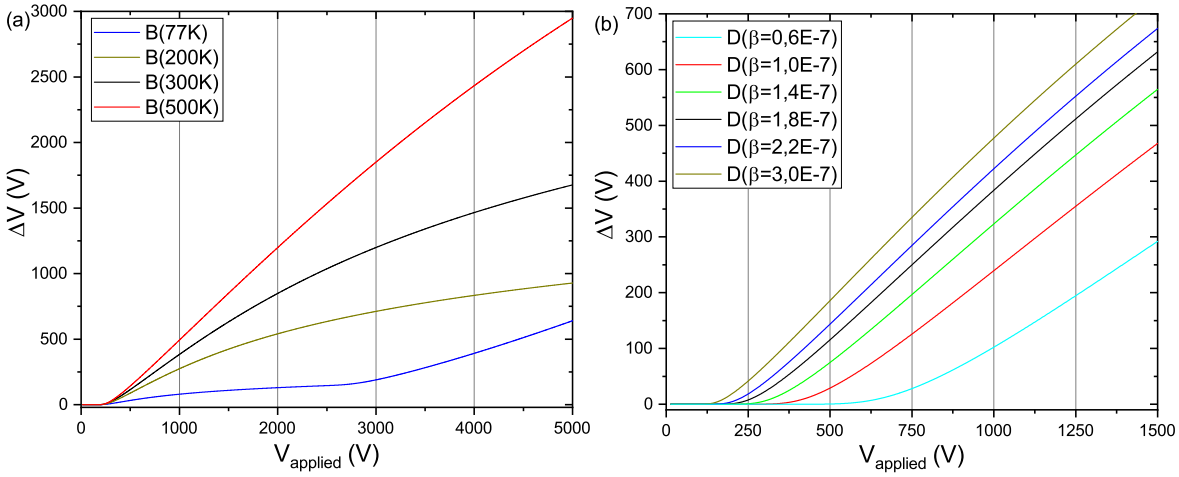

Figure 3.27: Evolution of the voltage drop as a function of the applied voltage for different values of the parameter (a) B and (b) D keeping the other parameters constant.

In particular, as shown in Figure 3.27(a), the voltage drop changes drastically for different temperatures, noting that we assumed the value of β_{PF} to be constant for every internal field of the sample. If the assumption of a β_{PF} constant is correct, it means that the temperature of the sample strongly influences the voltage drop as well as the current. Unfortunately, in experiments is very difficult to probe such wide range of applied voltage to verify the behavior of the voltage drop due to too high emission current that could lead to the breakdown of the sample. On the other hand, the variation of the voltage drop for different value of the D parameter is shown in Figure 3.27(b). In this case, the factor $D \propto \frac{1}{\beta}$ is inversely proportional to the enhancement factor of the tip. As one can see from the graph, for lower enhancement factors the voltage drop starts to appear at higher applied voltage and the slope above $1000\,V$ has a slightly lower value.

3.7.1.3 Laser illumination

Since the enhancement factor is mainly given by the material and geometry of the tip, its value cannot easily change. One method to change this D factor during experiments, is the use of a laser on the apex of the specimen in order to increase the emission current. To do this, a very focused laser on the apex is necessary in order to not affect the PF conduction inside the diamond, but only modifying the emission mechanism. In the Toulouse laboratory, this experiment has been performed with femto-second pulses (300 fs duration, 1030 nm wavelength, 1 MHz repetition rate) and a focal spot of a few micrometers on the apex of the diamond tip. With this, a transition in the emission process has been observed with the increasing of the laser intensity (Figure 3.28).

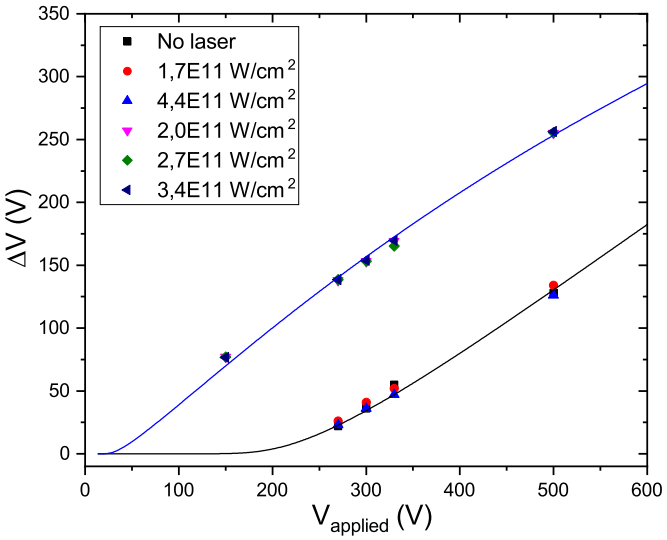

Figure 3.28: $\Delta V - V$ characteristic with and without laser illumination. Above a critical laser power, the voltage drop changes following quasi linear behavior at high applied voltage with a similar slope but very different intercept compared to the static case.

As shown in Figure 3.28, the voltage drop has a critical peak laser intensity of about $1.7 \cdot 10^{12}\ W/cm^2$where the voltage drop regime changes. Below this critical value, the variation of voltage drop with the applied voltage varies following the in dark behavior, while above this threshold there is a linear increase of voltage drop with an intercept close to zero. This can be explained with a decrease of the parameter D resulting in a decrease of the FN differential resistance. As done previously, fitting the data under laser illumination above threshold results in $D = (200 \pm 50)\,V$, around 12 times lower than the value obtained without laser. With the modification of the parameter D, as a consequence also the parameter C varies since $C \propto \frac{\beta^2}{\varphi}$. With the application of laser on the sample, it is not known what is the real consequences of the laser pulses on the mechanism of electron emission. Taking this into account, if we assume that under laser the D parameter is still

$D = \frac{4\sqrt{2m}}{3\hbar e}\varphi^{3/2}\upsilon(y)\frac{1}{\beta}$, then the drop of the value of D could be related to a change of β, change of φ or both at the same time.

3.7.2 Argus spectrometer

Using the Argus Spectrometer on the FEM workbench, various diamond samples have been analyzed without laser illumination due to the fact that a laser was still not installed on the workbench. With the Argus spectrometer, high resolution emission spectra can be obtained, while the emission current can be calculated through the integration of the energy spectra. The spectra Fermi Level E_F gives information of the voltage present on the apex of the tip $V_{apex} = E_F/e$ as shown in Figure 3.29. On the other hand, the emitted current is measured by the integration of the energy spectra.

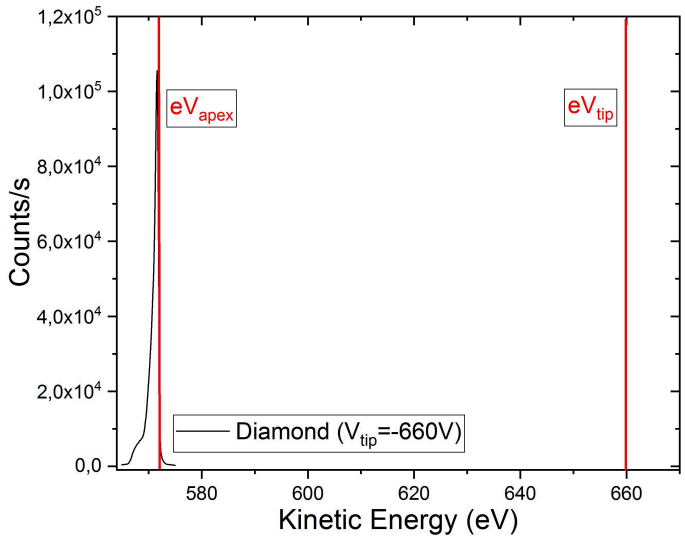

Figure 3.29: Emission spectrum from diamond at applied voltage $V_{tip} = 660V$, the voltage drop causes the Fermi level to be hundred of volts lower than the applied voltage.

The advantage respect to the measurements done in Toulouse, is the fact that the resolution on the spectra is higher consenting to extract new information from the shape of the emission spectra and not only through the information on the I-V curve.

3.7.2.1 Kinetic Energy emission spectra

Following the procedure in [36], from the classical theory of field emission it is possible to calculate the energy distribution of electrons that escape the surface with an energy between ε and $\varepsilon + d\varepsilon$ by:

$$P(\varepsilon) = Bf(\varepsilon, T) \cdot exp(C_V(\varepsilon - E_F) \cdot (1 - exp(C_V(\varepsilon - E_F))d\varepsilon \tag{3.20}$$

with

$$C_V = 2\left(\frac{2me}{\hbar}\right)^{1/2}\frac{\varphi^{1/2}}{E}t(y) \sim 10.25\cdot 10^9\frac{\varphi^{1/2}}{V_{apex}\beta} \tag{3.21}$$

where ε is the kinetic energy of electrons, $f(\varepsilon, T)$ the Fermi-Dirac distribution and E_{apex} is the electric field at the apex of the sample. In Equation 3.21, the effective mass of electron is taken as the free electron one, and with the approximation of the elliptical function $t(y) = 1$ since it slowly varies with y ($t(y)$ is tabulated function, see Table 1.1 of [34]). As in the case of the D parameter for the FN current, $C_V \propto \frac{\varphi^{1/2}}{\beta}$ depends on the emitter work function φ and its enhancement factor β.

In order to extract the value of C_V from the emission spectra, two different method can be used:

- A fit of the low energy side of the spectrum below the Fermi energy, where $P(\varepsilon) \sim B\cdot exp(C_V(\varepsilon - E_F))$, where the Fermi-Dirac distribution can be taken as 1 at these energies.

- A fit of the entire spectrum as a convolution of $P(\varepsilon)d\varepsilon$ at $T = 0K$ approximation with a Gaussian function $exp(-\varepsilon^2/a^2)$which takes into account the resolution of the spectrometer:

$$P(\varepsilon) = B\cdot exp(C_V(\varepsilon - E_F))\cdot[exp\left(\frac{1}{4}C_V^2a^2\right)\cdot erfc\left(\frac{aC_V}{2} + \frac{\varepsilon - E_F}{a}\right) + \\ - exp\left(C_V^2a^2\right)\cdot exp(C_V(\varepsilon - E_F))\cdot erfc\left(aC_V + \frac{\varepsilon - E_F}{a}\right)]d\varepsilon \tag{3.22}$$

  with erfc being the complementary error function. The T = 0K approximation leads in an overestimation of the spectrometer resolution.

The two methods give the value of C_V within 10% of difference.

3.7.2.2 Measurements on CVD diamond

For this study different diamond tips have been analyzed with the use of the Argus spectrometer. For the scope of discussing the conduction mechanism two different samples are taken into account (Figure 3.30).

In order to obtain the $I - \Delta V$ characteristic of the samples, various emission spectra have been acquired at different applied voltages. In Figure 3.31 are reported different energy spectra for the sample D5 taken ad different applied voltages.

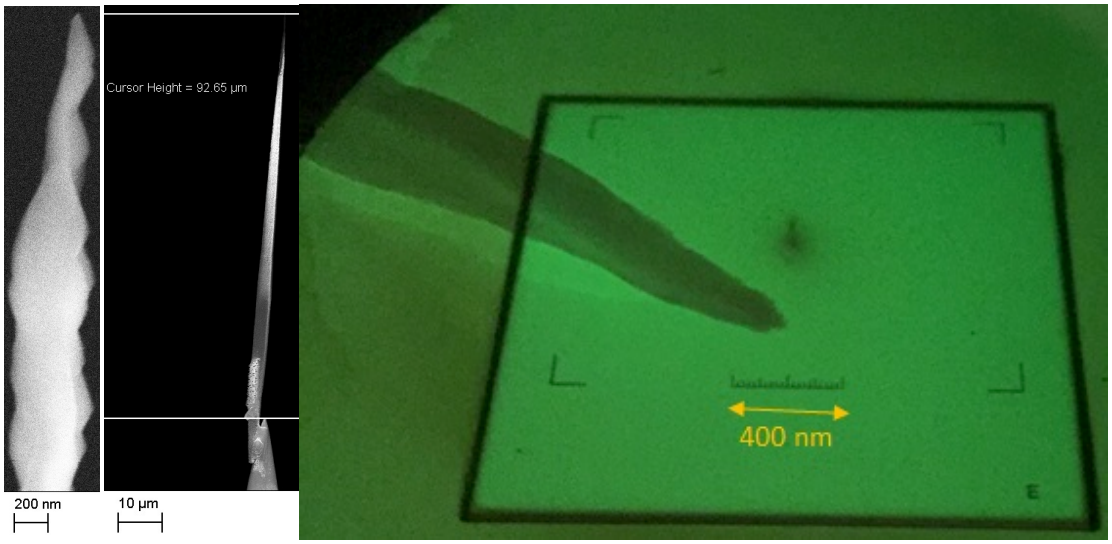

Figure 3.30: (a) Diamond D5, length $\sim 90\,\mu m$, tip apex $\sim 25\,nm$. (b) Diamond C6, length $\sim 14\,\mu m$, tip apex $\sim 25\,nm$

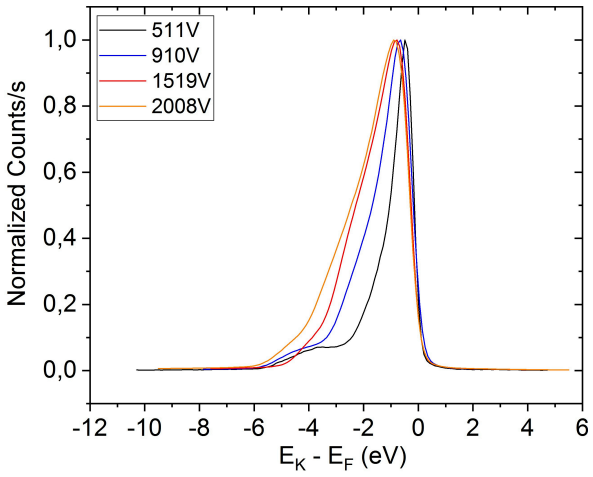

Figure 3.31: Energy spectra of diamond D5 taken at different applied voltages; Aperture 4, CAE 100 eV

Taking into account the non zero temperature at which the spectra where taken ($T = 300\,K$), the fit using Equation 3.22 gives a spectrometer resolution of around $150\,meV$. Integrating the spectra, we can obtain the $I-V$ and $I-\Delta V$ characteristic of the emitter, while with the fits on the spectra, we obtain the value of C_V. Worth to note that since the acceptance angle of the spectrometer is limited and the efficiency of the MCPs of the detector is not 100%, we collect only a part of the total emitted current, which is proportional to the real emission current. In Figure 3.32(a) the $I-\Delta V$ characteristic of the emitter is shown.

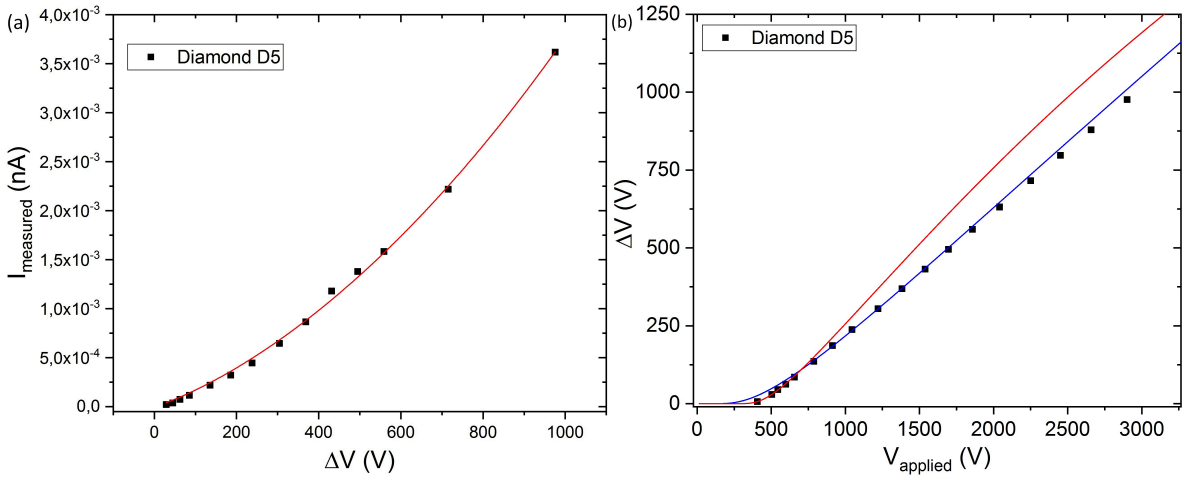

Figure 3.32: (a) $I - \Delta V$ characteristic of the diamond needle D5, taken at ambient temperature and with a variation of $V_{applied}$ between 500 and 3000 V. (b) Measurement of the voltage drop ΔV as a function of the applied voltage $V_{applied}$ and corresponding computed values from Equation 3.25.

As in the previous cases, the $I-\Delta V$ characteristic follows a PF conduction mechanism as shown by the fit of the data. On the other hand, the voltage drop ΔV changes linearly as in the previous case with a slope of 0.397 ± 0.001 and a negative intercept of $(-178\pm3)V$. With the same conduction method as in the case of the measurements on the diamond tip in Toulouse, from the fit of the PF plot and the FN plot (Figure 3.33), we can compute Equation 3.25 in order to obtain the behavior of the voltage drop as a function of the applied voltage.

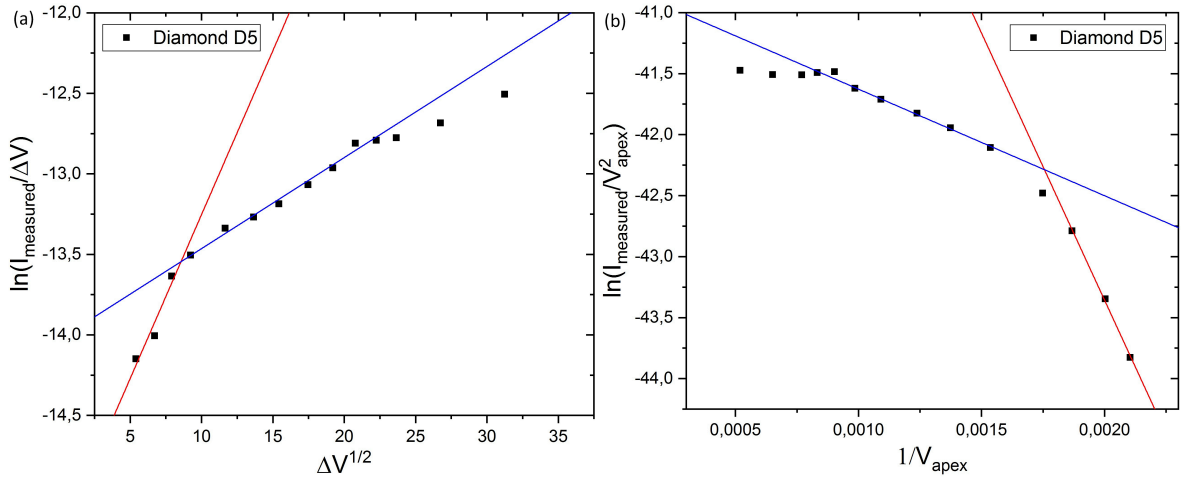

Figure 3.33: (a) $\Delta V - V$ characteristic of the data presented Figure 3.32(a) represented in PF coordinates. (b) The same data plotted in FN coordinates as a function of V_{apex} which is linked to the electric field at the diamond-vacuum junction.

Both the PF and the FN plot of Figure 3.33 show two different linear behaviors before

and after the first four point of measurements, probably due to the effect of current saturation from non conductive materials due to the decrease of electron concentration near the surface and the increase of the electric field penetration in the bulk which changes the geometry of the surface electric field (modification of the enhancement factor β). The PF plot gives, at voltage drops below 10 V, the parameters $A_{D5(lowV)} = (2.32 \pm 0.1) \cdot 10^{-7}\ nA/V$ and $B_{D5(lowV)} = (0.20 \pm 0.06)\ V^{-1/2}$ while at high voltage drop $A_{D5(highV)} = (9.5 \pm 0.1) \cdot 10^{-7}\ nA/V$ and $B_{D5(highV)} = (0.059 \pm 0.003)\ V^{-1/2}$of Equation 3.14. The low voltage part of the FN curve gives a $C_{D5(lowV)} = (9.4 \pm 0.4) \cdot 10^{-7}\ nA/V$ and a $D_{D5(lowV)} = (4370 \pm 170)\ V$ while the high applied voltage part gives a $C_{D5(highV)} = (2.01 \pm 0.08) \cdot 10^{-9}\ nA/V$ and a $D_{D5(highV)} = (873 \pm 26)V$. Taking into account these two regimes in the PF and FN plots, the curve $\Delta V - V$ has been calculated with the 2 different set of parameters using Equation 3.16 giving two different curves as shown in Figure 3.32(b). The curve with the parameters at low applied voltage is in good agreement with the low part of the $\Delta V - V$ characteristic (red line), while the parameters at high applied voltage gives a curve in accordance with the high part of the $\Delta V - V$ (blue line).

If we consider only the low part of the PF curve, where the current is not limited by the FN saturation effect, the fit parameter $B_{D5(lowV)} = \beta_{PF}/k_B T$ can be used in order to find an estimation of $\varepsilon_r d_{PF} \sim 215\ \mu m$. With the use of the bulk dielectric constant $\varepsilon_r = 5.7$, we obtain a $d_{PF} \sim 38\ \mu m$ as the region inside the tip near the apex where the PF effect takes place.

Regarding the FN part, since the FN curve has a change in slope, the two parameter C and D change. From the two fits it is clear that both these parameters decrease with the increase of the applied voltage. The parameter

$$C = aA\frac{\beta^2}{\varphi} \tag{3.23}$$

where A is the emitting surface and $a \sim 1.541 \cdot 10^{-6}\ A\ eV\ V^{-2}$, called the "first Fowler-Nordheim constant", and the parameter $D \propto \upsilon(y)/\beta$ both decrease with the increase of the applied voltage. C implies that the enhancement factor β decreases while D implies that the ration $\upsilon(y)/\beta$ decreases as well. So the approximation of a constant enhancement factor does not apply to this case.

In order to have an estimation of the enhancement factor β, thanks to the Argus spectrometer we can fit the spectra shape using Equation 3.22 in order to obtain C_V. Taking $\varphi = 5eV$ Equation 3.21 can be used in order to estimate the enhancement factor

$$\beta = 22.92 \cdot 10^9 \frac{1}{C_V V_{apex}} \tag{3.24}$$

obtaining the change in the enhancement factor with the increase of the applied voltage (Figure 3.34).

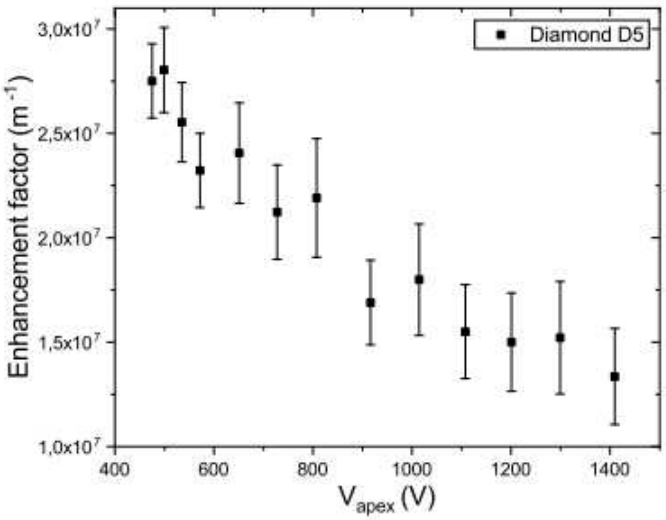

Figure 3.34: Enhancement factor $\beta = E/V_{apex}$ calculated using Equation 3.24

As is clear from the graph, the enhancement factor is not constant but in the case of these types of dielectrics decreases with the increase of applied voltage. The possible explanation is due to the fact that at high applied voltage the strong electric field penetrates more and more into the bulk of the emitter. This penetration changes the distribution of the field deteriorating the lightning rod effect of sharp tips.

3.7.2.3 Study as a function of Temperature

On the diamond D5, besides the study of emission in static regime, a study on the effect of the temperature as been done with the use of liquid nitrogen in the cold finger on the Sphere work bench. In this kind of material, as theoretically predicted and experimentally shown by Kleshch et al., the emission current in the saturation regime of field emission is very sensitive to change of temperature or laser pulses which change the density of carriers inside the samples [26]. In this case, keeping the applied voltage constant, the current has been monitored as a function of the temperature, plotted in "Arrhenius coordinates" $ln(I_{measured})$ as a function of $1/k_BT$ in Figure 3.35.

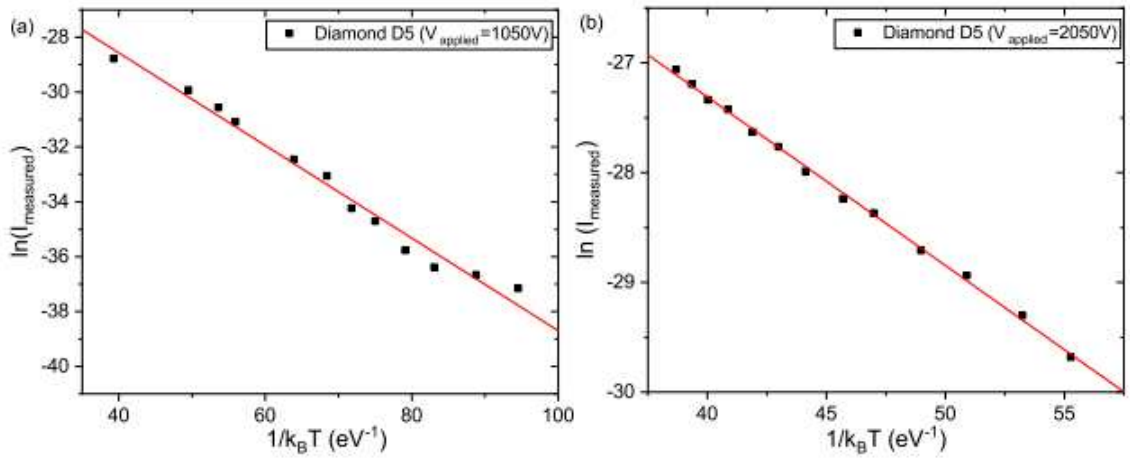

Figure 3.35: Emission current as a function of the temperature in Arrhenius coordinates for diamond D5 at (a) $V_{applied} = 1050\,V$ and (b) $V_{applied} = 2050\,V$.

The linear fits of the Arrhenius plots of Figure 3.35 give a PF $E_a(1050\,V) = (0.17 \pm 0.01)\,eV$and $E_a(2050\,V) = (0.155 \pm 0.005)\,eV$. From the value of the activation energy and the β_{PF}, the trap levels $\phi_{PF} = E_a + \beta_{PF}\sqrt{\Delta V}$ are obtained finding $\phi_{PF}(1050\,V) = (0.18 \pm 0.01)\,eV$ and $\phi_{PF}(2050\,V) = (0.172 \pm 0.005)\,eV$. This trap level is in accordance with the value found in the FIM case of $\phi_{PF} = (0.2 \pm 0.1)\,eV$ and in literature [26].

3.8 Conclusions

In this chapter, we focused on the conduction mechanisms in single crystal CVD diamond nano-needles. As the experimental data show, the internal conduction is not simple. In fact, depending on the geometry characteristic of each sample and the experimental environment (with or without laser illumination, low or high current regimes, FIM or FEM analysis), the conduction is a competition of more mechanisms such as Ohmic conduction, Poole-Frenkel conduction and Fowler-Nordheim emission law. Various models in order to describe the conduction behaviors have been introduced, such as a geometrical model to take into account the conical shape of the samples and the PF-FN conduction model in the case of FEM measurement, describe qualitatively and quantitatively the $I - \Delta V$ and $V - \Delta V$ characteristics of the samples.

Using an high resolution electron energy spectrum analyzer (Argus spectrometer) the enhancement factor has been estimated for CVD diamond and its change as a function of the applied voltage has been measured. FE measurements as a function of the temperature gave additional data for the measure of the trap level inside the diamond needles, confirming the validity of the previous measures.

Chapter 4

Laser assisted field emission from diamond

After the preliminary work on tungsten tips, discussed in Chapter 2, the laser assisted field emission has been studied on the single crystal diamond tips used in our previous analyses.

The main idea in the use of pulsed laser on field emission system is to have a stimulated emission from laser pulses instead of a continuous emission regime in the static case. This pulsed emission of electron could open the possibility of a time-resolved electron microscopy where high stability of emission and brightness are necessary.

As it will be discussed, there are two main types of diamond needle which were analyzed, diamond tips which do not present a voltage drop during field emission and diamond emitters which have a voltage drop during analysis.

At first, diamond tips without voltage drop will be discussed where, after a preliminary characterization in static regime, the results obtained under laser illumination will be shown. In particular the study of the emission pattern and laser polarization dependence at low applied voltage, where static emission is not present, and at high applied voltage in a concurrence of static and laser emission.

Afterwards, diamond tips which present a voltage drop will be considered. For this type of tips, a collaboration with the LCAR of the University of Toulouse has been carried out where I stayed at their laboratories for the duration of one month for a preliminary study of laser illumination on diamond tips. In a second time, with the implementation of a new detecting system as well as the installation of a femto-second fiber laser on the electron emission workbench, a new series of measurements on diamond has taken place. Also thanks to the rent of a 2 micron wavelength fiber laser (Brevity-Lambda+), emission at this laser wavelength has been analyzed.

4.1 Single crystal CVD diamond emitters without voltage drop

As previously said, the objective of this study, is to see if a diamond emitter, material which promises better performances to the respect of metallic emitters, has a more stable emission and brightness compared to the metal case. Even though diamond is a dielectric material with supposedly high electrical resistivity, we observed diamonds tips without voltage drop. Along with the presence of impurities and defects, most likely on the surface, layers of 'non-diamond' carbon could be present, inducing an electrical conductivity comparable to the metal case. Also part of this defective layers on the surface could undergo a modification during emission which make them ordered (graphitic phase) because of Joule heating in high vacuum environment.

The material here discussed is the Diamond HJ already studied in FIM (Chapter 3) reported in Figure 4.1.

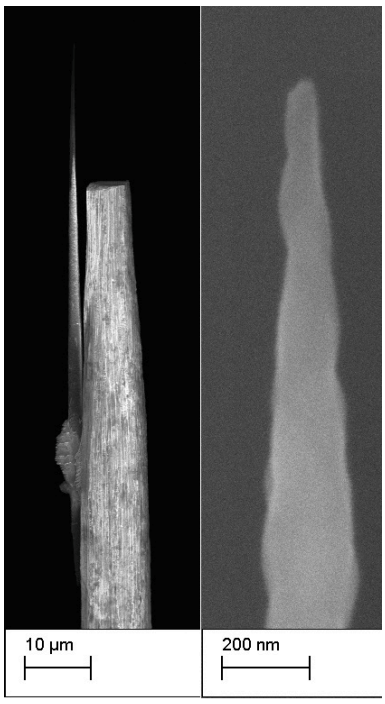

Figure 4.1: Diamond HJ, length $L_{tip} \sim 50\,\mu m$ from the welded point, part outside the shadow of W pre-tip $\sim 22\,\mu m$, tip apex $R \sim 20\,nm$.

In field emission, one of the classical characterization of the sample emission is its FN curve, presented in Figure 4.2. As we can see from the FN plot, this diamond sample presents a FN curve which is linear as in the case of conducting materials, meaning the

emission current obeys the FN law:

$$I = \frac{Aa}{\varphi}\left(\frac{\beta V_{tip}}{R}\right)^2 exp\left(\frac{-b\varphi^{3/2}\upsilon(y)R}{\beta V_{tip}}\right) \tag{4.1}$$

derived for metallic emitter, where V_{tip} is the applied voltage on the tungsten support, R the radius of the emitter, A the emission surface $a = 1.56 \cdot 10^{-6}\, A\, V^{-2}$ and $b = 6.83 \cdot 10^7\, eV^{-3/2}\, V\, m^{-1}$. In the case of a triangular surface potential, the elliptical function $\upsilon(y) = 1$.

In Figure 4.2 the FN curve is plotted in dark regime, that is when no laser illumination is present:

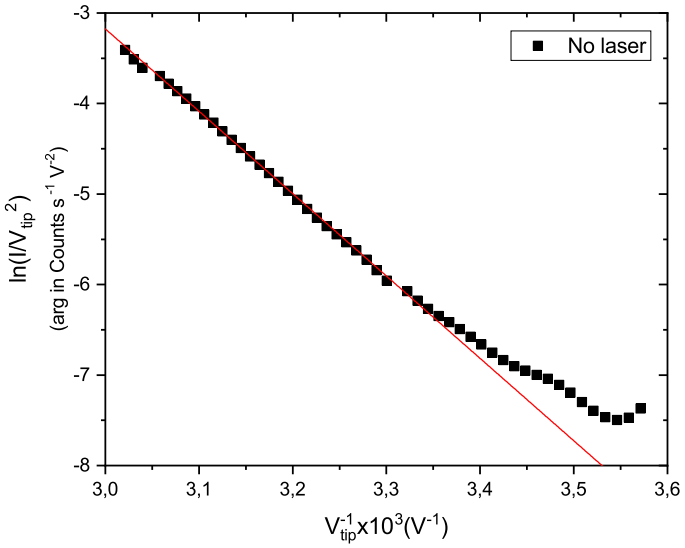

Figure 4.2: Fowler-Nordheim curve of electron emission in dark (no laser illumination)

As is clear from the shape of the curve in Figure4.2, the electron emission follows a metallic behavior being the curve linear. To enhance this statement is the fact that there is no measurable voltage drop during analysis. Another characterization of the tip in static regime is the electron emission spectra and its emission pattern. Furthermore, in the case of multiple emission poles, thanks to our 2D detector system, the emitted current can be integrated in a restrained zone in order to extract the spectrum of each emission pole. Figure 4.3 shows the emission spectra obtained for the 2 emission poles that appear in static regime. Being the emission areas relative to the two emission poles different, only the shape of the spectra can be compared and not their amplitude. These spectra show a single peak on the Fermi level where in this case $E_{Fermi} = e \cdot V_{tip}$, indicating no voltage drop.

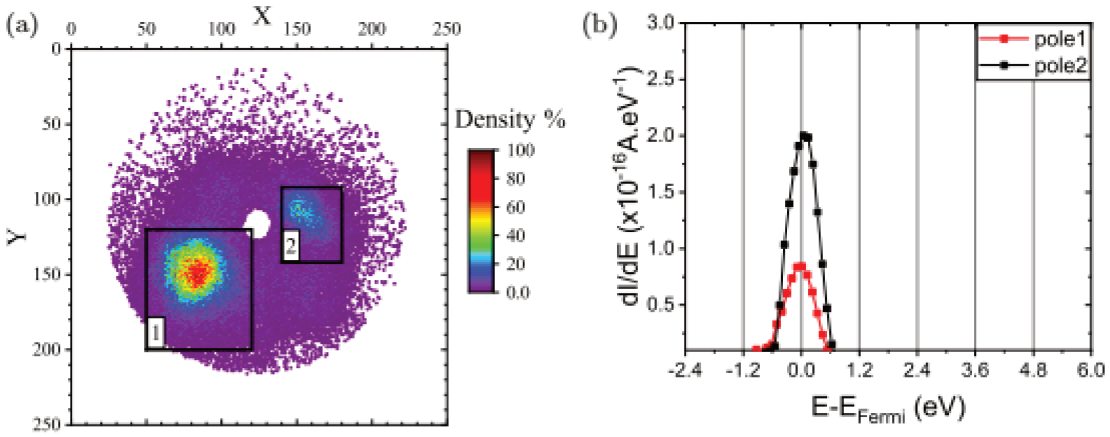

Figure 4.3: (a) Field emission pattern in the dark at $V_{tip} = 300 V$. The (X; Y) coordinates indicate the position on the CCD camera in number of pixels. The colors map corresponds to the normalized density of impacts. (b) Electron energy spectra at $V_{tip} = 300\,V$ of the poles 1 (black dots) and 2 (red dots) defined in (a).

With the application of laser pulses on the surface of the diamond sample, photon with $1.2\,eV$ energy have been focused on the diamond sample with a focal width of about $45 \pm 5\,\mu m$. Laser illumination has a strong effect on the electron emission, leading to a strong increase of the emission current as well as the lowering of the voltage threshold required for electron emission, where with sufficient laser power can be decreased to the tens of volts. As an example, with the application of around $27\,GW/cm^2$, at an applied voltage of $300\,V$, the emission current rises of a factor of 50 (Figure 4.4).

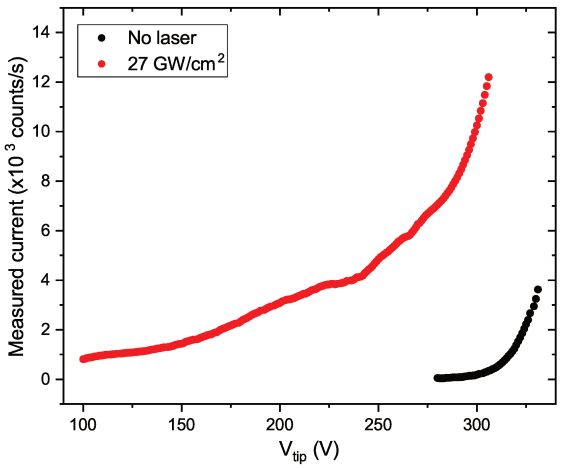

Figure 4.4: I-V characteristic of electron emission obtained in dark (black dots) and under laser illumination at $37.5\,kHz$ (red dots).

Another fact worth of note is that with laser illumination the emission results being more stable in time (Figure 4.5). For example, the emission current of Figure 4.5 at

around 10^4 $Counts/s$ has 6% of standard deviation in the laser illumination case while has 13% standard deviation for the emission without laser illumination.

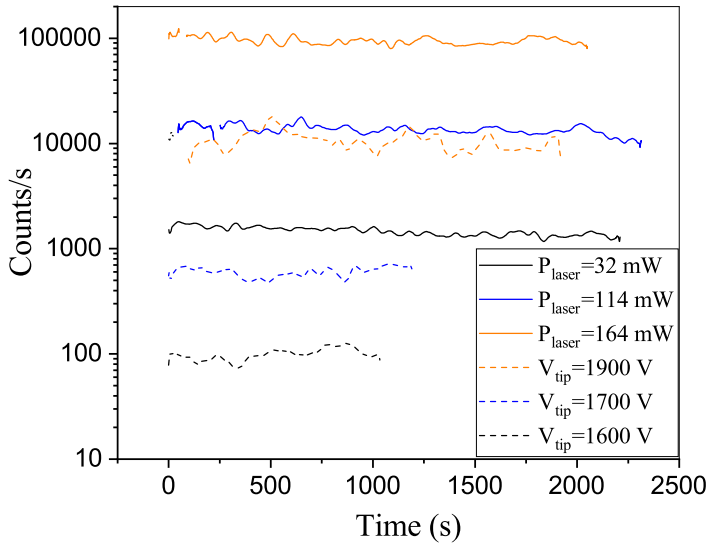

Figure 4.5: Emission currents as a function of time, full line correspond to laser assisted emission while dashed lines are emission currents in dark.

As in the case of metallic emitters, with the application of laser illumination, the assisted emission by photons depends strongly on the laser polarization angle with the sample axis. This dependence is due to the fact that photo-field emission depends only on the component of the laser electric field normal to the emitting surface [36]. This means that at the apex of the tip surface the maximum effect of the laser on the electron emission is when the laser polarization is parallel to the axis of the tip. This effect is visible in the emission current plot as a function of the laser polarization of Figure 4.6. The dependence on polarization orientation exhibits a $cos^{2n}(\theta)$ behavior with $n = 5$, where θ is the angle between the tip shank and the polarization axis of the laser beam. This suggests a multi-photon emission regime thanks to the enhancement of the laser field component along the needle axis. This cosine curve also excludes any possibility of thermally induced field emission, which has been shown elsewhere to be most efficient when the laser polarization is perpendicular to the tip axis [61].

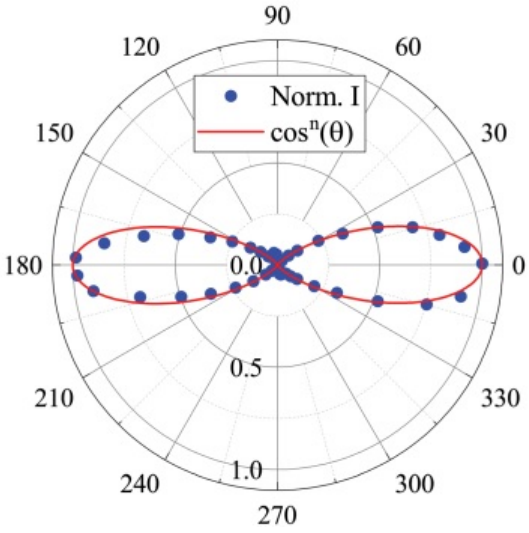

Figure 4.6: Normalized emission current as a function of the laser polarization angle θ. $V_{tip} = 100\,V$ with a laser illumination of $10\,GW/cm^2$ and a repetition rate of $2.35\,kHz$. Laser polarization parallel to the tip axis corresponds to $\theta = 0°; 180°$ while polarization perpendicular to the axis corresponds to angle of 90° and 270°. The line is the data fit with a $\cos^n(\theta)$ law with $n = 10$.

4.1.1 $I - V$ characteristic under laser illumination

With the use of laser illumination, the modification of the emission can be characterized in the $I - V$ curves plotted in the FN coordinates as well as by monitoring the changes on the electron energy spectra and emission pattern. The measurements shown here are in the case of the laser focused on the tip with the use of a lens mounted externally of the vacuum chamber, with the result of a focused laser beam waist of about $40\,\mu m$ which illuminates all the diamond needle (in Figure 4.1, $L \sim 22\,\mu m$).

In the case of FN plots, the graphs show a linear behavior at high applied voltage while at lower voltages the FN characteristic results constant (Figure 4.8). This implies that the emission regime is still following the FN process at high applied voltages, where the emission is assisted by the laser (photo-assisted field emission), while for low applied voltages the laser is strong enough to promote carriers to a level of energy higher than the vacuum barrier consenting electron to escape into vacuum (multi-photon field emission). This laser assisted emission regimes are shown in Figure 4.7.

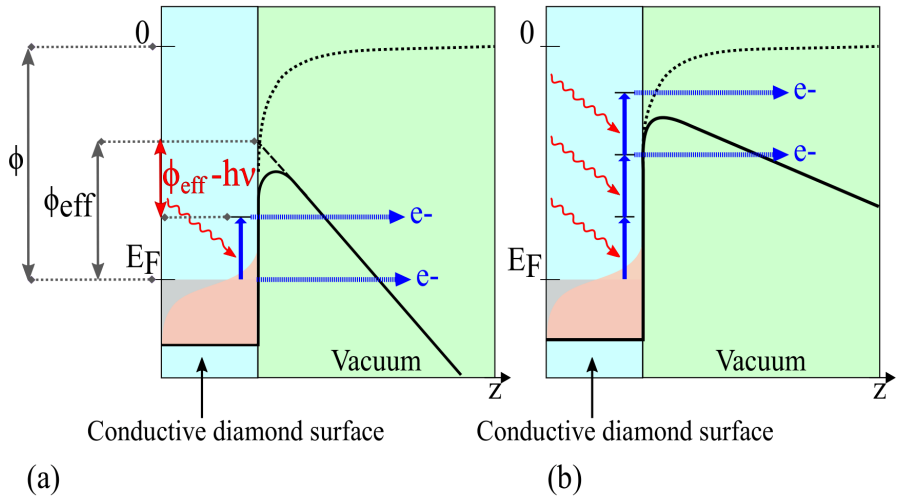

Figure 4.7: Laser assisted electron emission processes: (a) photo-assisted field emission; (b) multi-photon field emission.

During field emission, with the application of a bias voltage on the emitter, the image potential on the emitter-vacuum interface decreases the work function φ of the emitter to an effective work function (effective barrier height):

$$\varphi_{eff} = \varphi - \sqrt{\frac{e^3 \beta V}{4\pi\varepsilon_0 R}} \tag{4.2}$$

being βV the field on the apex of the tip. As shown from Figure 4.8, at high applied voltages ($1/V_{tip} < 0.0035\ V^{-1}$), the slope of the FN plot decreases with the increase of the laser intensity. This slope, as reported in Equation 4.1, is proportional to $\varphi^{3/2}/\beta$. In the case of laser illumination, the increase of laser intensity increases the probability of absorption of photons, which can increase the initial energy of the electrons before tunneling into vacuum. This increase of initial energy has the effect to directly change the FN emission by changing the effective work function of the emitter. Below the FN curves of Figure 4.8, three emission pattern are reported. These emission pattern are obtained during the FN analysis corresponding to the emitted electrons through the entire range of applied voltage used in order to obtain the relative FN curve. As shown, in dark regime (Figure 4.8a) the emission pattern is the same as in the case of the pattern relative to the static emission spectra of Figure 4.3. Applying laser to the FN measurements, the emission pattern changes. At low laser intensity ($13\ GW/cm^2$ of Figure 4.8b), the static emission is enhanced by the laser, while increasing the laser power ($26\ GW/cm^2$of Figure 4.8c) the emission is more intense with a larger emission zone with the appearance of an emission zone on the right part of the detector.

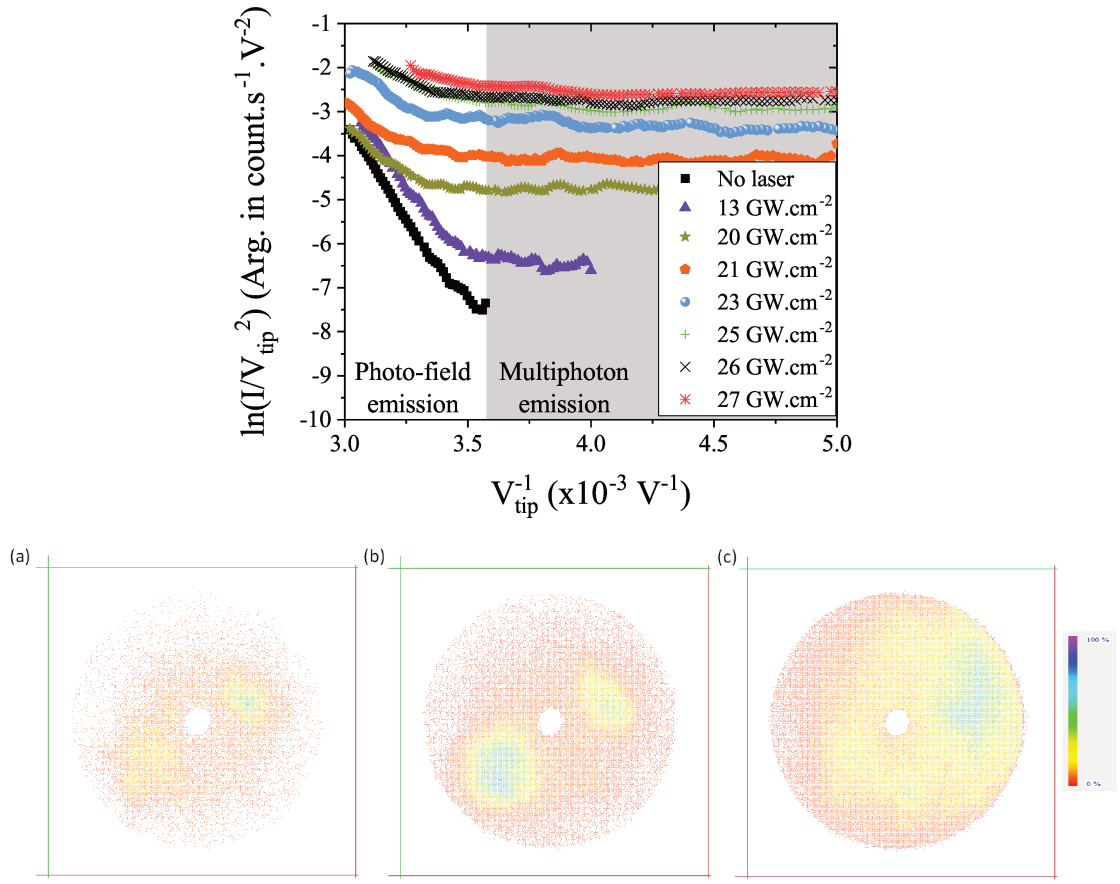

Figure 4.8: FN plots from diamond for different laser peak intensity at a repetition rate of 37.5 kHz. At high applied voltages (left side of the dashed line) the $I-V$ characteristic is linear in FN coordinates corresponding to photo-field emission while at low applied voltages (right side of the dashed line) the $I-V$ characteristic is constant in FN coordinates denoting multi-photon above barrier emission regime. Emission patterns during FN measurements taken in (a) dark regime(no laser illumination), (b) at 13 GW/cm^2 and (c) at 26 GW/cm^2.

At high applied voltage ($V_{tip} \geq 300\ V$), in the case of photo-field emission, through the ratio between the slope of the FN curves with laser illumination with the one in the absence of laser illumination, it is possible to have an estimation of the effective work function as well as the number of photon absorbed for each laser intensity (Figure 4.9a). In fact, the slope of the FN curve D is related with the ratio of the emitter work function φ and the enhancement factor β:

$$D \propto \frac{\varphi^{3/2}}{\beta} \tag{4.3}$$

Since the emitter do not present an energy deficit, in this case the enhancement factor is considered as constant and so the change of the FN slope is only related to a modification of the effective work function. Using Equation 4.3, from the ratio between the FN curves corresponding to laser illumination and the slope in dark emission, the value of the effective

work function with the absorption of one or more photons can be obtained, knowing the laser photon energy is $1.2\,eV$ (dashed lines in Figure 4.9a). The plot shows that with the increase of laser illumination, the emission process is assisted by laser with the absorption of 1 to 3 photons with the effect of effective reduced work function of more than 60%.

On the other hand, at low applied voltage ($100\,V$ and $180\,V$), plotting the emission current as a function of the laser intensity in log-log scale should give a linear behavior where the slope of the linear fit gives an indication of the mean number of photons that are absorbed in the process (Figure 4.9b). The slope in log-log scale give a value of 4.0 ± 0.6 for the $100\,V$ case and of 3.9 ± 0.6 for $180\,V$. This value of the slope of 4 suggest that at least there is a four photon absorption process in the multi-photon emission regime.

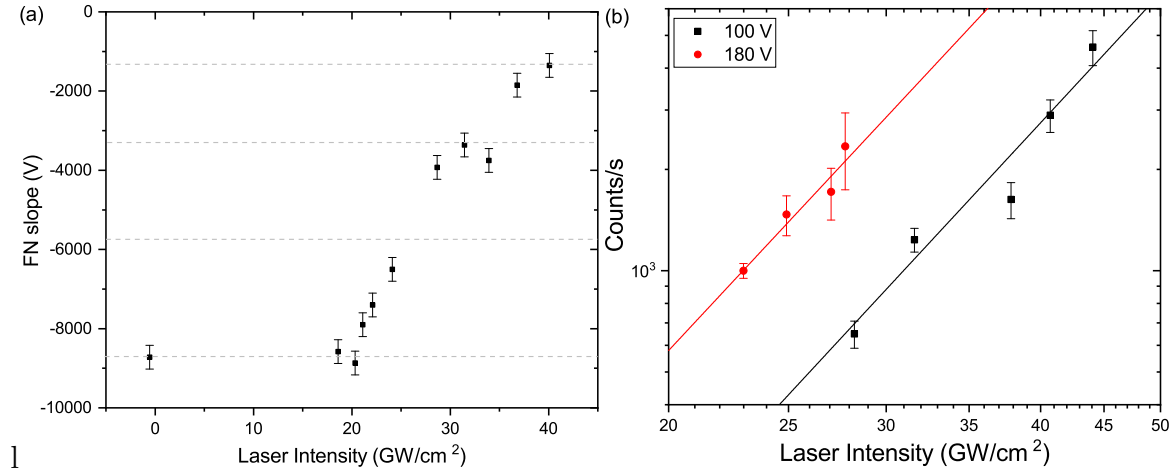

Figure 4.9: (a) Slope of the FN plots as a function of the laser peak intensity (I_{peak}) with $V_{tip} \in [280; 350]\,V$. The dashed lines correspond to the slopes of the FN plots calculated from the reduction of the height by absorption of one, two or three photons. (b) Emission currents as a function of the peak laser intensity in log-log scale.

4.1.2 Electron energy spectroscopy at low laser repetition rate

With the use of the spherical retarding lens of the LEED spectrometer, the electron energy spectra have been measured in static and under laser illumination. The parameters that can be adjusted for this type of measure are the applied voltage V_{tip}, the laser peak intensity I_{laser}, the laser pulse repetition rate ν_{laser} as well as the laser polarization θ_{laser}. In the case of electron spectra measurements, since the laser polarization influences only the emission current without affecting the emission pattern, the laser polarization angle has been aligned on the angle where maximum emission occurs (around $\theta = 0°$, $180°$ of Figure 4.6). In order to monitor the two emission regimes that appear in the $I - V$ curves of Figure 4.8, in the case of photo-field emission (high applied voltage) various spectra have been obtained at an applied voltage $V_{tip} = 300\,V$.

The first series of measurements with laser illumination have been carried out using the laser in a low repetition rate mode (below or equal to $100\,kHz$). This choice is justified by the fact that at high laser repetition rates a pile-up of thermal effects induced by the laser has been reported on Ag emitter as well as carbon nano-tubes (CNTs) [62, 63]. This pile-up effect is regarded as a change in regime which takes place at high repetition rates where the multi-photon emission switches to thermal emission.

The emission spectra, reported in Figure 4.10, have been acquired using a scan step of $0.1\,V$ and smoothed in post-treatment with a Savitzky–Golay smoothing filter over 20 adjacent points. In these spectra, two main peaks appear. The peak at $0\,eV$ corresponds to the electrons emitted from the Fermi level while the second wider peak is a convolution of multiple emission peaks which correspond to electron emitted with the assistance of the absorption of 1, 2 or 3 photons. Raising the laser intensity, the second peak increases in amplitude and shifts to higher energies indicating that the photo-assisted emission becomes predominant over the static emission.

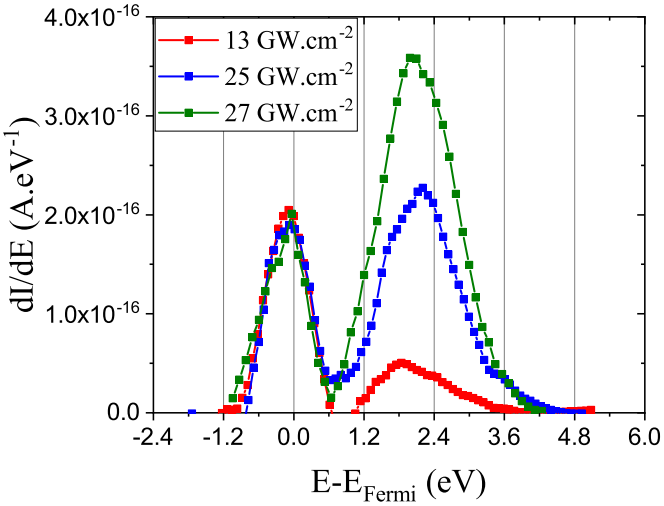

Figure 4.10: Electron energy spectra at $V_{tip} = 300\,V$ with different laser peak intensities taken at $37.5\,kHz$ repetition rate.

4.1.2.1 2D electron spectroscopy

The emission pattern associated to the energy spectra of Figure 4.10 are shown in Figure 4.11. When the sample is illuminated at low laser peak intensity (Figure 4.11b), the emission pattern present few changes compared to that observed in the dark (Figure 4.11a). Static emission poles 1 and 2 are always visible but they are broader. One can also distinguish the appearance of a third area (pole 3). At higher values of laser peak intensities (Figure 4.11c and Figure 4.11d), the right side of the map (shadow side) is

intensified to the detriment of static poles 1 and 2 on the left side (illuminated side of the tip).

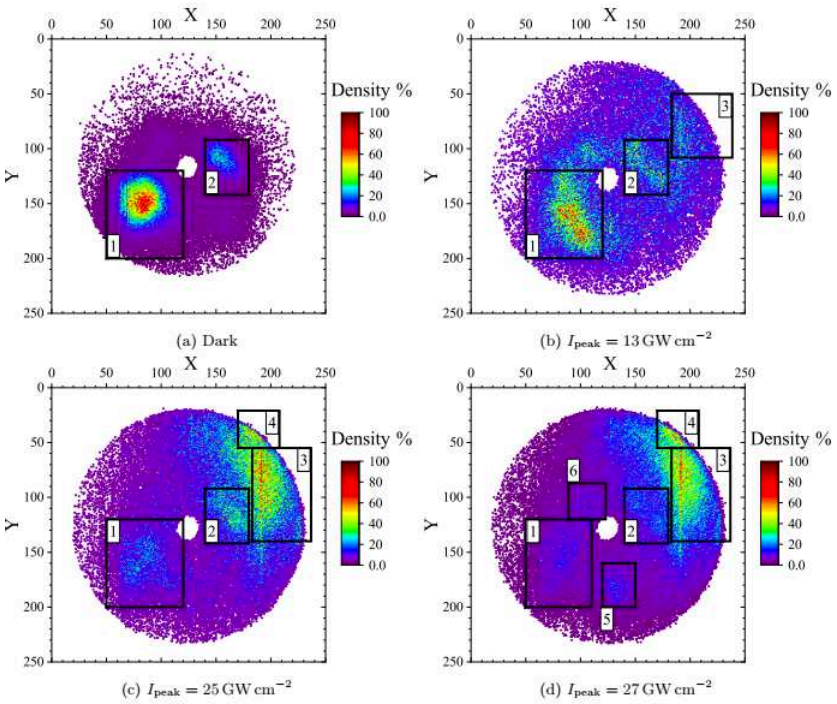

Figure 4.11: Emission pattern at $V_{tip} = 300V$: (a) in the dark; and under laser illumination at $37.5\,kHz$ (b)$I_{peak} = 13\,GW/cm^2$ (c) $I_{peak} = 25\,GW/cm^2$ (d) $I_{peak} = 27\,GW/cm^2$. The (X ; Y) coordinates indicate the position on the CCD camera in number of pixels. The colors map corresponds to the normalized density of impacts.

Thanks to the acquisition of emitted electrons in 2D maps, the emitted current can be integrated in a restrained zone in order to extract the spectrum of each emission pole. The area selected on the detector system are indicated by rectangles on the emission pattern figures. Because the size of the areas are different, only the shape of the spectra can be compared and not their amplitude.

When the sample is illuminated by the laser at $I_{peak} = 13\,GW/cm^2$, the field emission pattern changes, as reported in Figure 4.12a. The two poles move from round to elongated shape, as if they were part of the same ring patter. Moreover, a new emission area appears on the right-high part of the detector indicated in Figure 4.12a by the region 3. The impacts collected on the right part of the detector corresponds to electron emitted from the shadow side of the diamond needle compared to the incoming laser beam. The spectra corresponding to the area delimited in Figure 4.12a, are shown in Figure 4.12b, and compared to the total spectra integrated on the whole surface of the detector. Two peaks are visible, the first at the Fermi energy, as already reported for static emission (Figure 4.3) and the second peak at an energy $E = E_F + 2.2\,eV$, which corresponds to photo-assisted

field-emission, by the absorption of 1, 2 or 3 photons. This peak is wider because of the convolution of the different emission peaks related to photon absorption [63]. For poles 1 and 2, the static emission is stronger than the photo-assisted field emission, however for pole 3 the two emission processes have the same amplitude. Therefore, on the region 3, the laser contribution seams to be stronger that on the area 1 and 2.

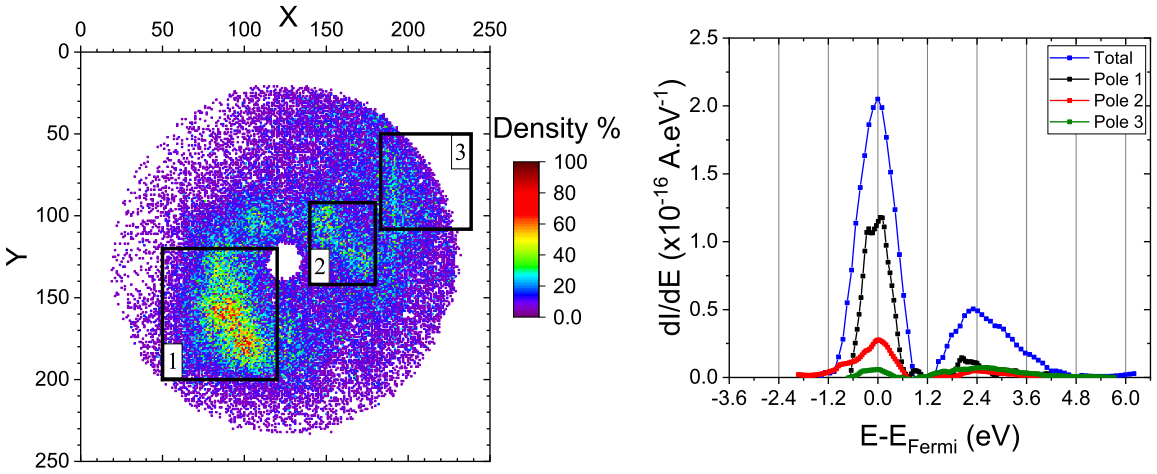

Figure 4.12: (left) Field emission pattern and (right) normalized energy spectra of the poles 1 (black dots), 2 (red dots), 3 (green dots) defined in (left), at $V_{tip} = 300\,V$ under laser illumination with 37.5 kHz repetition rate and $I_{peak} = 13\,GW/cm^2$.

At higher laser intensity, $I_{peak} = 25\,GW/cm^2$, the field emission pattern continues to evolve, as reported in Figure 4.13a. The poles 1 and 2 are still visible even if their intensity has strongly decreased. The emission region 3 is now larger and the emitted current is higher. The spectra corresponding to the three area, are shown in Figure 4.13b-c, and compared to the total spectra integrated on the whole surface of the detector. For poles 1 and 2, two peaks are visible, as already reported for emission al lower laser intensity. The first peak at the Fermi energy is followed by a the second peak at the energy $E = E_F + 3\,eV$, which corresponds to photo-assisted field emission. Increasing the laser intensity from 13 to 25 GW/cm^2, the second peak shifts toward higher energies and its amplitude increases, indicating that photo-assisted field emission becomes more favorable, and the number of photons involved in the process increases [63]. Moreover, at $I_{peak} = 25\,GW/cm^2$, the static emission is still stronger than the photo-assisted field emission.

In the region 3, the first peak disappears. On the right scale of Figure 4.13c, the variation of the current of region 3 on the detector is reported. For $E < E_F + 1.2\,eV$, the current fluctuates and the spectra can be calculated only for energy higher than 1.3 eV. Therefore, the laser contribution seams to completely mask the static field emission on the region 3.

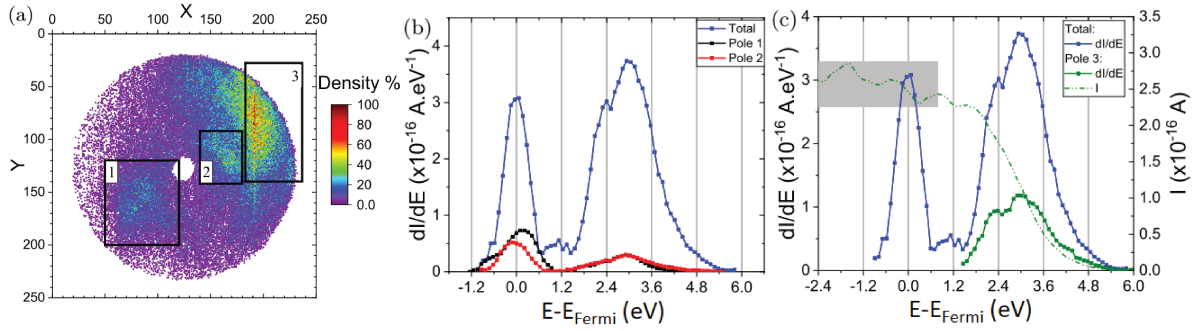

Figure 4.13: (a) Field emission image, (b) normalized energy spectra of the poles 1 (black dots), 2 (red dots) and c) normalized energy spectra and emitted current from the region 3 defined in (a), at $V_{tip} = 300\,V$ under laser illumination with with $37.5\,kHz$ repetition rate and $I_{peak} = 25\,GW/cm^2$.

Under laser illumination, two different emission behaviors have been reported, depending on the laser intensity. At low laser intensity, the laser beam enhances the emission from the areas where the emission takes place in dark (poles 1 and 2). Moreover, the energy spectra show that photo-field emission is added to static emission. At high laser intensity, the laser beam allows the emission from a different area, compared to the emission in dark. This area, named the region 3, is on the right side of the detector, therefore it corresponds to an emission area which is located in the opposite side of where the laser illumination is coming from. Moreover, the region 3 is large and covers almost all the right part of the detector. The related energy spectrum shows that the emission is pure photo-field emission. A similar behavior was reported by M. Marchand et al. on carbon nano-tubes [64]. It was shown that the pattern of the static emission can switch from a single point to a ring with the increase of the field emitter temperature. Moreover, the width of the ring depends on the temperature, it is larger at lower temperature. In the present work, only a part of the ring is visible in the region 3, probably because the temperature is not the same on the illuminated and shadowed side of the field emitter. In order to prove this assumption, the laser-tip interaction was computed by finite-difference time domain (FDTD) with a commercial software from Lumerical. In this model, the tip is represented as a cone terminated by a hemispheric cap. It is placed in the simulated space and surrounded by perfectly matched layer avoiding any field reflection. For the wavelengths of $1030\,nm$, the material properties are taken into account by using the refractive index $n = 2.4 + i0.003$. The electric field and the divergence of the Poynting vector (which corresponds to the absorbed energy) are calculated in all the simulated space. The results obtained on the small volume of $350 \times 350 \times 350\,nm^3$ close to the apex, are reported in Figure 4.14. The electric field and the absorption map are perfectly symmetric with respect to the axis of the needle. Therefore, if the laser-induced emission area is at the apex of the sample, these results can not explain why the emitted electrons

impact only the right side of the detector system.

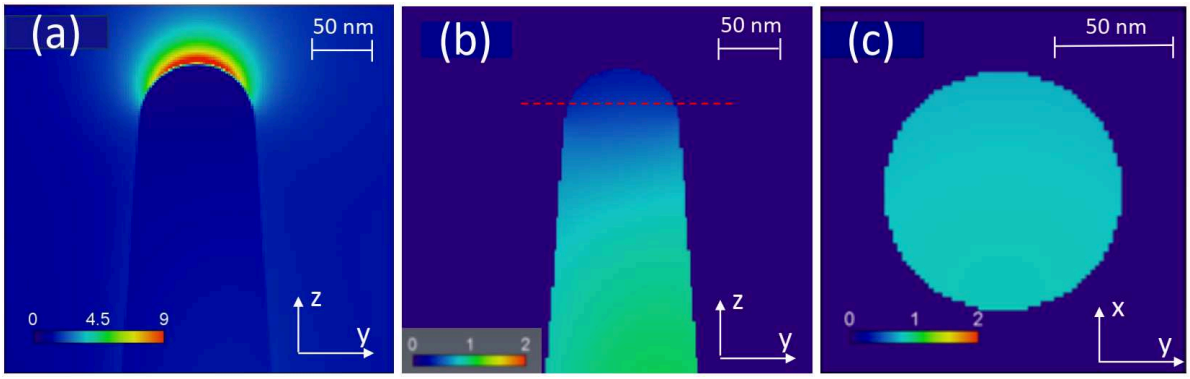

Figure 4.14: (a) (x,z) cross section of the electric field distribution for an incident field of amplitude 1 V/m. The color scale is in V/m. (b) (x,z) and (c) (x,y) cross section of the absorbed energy for an incident field of amplitude $1 V/m$. The color scale is in W/m^3. The red dashed line indicates the plane of the (x,y) cross section. The propagation direction of the laser is along the y axis and it is coming from the left.

However, the numerical results obtained on a large volume show an inhomogeneous distribution of the electric field and the absorbed energy (Figure 4.15). On the absorption cross section of Figure 4.15a, a few regions of higher absorption are visible on the shadowed side. These regions correspond also to the area where the electric field is higher (Figure 4.15b). The inhomogeneous enhancement of the electric field and the presence of high absorption area have been already reported on metallic and non-metallic field-emitters and they have been associated to the diffraction of the light by the nano-metric needle [65, 66]. The areas where the absorption is higher correspond to the areas where the temperature of the sample is higher and the electric field is enhanced. Therefore, these are are good candidates as source of the electrons but, in the case of emission from a flat surface on the shank of the needle, the electrons can't impact the detector, due to the limited angle of the view of the energy analyzer.

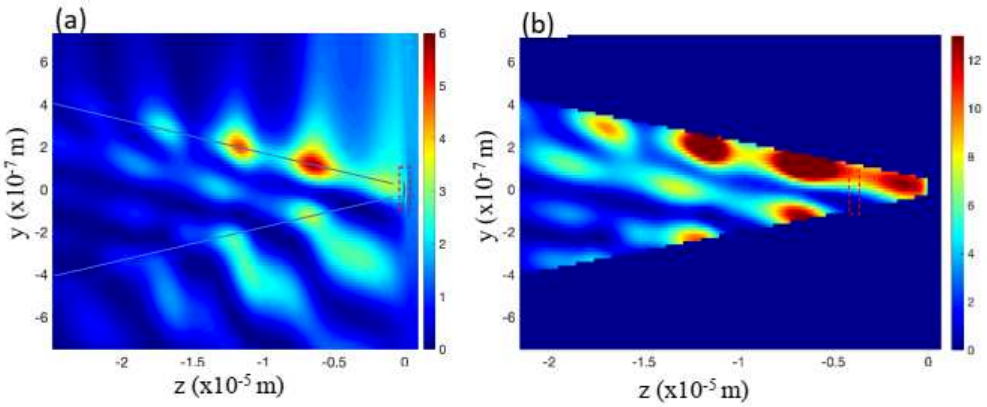

Figure 4.15: (a) (x,z) cross section of the absorbed energy for an incident field of amplitude $1\,V/m$. The color scale is in W/m^3. The dashed box in black corresponds to the volume simulated in Figure 4.14. (b) (x,z) cross section of the electric field distribution for an incident field of amplitude $1\,V/m$. The color scale is inV/m. The box in red correspond to the volume simulated in Figure 4.14. The laser is propagating along the y axis from the bottom to the top.

In the case of diamond needles, many asperities are visible at the surface, as shown in Figure 4.16. These asperities can emit electrons. The trajectory of the electrons emitted by asperities on the larger area on the shank where the absorption is higher have been calculated numerically using the software *Lorenz2D*, taking into account the symmetry of revolution along the nano-needle axis.

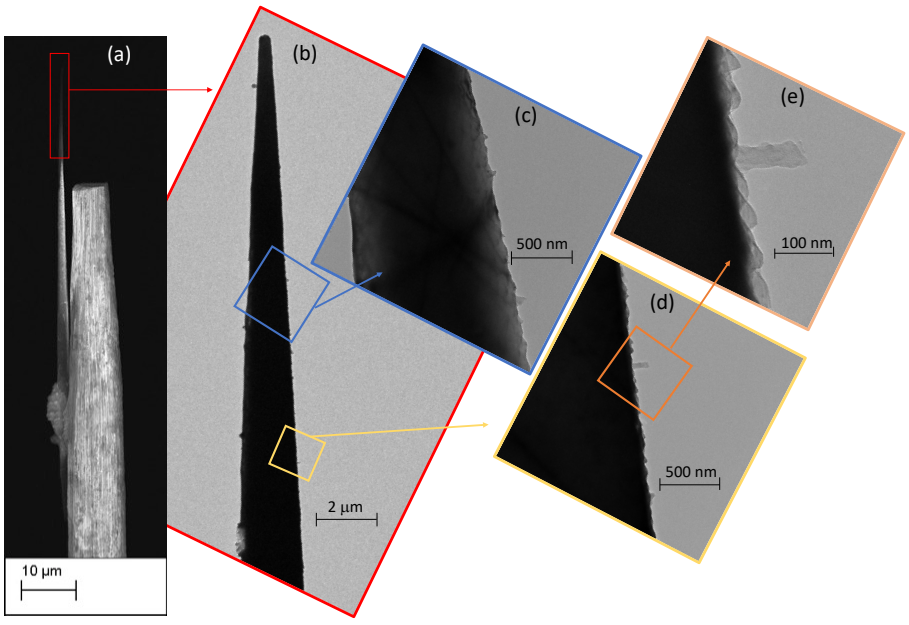

Figure 4.16: Transmission electron microscopy images, the zoom on the side of the sample shows nano-sized asperities on the side of the diamond.

The trajectory of the electrons emitted by asperities on the larger area on the shank

where the absorption is higher have been calculated numerically using the software Lorenz2D, taking into account the symmetry of revolution along the nano-needle axis. As shown on Figure 4.17, three asperities of about $150nm$ in height have been placed at 6, 12 and $18\mu m$ from the needle apex, corresponding to the maximum absorption and field-enhancement areas. These asperities are considered as electron emitters, together with the apex of the sample. The trajectories from the asperity close to the W support overlaps with the other trajectories (Figure 4.17b) and reach the detector system on the upper border (Figure 4.17c). The folding of the trajectories is influenced by the presence of the tungsten support. As shown in Figure 4.16a, the diamond tip is fixed on a tungsten support which terminates with a flat surface of about $10\,\mu m$ in thickness. This charged surface is at the origin of the trajectories folding. The support structure strongly influences the trajectories of electrons emitted by the asperities. A thicker tungsten support can induce a folding of trajectories from asperities far from the diamond/tungsten junction while a thinner tungsten support can avoid this folding phenomena. In the case of the sample of Figure 4.16, only the electrons emitted from asperities close to the diamond/tungsten junction will be detected on the border of the detector system. The static electric field in this area is 50 times lower than the field at the apex of the sample. However, the enhancement of the optical field on the asperities can compensate this lack in static electric field.

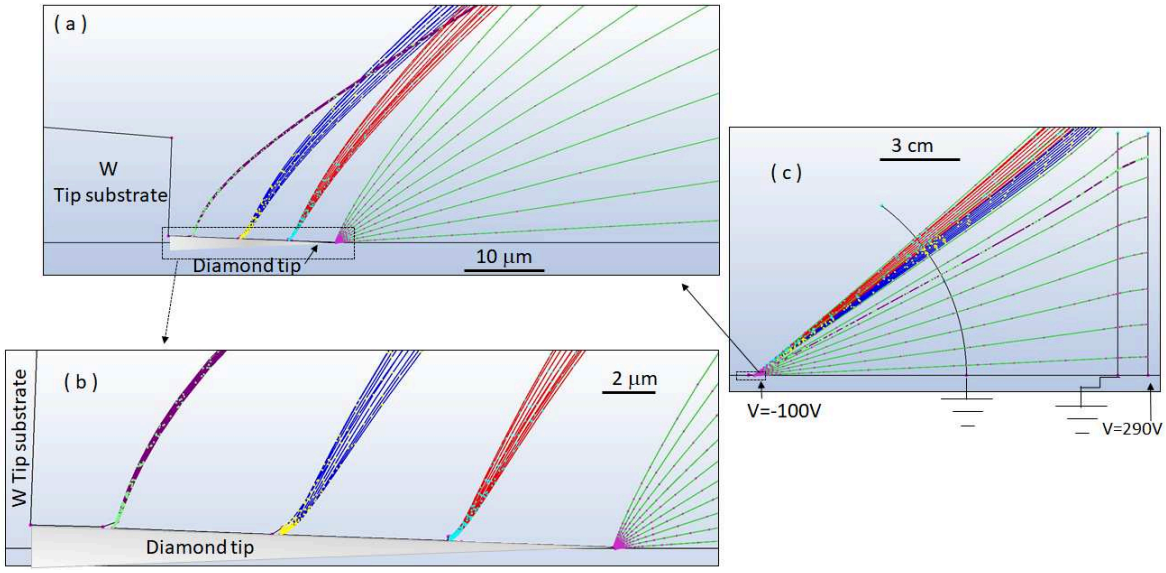

Figure 4.17: Simulation of the electrons from the diamond needle to the anode screen on different spatial scales : (a) $10\,\mu m$; (b) $1\,\mu m$ and (c) $1\,cm$. The trajectories of electrons emitted from the apex are represented in green, from the first, second and third asperity from the apex in red, blue and violet, respectively. The electrostatic configuration of the experimental analysis chamber is reported in (c).

4.1.2.2 Emission spectra at low applied voltage

In order to study the other emission regime observed in the FN curves of Figure 4.8, energy spectra have been acquired decreasing the applied voltage to $100\,V$. In this case the emission at $0\,eV$ is not present since there is no static emission from the E_F. When V_{tip} is decreased down to the static emission threshold while the sample is still illuminated, the emission is only due to the laser by multi-photon emission. In this condition, only the emission region 3 of Figures 4.12 and 4.13 is visible on the detector, as shown in Figure 4.18.

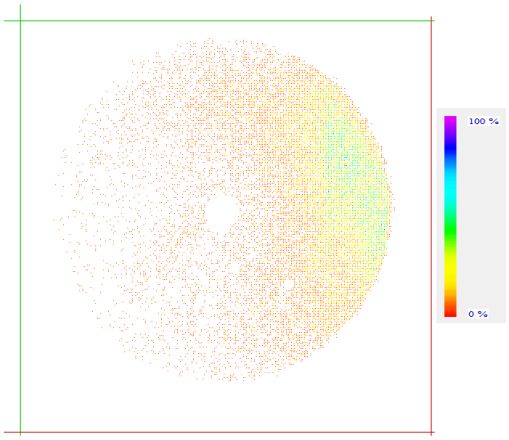

Figure 4.18: Emission pattern at $V_{tip} = 100\,V$ under laser illumination at $100\,kHz$ at a laser peak intensity of $15\,GW/cm^2$. The associated emission spectrum is shown in Figure 4.19.

The spectra obtained in these conditions for different values of the laser peak intensities ranging from $11\,GW/cm^2$ to $18\,GW/cm^2$ at $100\,kHz$ repetition rate are shown in Figure 4.19.

However, at a relative kinetic energy ranging from $2.4\,eV$ to $4.8\,eV$ two peaks are visible from the spectra at low laser intensity. These two peaks are separated by the $1.2\,eV$, the photon energy, as expected in the case of multi-photon emission and are the peaks corresponding to the absorption of 3 and 4 photons. At higher laser intensity, the multi-photon emission of 5 and 6 photons becomes visible, as shown in the log scale graph of Figure 4.19(right).

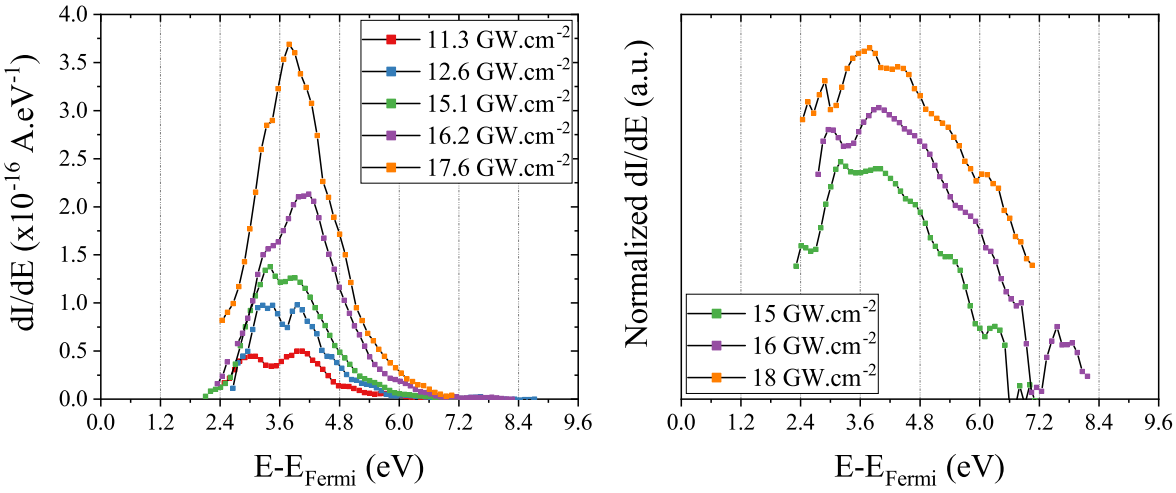

Figure 4.19: Electron energy spectra for different laser intensity taken at 100 kHz repetition rate at $V_{tip} = 300\,V$, on the left in linear scale and on the right in a semi-log scale.

In order to confirm the multi-photon emission, an energy selective measurement of the peaks has been done (Figure 4.20). Each line corresponds to one peak of emission as defined in Figure 4.19, where the electron yield is obtained by the integration of the peaks over the energy corresponding to each peak (for example the first peak correspond to the interval of energies between 2.4 and 3.6 eV).

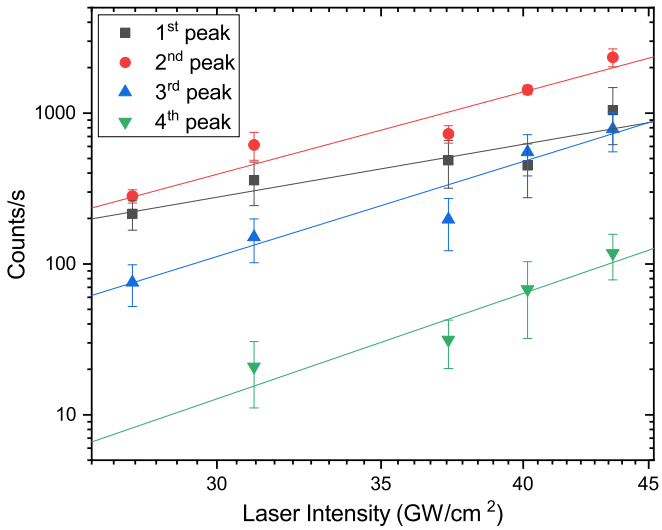

Figure 4.20: Log-log graph of electron yield as a function of laser peak intensity plotted for each emission peak of the energy spectra of Figure 4.19. The dots are the experimental data and the lines are the linear fit for the extracted exponent.

The linear fit give a factor of 2.8 ± 0.6 for the first peak, 4.4 ± 0.6 for the second, 5.1 ± 0.7 for the third and 5.6 ± 1.5 for the fourth. The first exponent is close to 3

indicating a 3 photons absorption process. This means that the effective work function in this case is around 3.6 eV (three times the photon energy). Being the applied voltage of $V_{tip} = 100\,V$, the estimation of the effective work function is not precise since some electrons can still tunnel into vacuum through the potential barrier.

The last peak has an higher error due to the fact that it can only be isolated from the background noise at high laser intensities and shows that when the laser intensity is high enough, the system absorbs up to 6 photons in order to emit electrons into vacuum. The range of intensities explored is relatively narrow due to the fact that the emission is very sensitive to laser, making the detector saturate quickly in emission current restricting the laser intensity range that can be probed with our experimental setup. Due to this narrow range of current, the limited range of laser intensity used could affect even more the error given by the fits of Figure 4.20.

Taking into account Equation 4.2, it follows that there should be an energy shift in the spectrum when the applied voltage is changed. In particular, from Figure 4.21, it appears that for the spectrum at lower applied voltage the energy peaks are at higher energies. This behavior has been described by H. Yanagisawa et al. on tungsten field emitters [67, 68]. In fact, also confirmed by numerical simulation, this behavior can be explained by the increase of the effective work function of Equation 4.2 that increases with the decrease of the electric field present on the apex surface of the emitter. As shown in Figure 4.21, the maximum of the first emission peak shifts from 4.1 eV at $V_{applied} = 100\,V$ to 4.7 eV at $V_{applied} = 30\,V$ giving a $\Delta E = 0.6 \pm 0.1\,eV$. Using Equation 4.2 we can extract the ratio β/R with the use of:

$$\Delta E = \sqrt{\frac{e^3\beta}{4\pi\varepsilon_0 R}}\left(\sqrt{V_1} - \sqrt{V_2}\right) \tag{4.4}$$

where $V_1 = 30\,V$ and $V_2 = 100\,V$. For a $\Delta E = 0.6\,eV$ we obtain a ration $\beta/R = (1.2 \pm 0.4) \cdot 10^7\,m^{-1}$. Note that in this case, the enhancement factor β differs from the enhancement factor of Chapter 3 by the factor R which in this case is not included directly inside β. The value of β/R here obtained is in agreement with the values found in the FIM and FEM measurements treated in Chapter 3 as well as for metallic emitters [69].

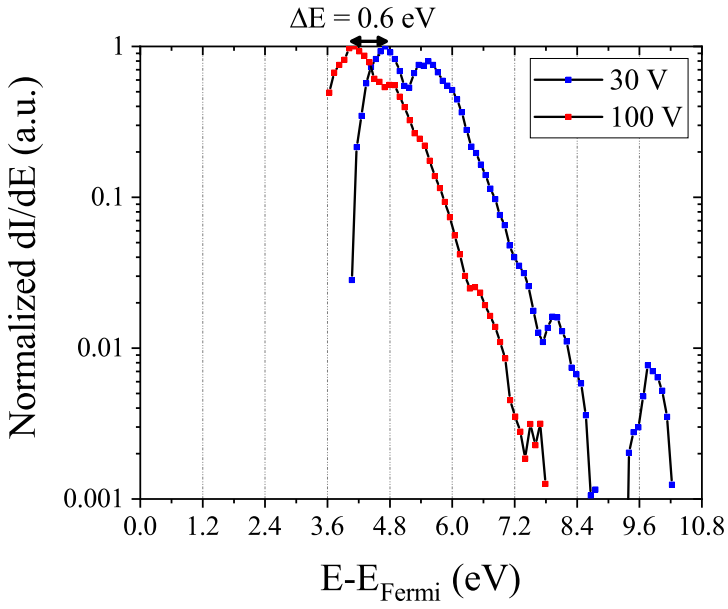

Figure 4.21: Electron energy spectra shift taken at 100 kHz with laser peak intensity of 18 GW/cm^2 for $V_{tip} = 30\,V$ (blue dots) and $V_{tip} = 100\,V$ (red dots).

Considering an applied voltage $V_{tip} = 30\,V$ and an effective work function $\varphi_{eff} = 4.7\,eV$, inserting the value obtained for β/R in Equation 4.2 the work function value of $\varphi = 5.4 \pm 0.3\,eV$ is obtained. Similar value for the work function of diamond have been measured in literature on diamond nano-crystals [24].

Furthermore, at low repetition rate, the emission current has been monitored varying the laser repetition rate keeping the mean pulse energy in order to control for thermal effects (Figure 4.22). As one can see from the graph, in the measurements done at constant energy the current behaves linearly. This indicates that the increase in current is only due to the increase of the number of laser pulses hitting the sample in unity of time, excluding a thermal contribution to the electron emission.

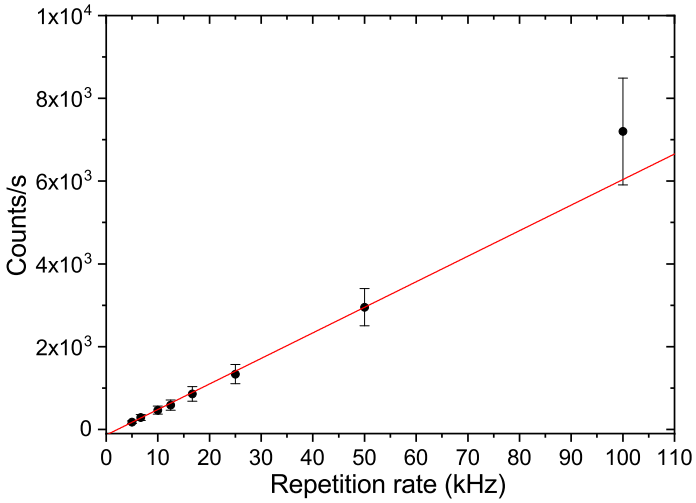

Figure 4.22: Emission current as a function of the laser repetition rate at fixed laser peak intensity of 21.8 GW/cm^2 at $V_{tip} = 100\,V$.

4.1.3 Electron energy spectroscopy at high laser repetition rate

Another study has been done on diamond emitters with the use of the laser illumination at high repetition rate of 2.35 MHz. In this case, as shown in Figure 4.23, the high repetition rate of the laser does not affect the shape of the emission spectra which continues to show each individual contribution of different multi-photon emission processes. This behavior, as a clear signature of multi-photon absorption process, rules out the thermal contribution of a possible pile-up effect of laser pulses.

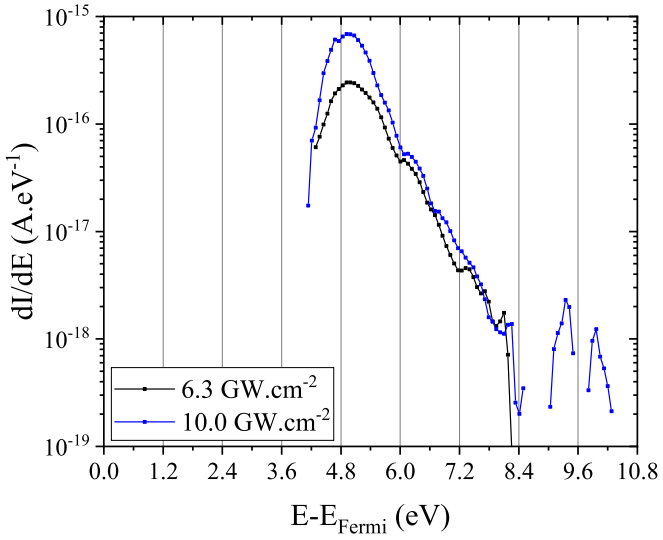

Figure 4.23: Electron energy spectra shift taken at 2.35 MHz at $V_{tip} = 100\,V$ for two different laser peak intensities.

This behavior can be explained taking into account the outstanding thermal diffusivity of diamond which is able to dissipate effectively the heat generated by laser illumination. A recent study of thermal diffusivity on these nano-needle diamond has been carried out Arnoldi et al. finding a thermal diffusivity of $D = 5.5 \pm 0.5\, cm^2/s$ [18]. This value, even though is lower than the bulk thermal diffusivity of bulk diamond, is high enough to justify a fast heat dissipation during analysis able to prevent thermal emission. Since these emitters do not show thermal emission, they can withstand higher repetition rates without being destructed by the high laser energies thanks to their high thermal diffusivity.

4.1.4 Laser polarization effects

In order to have a $cos^{2n}(\theta)$ curve in the polarization curve of Figure 4.6, it is necessary to have a good alignment on the tip apex in order to exclude a thermal contribution to the emission.

When the laser beam is focused farther from the tip apex, one can also observe a sinusoidal contribution. Indeed thermal processes are more efficient when the laser polarization is perpendicular to the tip axis and the increase of electron temperature promotes the electron emission. This contribution was observed on the sample Diamond HJ of Figure 4.1. Several absorption maps are shown for characteristic values of θ in Figure 4.24. The maps got for $\theta = 0°$ and $\theta = 180°$ correspond to a parallel polarization (maximum values of the emitted current). The maps got at $\theta = 105°$ and $\theta = 285°$ correspond to a perpendicular polarization (second set of current maxima). They display complementary patterns. So the emission sites change according to the involved process. For an intermediate value of θ, those two extreme patterns overlap ($\theta = 135°$ and $\theta = 315°$). The emission is only canceled for $\theta = 45°$ and for $\theta = 235°$.

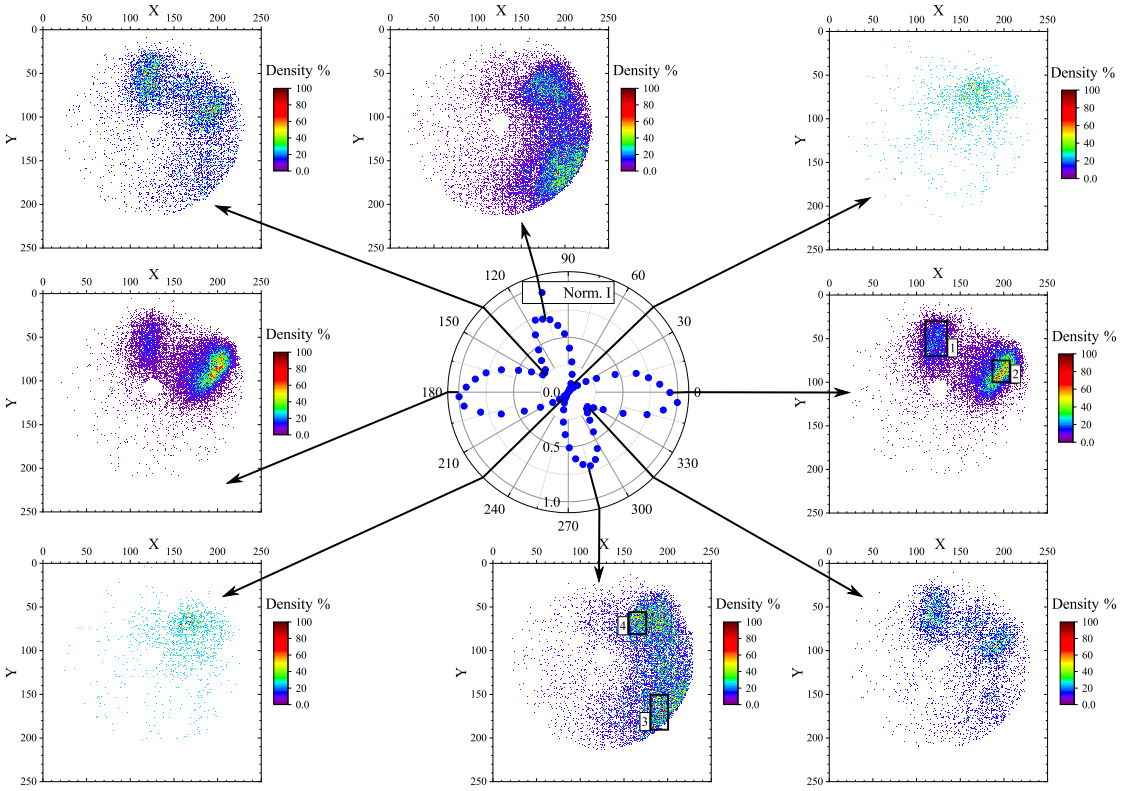

Figure 4.24: Normalized measured current as a function of the angle of polarization (θ) of the laser ($I_{peak} = 9GW/cm^2$, $V_{tip} = 100\,V$, repetition rate of 2.4 MHz). The laser polarization is parallel to the tip axis for $\theta = 0°$ and $\theta = 180°$. It is perpendicular to the tip axis for $\theta = 90°$ and $\theta = 270°$. The blue dots correspond to experimental data. Emission patterns are shown for characteristic values of θ.

A method to check the pole dependence of the emission processes is to restrain the study area, as in Figures 4.25, 4.26 and 4.27.

On Figure 4.25a, which corresponds to the polarization dependence of the pole 1 defined in Figure 4.24. It exhibits a $cos^{2n}(\theta)$ behavior with $n = 5$, that denotes a multi-photon emission with 5 photons preferentially absorbed by electrons before their emission into vacuum. The corresponding energy spectra are displayed in Figure 4.27a and they confirm the multi-photon process. So pole 1 is only activated by multi-photon process. One can observe a similar behavior for pole 2 even if Figure 4.25b shows a little pollution by a perpendicular contribution.

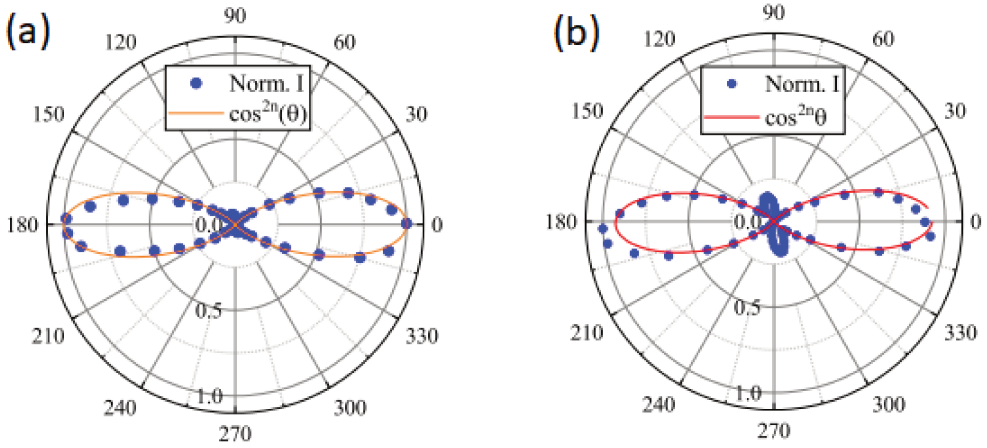

Figure 4.25: Normalized measured current as a function of the laser polarization angle ($I_{peak} = 9GW/cm^2$, $V_{tip} = 100\,V$, repetition rate of $2.4\,MHz$) for selected parts of the CCD image. Measured current from (a) area 1 and from (b) area 2 defined in Figure 4.24.

The same study was performed for pole 3 and pole 4 defined in Figure 4.24. The emission from pole 3 is maximized for perpendicular polarization and equal to zero for parallel polarization (Figure 4.26a). However pole 4 shows a little contribution of multi-photon emission ($\theta = 0°$ and $\theta = 180°$) due to an overlap of poles 2 and 4 of Figure 4.24.

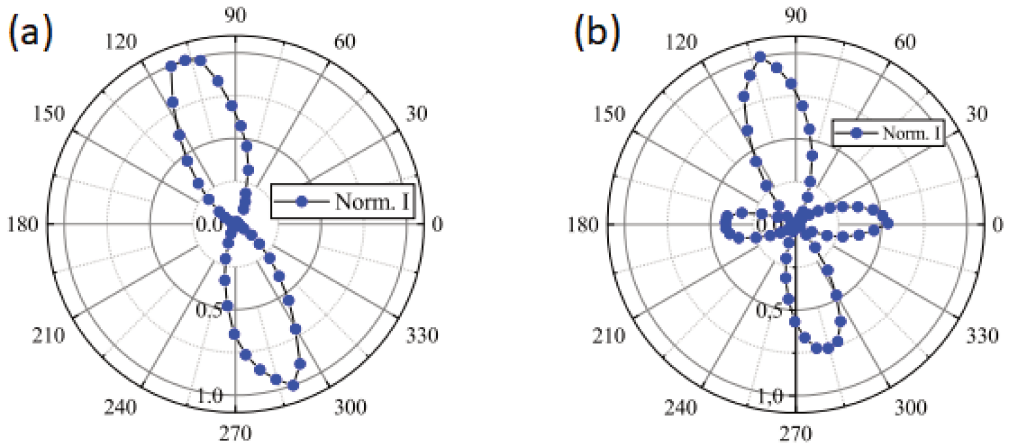

Figure 4.26: Normalized measured current as a function of the laser polarization angle ($I_{peak} = 9GW/cm^2$, $V_{tip} = 100\,V$, repetition rate of $2.4\,MHz$) for selected parts of the CCD image. Measured current from area 3 (a), and from area 4 (b) defined in Figure 4.24.

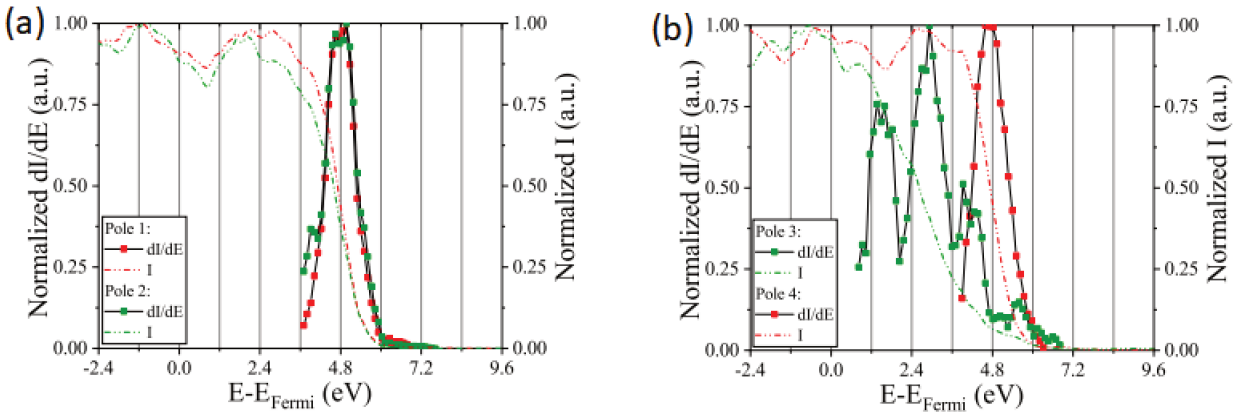

Figure 4.27: Energy spectra obtained from selected areas defined in Figure 4.24: (a) Spectra (squares) and current (dashed line) obtained from areas 1 (red) and 2 (green) for $\theta = 0°$ (parallel polarization). (b) Spectra (squares) and current (dashed line) obtained from areas 3 (green) and 4 (red) for $\theta = 105°$ (perpendicular polarization).

Figure 4.24 shows that changing the polarization from axial to perpendicular the emission region 1 disappears and the new emission in region 3 appears. Moreover, the emission region 2 changes in shape to emission region 4. Looking at the spectra obtained from each single region 1, 2 ,3 and 4, the emission process seems to be the same for the regions 1, 2 and 4, corresponding to field emission by 4 photons absorption (Figure 4.27a), however low energy electrons are emitted from region 3, corresponding to field emission assisted by 2, 3 and 4 photons absorption (Figure 4.27b). One possible explanation is that the static field is higher in region 3, inducing a stronger bending of the barrier compared to region 1, 2 and 3. This can be due to the presence of a local asperity at the surface of the needle which enhances the static electric field. If the static field is enhanced, then emission assisted by the absorption of 2, 3 or 4 photons can be observed (Figure 4.28). Moreover, using a perpendicular polarization, the optical field is enhanced close to these asperities, which is not the case for axial polarization. This can explain the $sin^{2n}(\theta)$ behavior reported in Figure 4.26a.

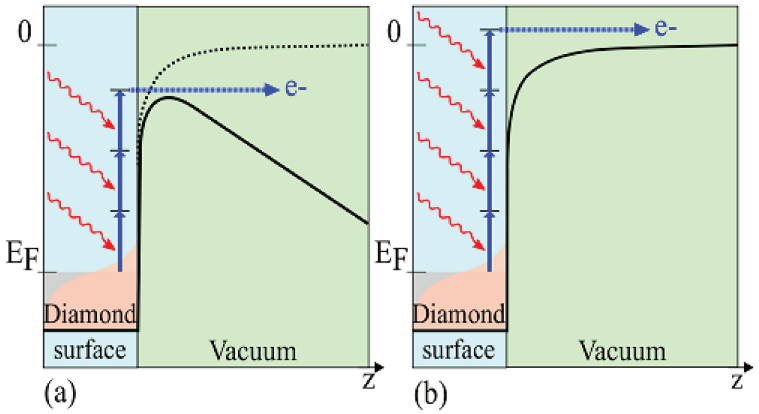

Figure 4.28: Schemes of emission processes: (a) field emission process from region 4 and (b) from region 1, 2, and 3.

To verify that the regions where the optical field is enhanced are polarization dependent, we perform numerical simulation using the commercial software Lumerical to solve Maxwell equations in the 3D geometry of the diamond sample (Figure 4.29).

The calculations show that using axial polarization the field is higher at the apex of the sample, however using perpendicular polarization the field is enhanced on the border of the apex, where more asperities are observed by TEM images of our diamond samples. Therefore, changing the polarization, different emission areas are activated by the laser at the sample surface.

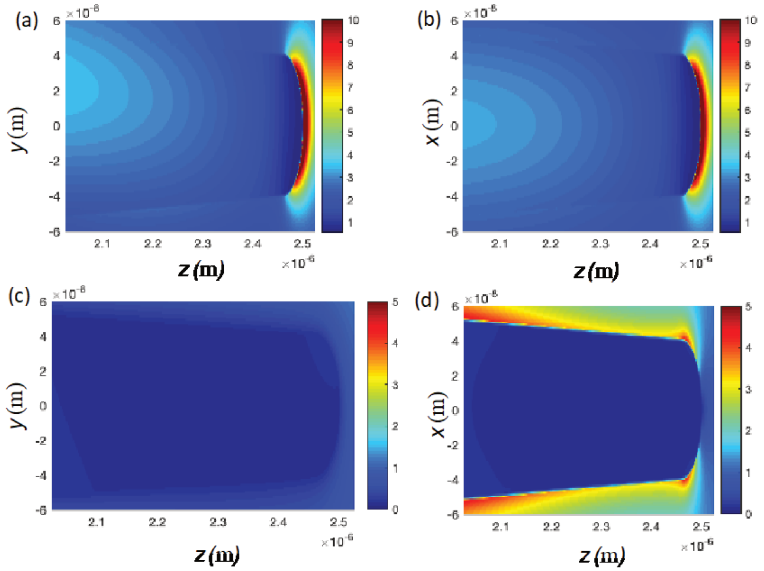

Figure 4.29: 2D maps of the optical field for axial polarization (along the "z" axis) (a) and (b) and for perpendicular polarization (along the "x" axis) (c) and (d).

4.2 Single crystal CVD diamond emitters with voltage drop

In some cases, when the diamond needles have a clean surface free of graphitic phase, the nano-needles present an energy deficit of the emitted electrons. As in the precedent case without voltage drop, the laser influence on the emission mechanism has been studied as well as its effect on the $I - \Delta V$ characteristic. Diamond emitters which present voltage drop have been studied under laser illumination in multiple systems. In collaboration with the LCAR of Toulouse University under a IR laser of $\lambda_{IR} = 1030\,nm$ with a pulse duration of $300\,fs$ where I spent there a month in order to do analyses. And as well as in the GPM laboratories under two different lasers, the one given by the CORIA laboratories ($\lambda_{IR} = 1040\,nm$, pulse duration of $500\,fs$ and a variable repetition rate up to $18.8\,MHz$) and a borrowed commercial laser called Brevity-Lambda+ given by S.A.S. NOVAE of $\lambda_{IR} = 2110\,nm$ with a pulse duration of $90\,fs$ working at a repetition rate of $20\,MHz$.

4.2.1 Toulouse analysis results

In the laboratory of the University of Toulouse a preliminary study on the effect of laser illumination has been carried out on our diamond samples. The study of electron emission has been done on the same diamond tip described in Chapter 3. In fact, in addiction of the measurements on the internal electrical conduction, measurement of field emission has been also done in the presence of IR laser. The laser is focused on the tip with the use of a spherical mirror inside the chamber which permits a laser beam diameter at the focus of about $5\mu m$. This implies a much higher focalization in comparison with the measurements done with the use of an external lens (diameter at the focus of about $45\,\mu m$).

In this case, illuminating the sample with laser gives a change in the emission pattern as well as a modification of the emission current and the kinetic energy of the emitted electrons. The emission pattern are shown in Figure 4.30, with and without laser illumination.

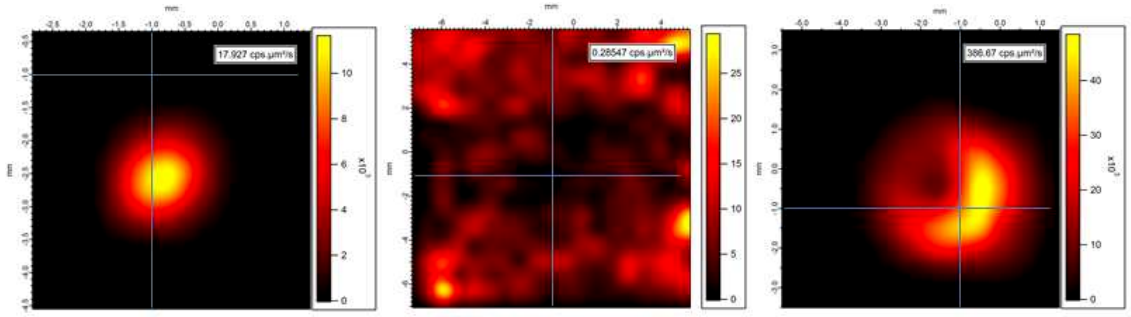

Figure 4.30: Field emission pattern at $V_{tip} = 250\,V$ in the case of no laser illumination (on the left) and increasing the laser peak intensity (in center $I_{laser} = 1.02 \cdot 10^3\,GW/cm^2$ and on the right $I_{laser} = 2.04 \cdot 10^3\,GW/cm^2$).

As shown by the left image of Figure 4.30, the static emission presents a single spot of emission, while applying the laser illumination on the tip changes the emission pattern in a peculiar way. In fact, increasing the laser intensity, the static emission starts to disappear reaching a threshold of intensity where there are no more impact on the detector (in the case of $V_{tip} = 250\,V$ of Figure 4.30, the threshold is around $I_{laser} = 1 \cdot 10^3 GW/cm^2$). Increasing furthermore the laser illumination, the emission pattern reappears with a new form characterized by a ring shape of emission, where the brighter area is in the opposite of the direction of the laser beam on the tip, which shrinks in size with the increase of laser intensity as shown in Figure 4.30. This behavior has been observed for other diamond samples as well as at different applied voltages on the tip.

Along with the change in emission pattern, during the increase of laser intensity, also the emission current is modified as well as the voltage drop present on the sample which is the difference between the applied voltage on the base of the sample and the kinetic energy K of the emitted electrons divided by the electron charge e, $\Delta V = V_{tip} - K/e$. As shown in Figure 4.31, the emission characteristic changes completely with the laser illumination. In particular, the voltage drop during emission starts to increase approaching the laser intensity threshold. Once the intensity is higher than the threshold, the drop increases of about $100V$ for every applied voltage probed. On the other hand, before the threshold, the current decreases until almost disappear at the threshold. While with a laser illumination of intensity higher than the threshold, the current rises rapidly of one or two order of magnitude.

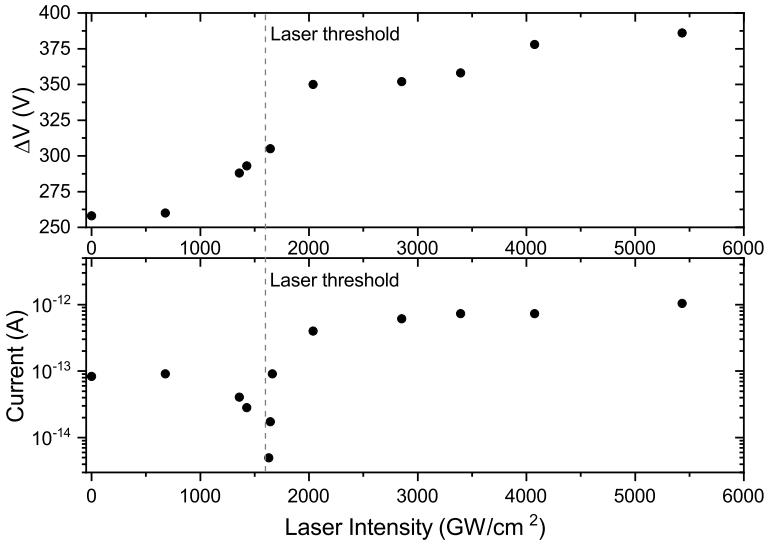

Figure 4.31: Voltage drop and emission current as a function of the laser peak intensity at $V_{tip} = 800\,V$.

Since the laser illuminates only the apex of the diamond needle, the conduction mechanism is not affected. In the case of Poole-Frenkel conduction, an increase of current is directly reflected in an increase of voltage drop. In the point of view of the emission pattern change, a possible explanation is the fact that the laser illumination above threshold is strong enough to deplete a region near the apex, making the needle emit from the surface below it, as schematized in Figure 4.32.

The electrons trajectories were calculated considering that a small spherical cap, close to the symmetry axis of the needle, is positively charged, whereas all the other surface of the needle is at a negative voltage of $100\,V$. The detector system is polarized as reported in the previous Figure 4.17.

Due to the 2D revolution symmetry of the simulation, only the trajectories from half of the emitter section are reported in Figure 4.32. Moreover, when trajectories cross the symmetry axis "z", they appear as reflected back.

Electrons emitted from the region at the border of the positively charges spherical cap, cross the symmetry axis of the field emitter (the "z" axis) and will design on the detector a ring impact area. Increasing the laser intensity, the area of the spherical cap positively charged will increase, therefore the electrons emitted from the border of this cup will cross the "z" axis far and they will impact the detector in a ring area with a smaller diameter, as experimentally observed.

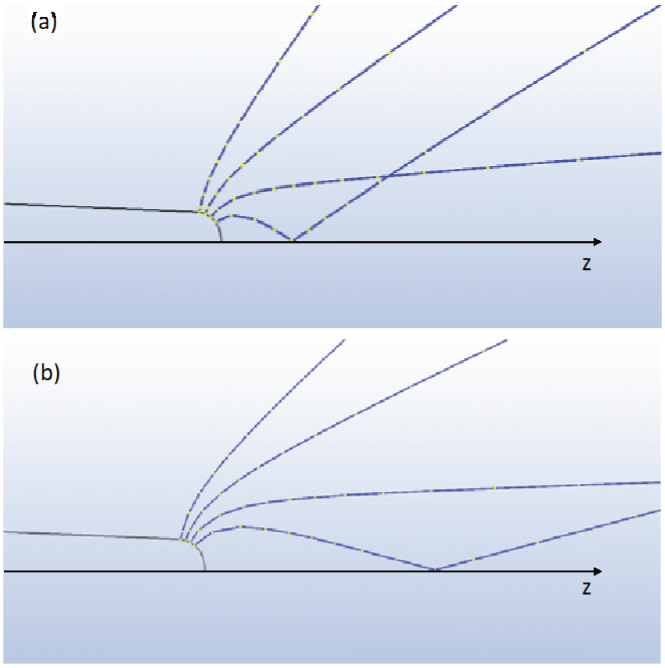

Figure 4.32: Simulation of electrons trajectories from a field emitter having a spherical cap positively charged: (a) small spherical cap, (b) larger spherical cap.

In order to try to better understand the dynamic of charge and discharge of the spherical cup at the apex of the diamond field emitter, a preliminary study of how the laser pulses interact with the emission has been done. In detail, a $200\,ns$ gate window has been placed on the detector during pulses and between them in order to try to measure the current during and off pulses. In this mode, using low laser repetition rates, it was possible to show that the electron emitted thanks to the laser are indeed emitted by packets during laser pulses as shown in Figure 4.33.

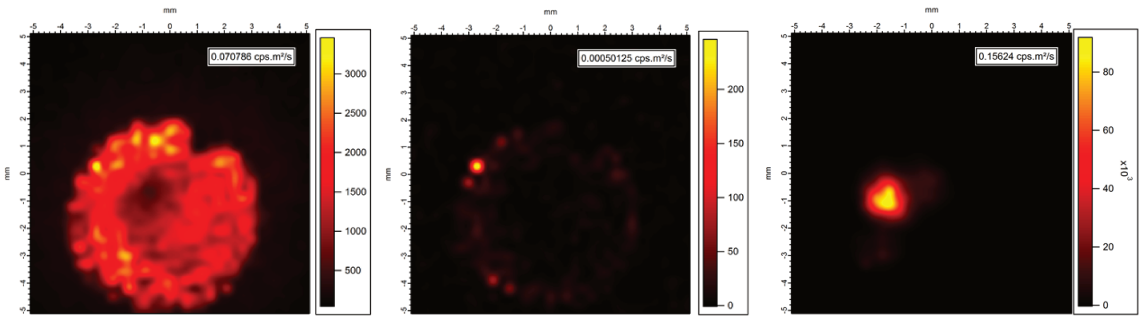

Figure 4.33: Emission pattern at $V_{tip} = 500\,V$ during a gate of $200\,ns$: on the left during pulse, in the center between laser pulses at $10\,kHz$ laser repetition rate while on the right at $1\,kHz$.

As one can see from Figure 4.33, the laser pulses induce a burst of emission during pulses while between them no emission occurs. In the case of a low repetition rate as

1 kHz (on the right of Figure 4.33), instead the diamond needle has sufficient time to restore its static emission regime. In order to study the time that the sample takes in order to restart to emit electrons in static regime, a measurement of the current between pulses has been done moving a 50 μs gate between pulses (Figure 4.34).

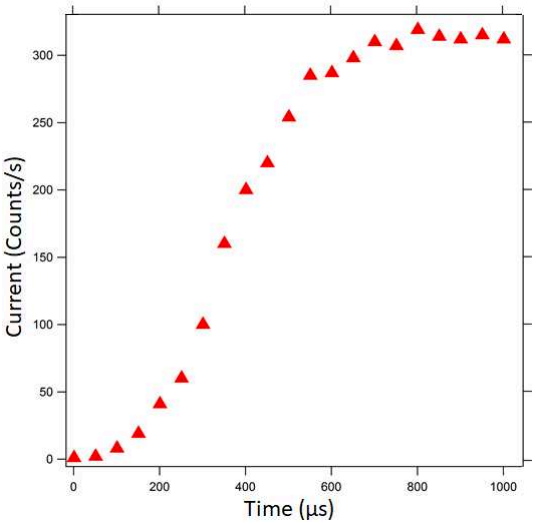

Figure 4.34: Static emission current over time between laser pulses measured moving a 50 μs gate from a pulse to the next one at 1 kHz laser repetition rate.

From the graph of Figure 4.34, the time the diamond takes to restart to emit in static regime is around 100 μs reaching the max current at around 600 μs. Since the static emission needs a minimum time to restart after a laser pulse, it can be nullified with a repetition rate sufficiently high, in this case 10 kHz.

4.2.2 Rouen results

In the GPM laboratories, after the analysis done on diamond tip which do not present voltage drop, a golden mirror has been placed inside the vacuum chamber in order to increase the laser focalization on the samples. This new focalization method, compared to an external lens, consent a laser focalization on the tip apex of about 5 μm of diameter. With this set-up, two laser systems have been implemented, the CORIA laboratory fiber laser and the commercial laser Brevity-Lambda+. Unfortunately, due to difficulty of sample preparation and requirements for the detecting set-up (emission below 700 V), finding diamond samples which present voltage drop at emission threshold below 700 V has been challenging. In fact, in this case, only one diamond tip which present an energy deficit has been successfully analyzed in this setup. The sample analyzed is shown in Figure 4.35, this tip presents a length of about 20 μm with a radius on the apex of about 40 nm.

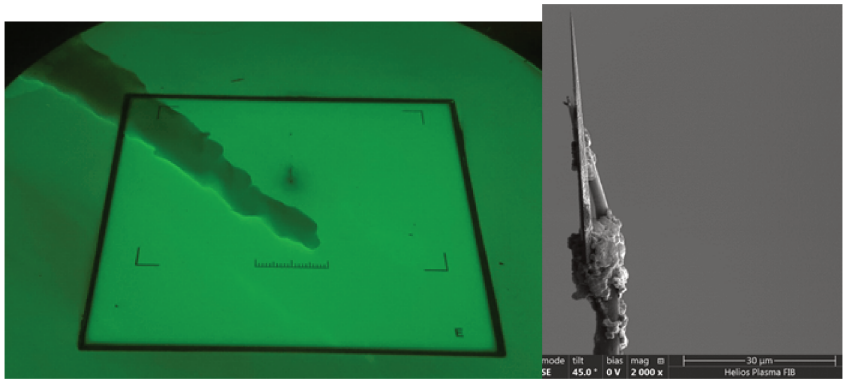

Figure 4.35: Diamond G9. On the left a TEM photo taken at a magnification of $50k$, the scale length correspond to approximately $400\,nm$; on the right a SEM photo of the needle glued on the W support.

During the preliminary test in static regime, a very small voltage drop has been observed, and the FN curve is linear as the case described above (Figure 4.2), shown in Figure 4.37a, where $V_{apex} = V_{tip} - \Delta V$. The static emission pattern is shown in Figure 4.36a, as well as an example of emission spectrum in static regime, in this case with $V_{tip} = 710\,V$ (Figure 4.36b), where the voltage drop can be obtained through $\Delta V = V_{tip} - E_{Fermi}/e$.

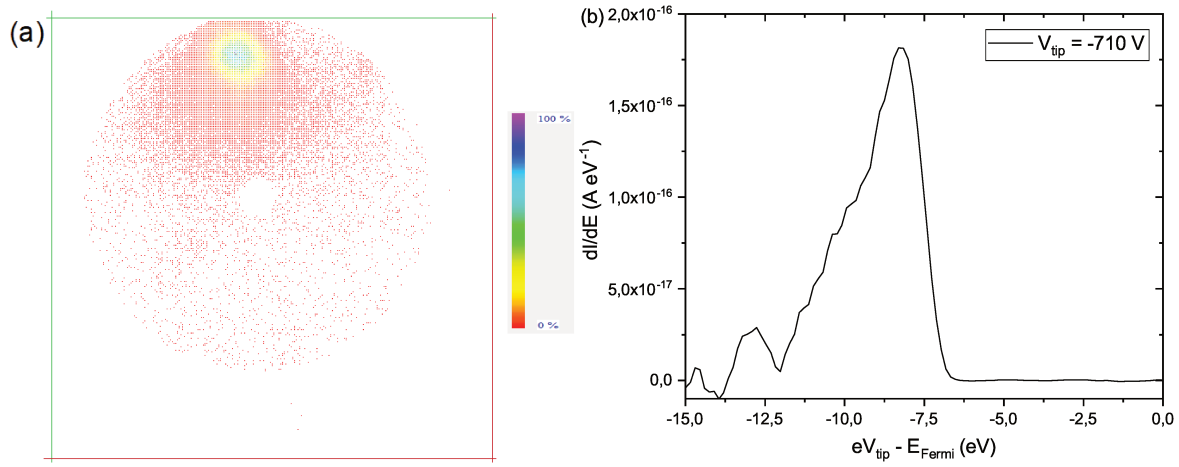

Figure 4.36: (a) Emission pattern of Diamond G9 in static regime. (b) Electron emission spectrum with $V_{tip} = 710\,V$ showing a $\Delta V = 7.5\,V$.

This tip presents a small voltage drop during static measurements (Figure 4.37b), of the order of 1%.

Furthermore, as other cases described in this thesis, the FN curve in static regime is linear as well as the voltage drop as a function of the applied voltage (Figure 4.37).

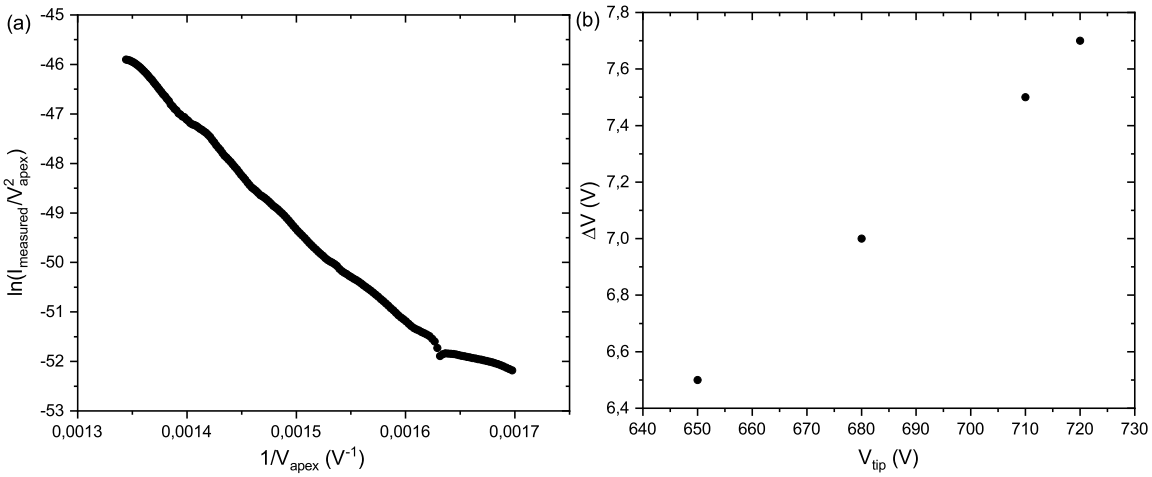

Figure 4.37: (a) FN plot in static of Diamond G9 in dark with an applied voltage ranging from $590\,V$ to $760\,V$. (b) Voltage drop as a function of the applied voltage V_{tip} calculated from static emission spectra.

4.2.2.1 CORIA laboratories $1\,\mu m$ fiber laser

This tip has been initially characterized with the use of the fiber laser given by the CORIA laboratories at $\lambda = 1040\,nm$ with a repetition rate of $18.8\,MHz$, in order to test the behavior of the sample under laser illumination. In this case, the laser assisted emission has been carried out at applied voltages of $V_{tip} = 50\,V$ which is well below the threshold for static emission ($\sim 500\,V$). In order to preserve the sample from damage or falling from the W support, the data collected on this sample are not exhaustive. In particular, the electron emission as a function of the laser polarization angle has been studied as well has energy emission spectra increasing the laser intensity. In Figure 4.38, the emission pattern under illumination is shown. This emission pattern does not change shape increasing the laser intensity or polarization.

In Figure 4.39, the laser polarization and the emission spectra are shown. As one can see, from the polarization plot, there are maxima of emission for four different angles of a complete turn of the $\lambda/2$ plate, separated by an angle of 180°, indicating an emission not affected by thermal effects. The emission law follows the $\cos^{2n}(\theta)$ where in this case $n = 5 - 6$, evidence of multi-photon absorption. The energy emission spectra show a difference in the energy which is lower than the energy corresponding to the applied voltage (0 in the abscissa axis of the right graph of Figure 4.39) indicating a small voltage drop along the tip. From the result of the polarization plot (5 photon absorption), a voltage drop of about $\Delta V = 9.6 \pm 0,6\,V$ can be obtained. Another remark on the ability of these nano-needle to dissipate effectively the heat is the fact that at even this high repetition rate of the laser no thermal effects are observed both in the polarization plot as well as the energy spectra.

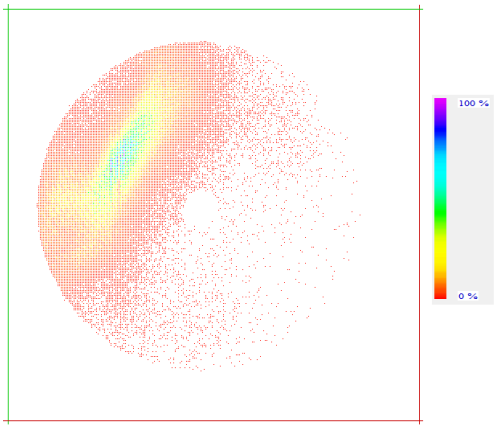

Figure 4.38: Emission pattern under laser illumination at a peak intensity of $9.5 GW/cm^2$at a laser repetition rate of 18.8 MHz and $V_{tip} = 50\,V$.

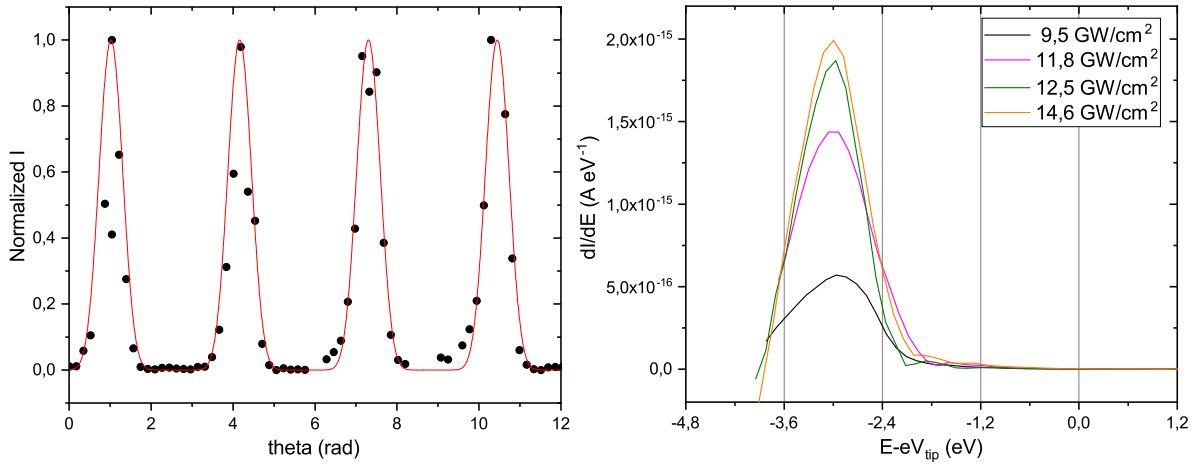

Figure 4.39: On the left, emission current as a function of the laser polarization angle at 10.1 $GW/cm^2$of peak intensity and $V_{tip} = 50\,V$, fitted with a $\cos^{2n}(\theta)$ behavior. On the right, emission spectra at different laser peak intensities taken at an applied voltage of 50 V at a laser repetition rate of 18.8 MHz.

4.2.2.2 Brevity-Lambda+ 2 μm fiber laser

Using a commercial laser at 2 μm, the emission has been monitored from the diamond G9. In this case, the emission at high applied voltage as well as at low applied voltage has been done. The practical use of this laser is more complicated respect to the 1 μm due to the fact that we do not have a camera which can see the diffraction pattern of the laser on the tip, so the right alignment on the sample apex is challenging. In fact, in order to align the laser on the tip, an high power has been used scanning the tip to search emission triggered by the laser. As this process was done, the electrical conduction properties of the sample changed, leading to a not anymore negligible voltage drop. This modification is reflected directly on the FN curve in dark as well as the voltage drop as

a function of the applied voltage shown in Figure 4.40. In this case, opposite to the case of Figure 4.37, the FN curve present the characteristic of a non conductive material: a linear part at low applied voltage, followed by a saturation region and at high voltage a sharp increase of the current with a low change in voltage. In the inset of the left graph of Figure 4.40, the PF plot results linear indicating a internal electrical conduction of the Poole-Frenkel type.

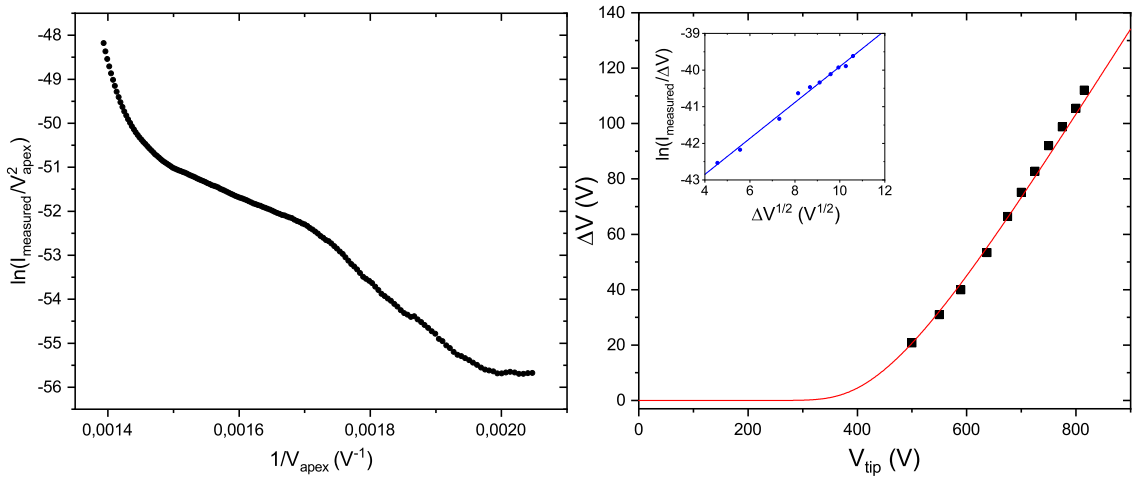

Figure 4.40: On the left FN curve in dark of Diamond G9. On the right voltage drop as a function of the applied voltage, the line corresponds to the computed values using Equation 3.16 of Chapter3 using the same procedure with the linear fit of the FN corresponding to the linear part at low applied voltages.

With the change in voltage drop, also the emission pattern changed, as shown in Figure 4.41, where the emission is now localized in the center of the detector.

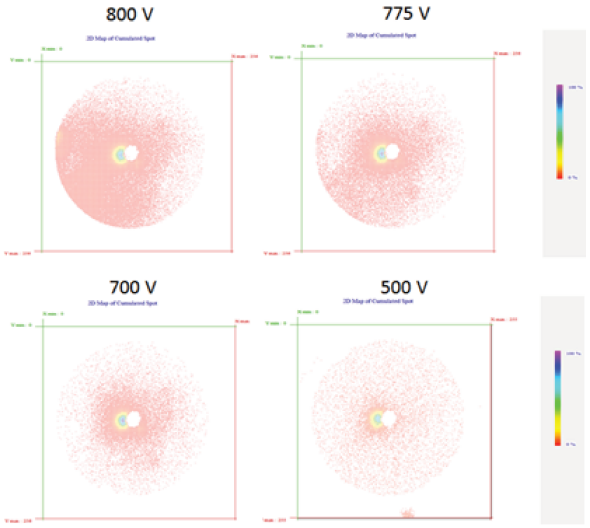

Figure 4.41: Static field emission patterns after change in the voltage drop.

As seen in the previous case of Toulouse results, when focusing the laser only on the apex of the diamond needle, the voltage drop increases instead of decreasing as was in the FIM case, reported in the Chapter (insert reference chapter conduction) where the laser illuminates the totality of the sample (Figure 4.42).

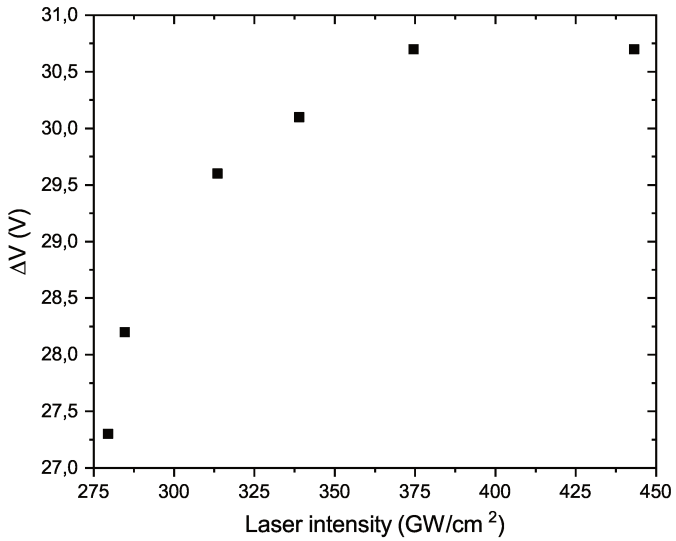

Figure 4.42: Voltage drop evolution as a function of the laser peak intensity at an applied voltage of $V_{tip} = 80\ V$.

The voltage drop evolution under laser illumination follows the same pattern as seen in precedence on the diamond F16 analyzed in Toulouse above the threshold laser peak

intensity (see Figure 4.31).

Another factor of similarity between the two cases is given by the emission patterns during emission (Figure 4.43), where the appearance of a ring shape emission takes place. In this case, compared to the case of the measurements done in Toulouse, an emission under the minimum laser intensity here reported could not been found, indicating that under this threshold only static emission is possible.

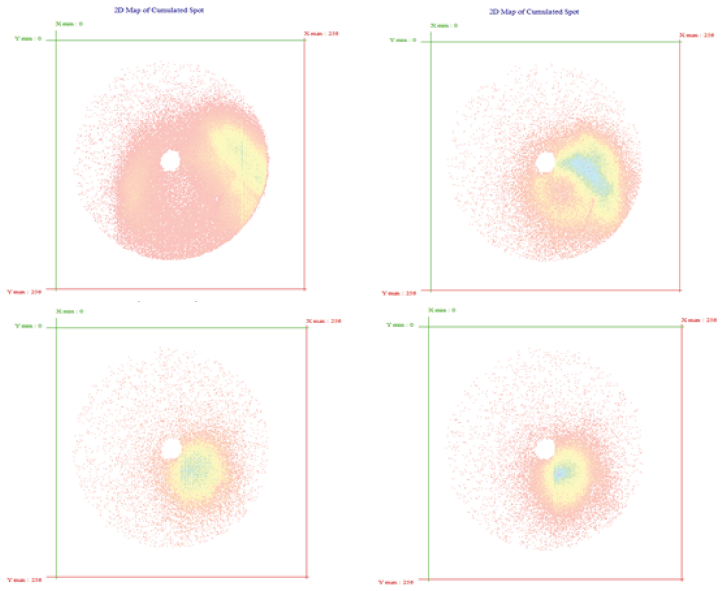

Figure 4.43: Field emission patterns at $V_{tip} = 80\,V$ increasing the laser peak intensity (top left $I_{laser} = 279 GW/cm^2$, top right $I_{laser} = 285 GW/cm^2$, bottom left $I_{laser} = 314 GW/cm^2$ and bottom right $I_{laser} = 374\, GW/cm^2$).

From the emission pattern one can see that the ring shape shrinks back in an single emission dot at high enough laser intensity.

Before performing energy spectra, a study of the emission current as a function of the laser polarization angle has been done, also in order to confirm a good alignment of the laser on the apex (Figure 4.44). The $cos^{2n}(\theta)$ law gives an $n \sim 8 - 10$ suggesting an up to 8-10 multi-photon absorption process.

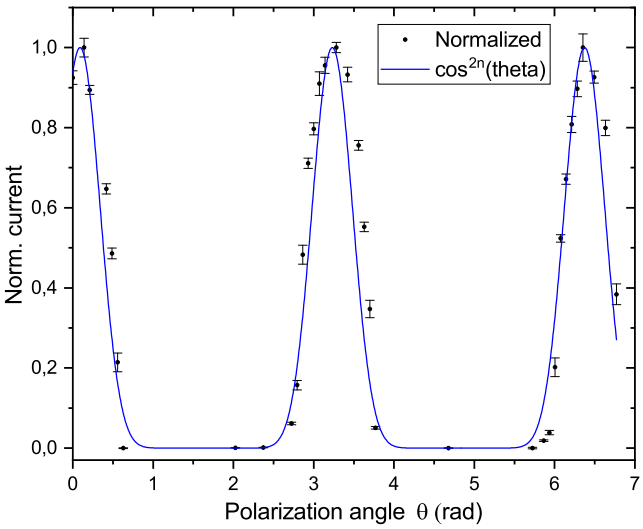

Figure 4.44: Emission current as a function of the laser polarization angle at $297\,GW/cm^2$of peak intensity at $V_{tip} = 80\,V$.

The energy deficit shown in Figure 4.42, has been obtained through the Spectra taken at $V_{tip} = 80\,V$ of Figure 4.45. In order to acquire these energy spectra, since the emission current is high enough to saturate the detector system, the gain on the MCPs has been decreased so that the electron amplification does not damage the MCPs as well as the total current hitting the phosphorous screen for camera detection. With this method of analysis, the current measured is not anymore the real total current but is biased by a factor which depends on the voltage applied on the MCPs for the amplification of the system. This current in Figure 4.45 has been corrected in data analysis with a reference current taken at the good working gain on the MCPs. Even with this correction, the value of the current measured cannot be considered accurate. As a second method to have the current, we tried measuring it with the use of a pico-amperometer (Model 6485 of Keithley Instruments) directly connected on the sample with the use of a transformer in floating mode, but the background noise and capacity effects taking place during analysis made it impossible to have a measurement.

As shown in Figure 4.45, the general shape of the emission spectra remain the same as the precedent cases with multi-photon absorption. Considering the fit of Figure 4.44, we can deduce that the spectra reflect multi-photon absorption of 8 and more photon suggesting a Fermi level lower of about $4\,eV$ shifting the plot of Figure 4.42 of $4\,V$ to higher voltage drop.

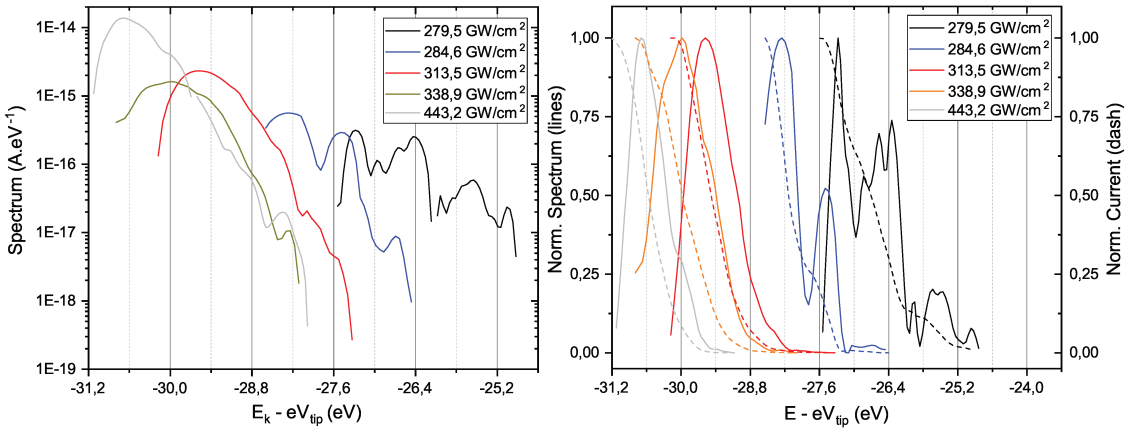

Figure 4.45: Energy spectra taken at $V_{tip} = 80\,V$ increasing the laser peak intensity, in semi-log scale (on the left) and linear scale (on the right).

Since the LEED is a 2D detector, restricted zone on the detector can be selected in order to extract the local energy spectrum. In the case of the ring pattern of Figure 4.43 at the up-right corner taken at $I_{laser} = 279\,GW/cm^2$, the local spectra of the high current local zone and its opposite have been taken and shown in Figure . As one can see, the electron kinetic energy of the two different zone are very similar meaning that electron are emitted with the same energy throughout the ring pattern.

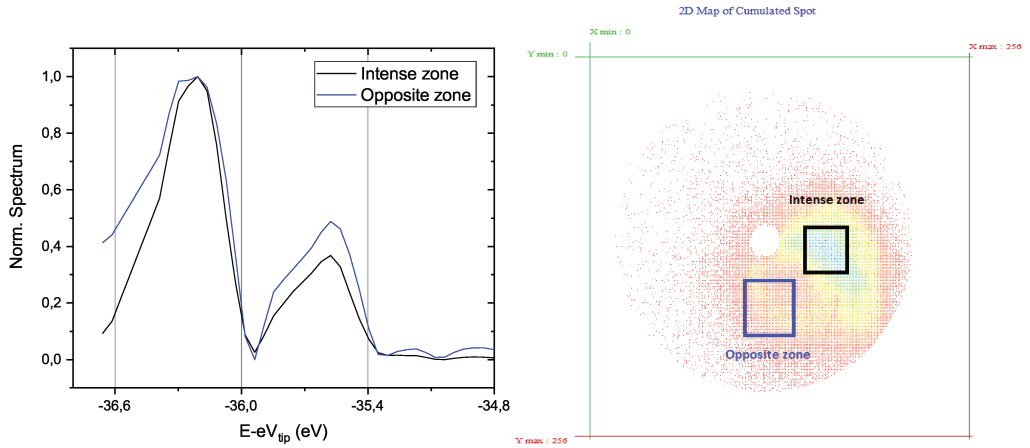

Figure 4.46: Two different emission spectra taken at $V_{tip} = 80\,V$ from two different regions of the emission ring pattern at $I_{laser} = 279\,GW/cm^2$.

Along with the emission behavior at low applied voltage ($V_{tip} = 80\,V$), a study of the emission has been done as well as in the case of high applied voltage ($V_{tip} \geq 500\,V$).

In the same condition, the behavior of the voltage drop has a function of the laser peak intensity has been monitored also at high applied voltage, such as $V_{tip} = 660\,V$. As shown in Figure 4.47, in the case of high applied voltage, the voltage drop decreases with the increase of laser intensity until completely disappear above a threshold of $I_{laser} \geq 250 GW/cm^2$. Another observation is the fact that at this high applied voltage the emission pattern differs with the one at low applied voltage of Figure 4.43 where a ring shape appears. In this case, the emission is the one of a single spot of emission unchanging in shape with the modification of the laser intensity. With the laser intensity available, it was also not possible to suppress the static emission as in the case of Toulouse experiments of Figure 4.30, where at a certain laser intensity the static emission is suppressed with the appearance of a ring shape of emission at high laser intensity. This could be due to the fact that in the case of the Brevity-Lambda+ laser, the available laser power was not enough to trigger such effect which appeared only in the case of low applied voltage.

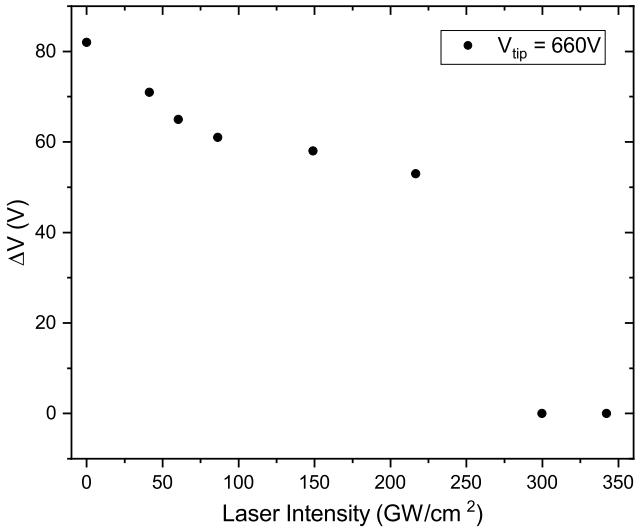

Figure 4.47: Voltage drop as a function of the laser peak intensity in the case of high applied voltage: $V_{tip} = 660\,V$.

4.3 Conclusions

In this chapter, electron emission from diamond nano-needle has been studied in a preliminary study with the assistance of femto second lasers in the IR frequencies at $\lambda = 1030nm$ and $\lambda = 2100\,nm$. This study has been done for both low and high laser repetition rates, without the appearance of thermal effects due to pile up of laser pulses thanks to the outstanding thermal conductivity of diamond which makes it also highly resistant to damage during analysis, distinguishing it from other studied materials such as carbon nano-wires. Another characteristic that makes diamond appealing for field emission application is the high emission stability over time without degradation of the emission current density over time. Our sample can also have different characteristics, such as the presence or not of electron energy deficit during analysis.

Sample which do not present voltage drop have been largely studied in static and under laser illumination regimes. Under laser illumination, the emission current is strongly enhanced with a strong dependence on the laser polarization angle. We observe multi.-photon absorption at low applied voltage on the samples while at higher voltages the emission is of the photo-field emission regime. Acquiring electron energy spectra we can obtain the work function of the emitters as well as their enhancement factor.

On the other hand, in the case of diamond emitter which present an energy deficit, we show a peculiar emission pattern (ring shape) under laser illumination with an increase of the voltage drop when illuminating only the apex of the sample. Furthermore, we show that under laser pulses, the whole emission is localized in time during pulses with a time window with no current between laser pulses of around $100\,\mu s$. Switching to a $2\,\mu m$ laser, the emission is comparable with the previous $1\,\mu m$ case, with the appearance of the same emission pattern and similar voltage drop and energy emission spectra.

With this work, we show that diamond nano-needles are excellent candidates for high repetition rate ultra-fast electron sources and for the study of strong field phenomena on carbon materials.

Conclusions and perspectives

In this dissertation, I presented the study of electrical conduction and field emission properties of single crystal CVD diamond nano-needles. This study has been conducted using two different experimental setups, namely FIM and FEM, in different configurations with and without ultra-fast laser illumination. The aim of the work was the measure of the electrical and optical properties of nano-size, non-conductive materials, in particular diamond needles.The study of diamond has been widely discussed by the scientific community but never in the specific conditions of our work: nano-metric dimensions of the sample, ultrashort laser illumination and high electric static field. However, only a few works on laser-assisted field emission from non-conductive material are published so far.

The first two chapters permitted to introduce the theoretical basis and the two experimental setups used in this work (FIM and FEM). These two techniques permitted the study of the electrical conduction inside the samples in relation to the sample geometry and the experimental conditions. On the other hand, with the use of FEM the emission characteristic of diamond has been monitored in static regime and laser illumination regime.

In Chapter 3, the experimental results on the conduction mechanism in diamond are presented. FIM permitted to emphasize that the geometry of the sample can play an important role in driving the conduction mechanism from an Ohmic conduction toward a Poole-Frenkel (PF) conduction type. Various models have been introduced in order to describe the conduction properties in a qualitatively and quantitatively way for the I-ΔV and V-ΔV characteristics. Under laser illumination, free carriers are generated inside the needle and they contribute to the conduction. The study of the the sample's temperature increase induced by the laser gives information on the trap levels that drive the PF conduction mechanism. A model which considers both the conduction and the emission has been introduced in order to explain the I-ΔV and V-ΔV characteristics during electron emission without and with laser illumination. Furthermore, the trap level measured with this technique is in agreement with the results obtained using the FIM setup and the results reported in literature [26].

Chapter 4 is devoted to the presentation of the experimental results on laser-assisted

field emission. Our findings show that field emission results from a multi-photon absorption process taking place at the apex surface of the sample where a strong field enhancement is present. In this study, two different type of diamond samples have been analyzed: samples exhibiting a voltage drop and others without voltage drop. The samples without voltage drop are good candidates for static field emission, thanks to the emission stability over time compared to metal emitters. When the laser is illuminating the tip, these samples withstand pulsed emission at high repetition rates and high laser intensities thanks to their good thermal conduction and mechanical resistance. On the other hand, in the case of diamond samples with voltage drop, the static emission can be shut down with the use of the laser. This can be used to control the pulsed electron emission by the laser even above the static emission threshold. This could be useful for time resolved electron microscopy.

Part of my work in the GPM laboratory was focused on the implementation and calibration of the various experimental setups. In the FIM setup, a new system for the measure of the current on the detector has been implemented. On the other hand, at the beginning of this project, the FEM setup was barely functional. The experimental bench has been first upgraded by the installation of a new detector (Argus spectrometer). In a second time, this detector has been substituted by the LEED spectrometer allowing the addition of the ultra-fast laser. Furthermore, an acquisition and data processing software had been developed in order to do measurements. This setup is now fully operational and at the disposal of the laboratory in order to perform further analysis on diamond samples or for the analysis of new kind of materials.

The results presented in this manuscript describe the electrical conduction and electron emission of these diamond nano-needle in different conditions of analysis. Concerning field emission, our work has revealed several advantages of diamond compared to metals, notably a higher electron emission stability and a higher damage threshold under ultra-fast laser illumination. With the application of ultra-short laser pulses, the electrons are emitted in packages, allowing the use of this source for time-resolved electron microscopy. As shown, diamond samples present different characteristics which are driven by their shape and their surface structure (amorphous or graphitic). So that, to increase the reproducibility from one diamond field emitter to another, the needle fabrication process has to be improved to better control the surface structure. Regarding the samples with voltage drop, this system could be used for the unusual emission patterns (ring shape emission) in new applications, but more studies are required to determine the conditions for the appearance of the ring emission patterns.

List of Symbols and Abbreviations

β	Field enhancement factor
β_{PF}	Barrier lowering coefficient
ε_0	Permittivity of vacuum
ε_r	Relative dielectric constant
θ	Laser's polarization angle
μ	Electron mobility
v	Thermal vibration frequency
ν_{laser}	Laser's photon frequency
ρ	Electrical resistivity
σ	Electrical conductivity
φ	Work function
ϕ_{PF}	PF trap level
a	Mean hopping distance
d_{PF}	Length of the region under PF conduction
e	Elementary electric charge
e^-	Electron
E	Electric field
E_a	Activation energy
E_g	Energy band gap
$f(\varepsilon, T)$	Fermi-Dirac distribution
h	Planck's constant
$\hbar$	Reduced Planck's constant
I_{peak}	Laser peak intensity
J	Current density
k_B	Boltzmann's constant
K_E	Kinetic energy
m_e	Electron's mass
n_e	Carrier's density
p	Pressure
R	Electrical resistance
T	Temperature
V_{apex}	Voltage at the apex of the samples

$V_{applied}$	Bias applied on the sample
AOM	Acousto-optical modulator
APT	Atom probe tomography
CAE	Constant analyzer energy
CB	Conduction band
CCD	Charge-coupled device
CNT	Carbon nano-tube
CRR	Constant retard ratio
CVD	Chemical vapor deposition
erfc	Complementary error function
FEM	Field emission microscopy
FIM	Field ion microscopy
FN	Fowler-Nordheim
GB	Grain boundaries
IR	Infrared
UV	Ultraviolet
LEED	Low-Energy Electron Diffraction
MCP	Micro-channel plate
PAFE	Photo-assisted field emission
PF	Poole-Frenkel
SCLC	Space charge limited conduction
TEM	Transmission electron microscopy
VB	Valence band

Bibliography

[1] Charles Kittel, *Introduction to solid state physics*, 8th edition, John Wiley & Sons Inc., (2005) 16-18.

[2] P. Hess, *The mechanical properties of various chemical vapor deposition diamond structures compared to the ideal single crystal*, Journal of Applied Physics 111 (2012) 051101.

[3] L. Wei, P. K. Kuo, R. L. Thomas, T. R. Anthony and W. F. Banholzer, *Thermal conductivity of isotopically modified single crystal diamond*, Physical Review Letters 70 (1993) 3764.

[4] C. D. Clark, P. J. Dean and P. V. Harris, *Intrinsic edge absorption in diamond*, Proceedings of the Royal Society A 277 (1964) 312-329.

[5] M. T. Yin and M. L. Cohen, *Ground-state properties of diamond*, Physical Review B 24 (1981) 6121.

[6] G. G. Raju, *Dielectrics in Electric Fields*, 2nd edition, CRC Press, (2017) Chapter 10.

[7] R. Nottenburg, K. Rajeshwar, M. Freeman, J. Dubow, *Dynamic Dielectric Analysis of Solid*s, Journal of Solid State Chemistry 28 (1979) 195-208.

[8] W. C. Lee and C. Hu, *Modeling CMOS tunneling currents through ultrathin gate oxide due to conduction-and valenceband electron and hole tunneling*, IEEE Transactions on Electron Devices, 48, no. 7 (2001) 1366–1373.

[9] C. D. Child, *Discharge From Hot CaO*, Physical Review. Series I. 32 (1911) (5) 492–511.

[10] J. H. Schon, Ch. Kloc, R. A. Laudise, and B. Batlogg, *Electrical properties of single crystals of rigid rodlike conjugated molecules*, Physical Review B 58, 19 (1998) 12952.

[11] M. W. J. Prins, K. O. Grosse-Holz, J. F. M. Cillessen and L. F. Feiner, *Grain-boundary-limited transport in semiconducting SnO2 thin films: Model and experiments*, Journal of Applied Physics 83 (1998) 888.

[12] G. E. Harlow, *The Nature of Diamonds*, Cambridge Univ Press, Cambridge, UK, (1998) pp 23–47.

[13] R. Robertson, J. J. Fox, A. E. Martin, *Two types of diamond*, Philosophical Transactions of the Royal Society A 232 (1934) 463.

[14] W. Kaiser, W. L. Bond, *Nitrogen, A Major Impurity in Common Type I Diamond*, Physical Review. 115 (4) (1959) 857.

[15] A. T. Collins, (1993). *The Optical and Electronic Properties of Semiconducting Diamond*, Philosophical Transactions of the Royal Society A 342 (1993) 233–244.

[16] C. D. Clark, H. Kanda, I. Kiflawi, G. Sittas, *Silicon defects in diamond,* Physical Review B. 51 (23) (1995) 16681.

[17] T. R. Anthony, W. F. Banholzer, J. F. Fleischer, L. Wei, *Thermal conductivity of isotopically enriched 12C diamond*, Physical Review B. 42 (2) (1990) 1104–1111.

[18] L. Arnoldi, M. Spies, J. Houard, I. Blum, A. Etienne, R. Ismagilov, A. Obraztsov, and A. Vella, *Thermal diffusivity of diamond nanowires studied by laser assisted atom probe tomography*, Appl. Phys. Lett., 112 (2018) 143104.

[19] W. Li, N. Mingo, L. Lindsay, D. A. Broido, D. A. Stewart, and N. A. Katcho, *Thermal conductivity of diamond nanowires from first principles*, Phys. Rev. B 85 (2012) 195436.

[20] R.U. Martinelli and D. G. Fisher, *The application of semiconductors with negative electron affinity surfaces to electron emission devices*, Proceedings of IEEE 62 (10) (1974) 1339-1360.

[21] M. Grundmann, *The physics of Semiconductors*, 2nd ed., Springer, pp 524-527.

[22] C. Wang, A. Garcia, D.C. Ingram, M. Lake, M.E. Kordesch, *Cold field emission from CVD diamond films observed in emission electron microscopy*, Electronics Letters 27 (1991) 16, 1459 - 1461.

[23] M. W. Geis, N. N. Efremow, J. D. Woodhouse, M. D. McAleese, M. Marchywka, D. G. Socker, J. F. Hochedez, *Diamond cold cathode*, IEEE Electron device letters 12 (1991) 8, 456-459.

[24] O. Groning, O. M. Kuttel, P. Groning, L. Schlapbach, *Field emission properties of nanocrystalline chemically vapor deposited-diamond films*, Journal of Vacuum Science & Technology B 17 (1999) 1970-1986.

[25] R. Schlesser, M. T. McCarson, Z. Sitar, *Bias voltage dependent field-emission energy distribution analysis of wide band-gap field emitters*, Journal of Applied Physics 82 (1997) 5763.

[26] V.I. Kleshch ,S.T. Purcell & A. N. Obraztsov, *Single Crystal Diamond Needle as Point Electron Source*, Scientific Reports 6 (2016) 35260.

[27] L. M. Baskin, O. I. Lvov, G. N. Fursey, *General Features of Field Emission from Semiconductors*, Physica Status Solidi B 47 (1971) 49–62.

[28] V. Porshyn, V. I. Kleshch, E. A. Obraztsova, A. L. Chuvilin, D. Lützenkirchen-Hecht, and A. N. Obraztsov, *Photoinduced effects in field electron emission from diamond needles*, Applied Physics Letters 110 (2017) 182101.

[29] J. M. Ralston and R. K. Chang, *Optical limiting in semiconductors*, Applied Physics Letters 15 (1969) 164.

[30] M. Grundmann, *The Physics of Semiconductors*, 2nd ed., Springer, pp. 268–269.

[31] A. A. Zolotukhin, M. A. Dolganov, A. M. Alekseev, A. N. Obraztsov, *Single-crystal diamond microneedles shaped at growth stage*, Diamond and Related Materials 42 (2014) 15-20.

[32] A.N. Obraztsov, A.A. Zolotukhin, A.O. Ustinov, A.P. Volkov, Yu. Svirko, *Chemical vapor deposition of carbon films: in-situ plasma diagnostics*, Carbon 41 (2003) 836–839.

[33] E. W. Müller, J. A. Panitz, and S. Brooks McLane, *The Atom-Probe Field Ion Microscope*, Rev. Sci. Instrum. 39 (1968) 83.

[34] A. Modinos, *Field, Thermionic, and Secondary Electron Emission Spectroscopy*, Plenum Press, New York, 1984.

[35] B. Barwick, C. Corder, J. Strohaber, N. Chandler-Smith, C. Uiterwaal and H. Batelaan, *Laser-induced ultrafast electron emission from a field emission tip*, New Journal of Physics, 9 (2007) 142.

[36] D. Venus and M.J.G. Lee, *Polarization dependence of photoexcitation in photofield emission*, Surface science 125 (1983) 452-472.

[37] H. Yanagisawa, C. Hafner, P. Doná, M. Klöckner, D. Leuenberger, T. Greber, J. Osterwalder, and M. Hengsberger, *Laser-induced field emission from a tungsten tip: Optical control of emission sites and the emission process*, Physical review B 81 (2010) 115429.

[38] E. W. Müller, *Das Feldionenmikroskop*. Z Phys 1951;131:136–142.

[39] F. Vurpillot, J Houard, A Vella and B Deconihout, *Thermal response of a field emitter subjected to ultra-fast laser illumination*, J. Phys. D: Appl. Phys. 42 (2009) 125502.

[40] Y.M. Chen, T. Ohkubo, K. Hono, *Laser assisted field evaporation of oxides in atom probe analysis*, Ultramicroscopy 111 (2011) 562-566.

[41] A. Vella, *On the interaction of an ultra-fast laser with a nanometric tip by laser assisted atom probe tomography: A review*, Ultramicroscopy 123 (2013) 5-18.

[42] E. P. Silaeva, L. Arnoldi, M. L. Karahka, B. Deconihout, A. Menand, H. J. Kreuzer, A. Vella, *Do Dielectric Nanostructures Turn Metallic in High-Electric dc Fields?*, Nano Lett., 14 (2014) 6066-6072.

[43] F. Vurpillot, A. Gaillard, G.Da Costa, B.Deconihout, *A model to predict image formation in Atom probeTomography*, Ultramicroscopy 132 (2012) 152-157.

[44] E.P. Silaeva, N. S. Shcheblanov, T. E. Itina, A. Vella, J. Houard, N. Sévelin-Radiguet, F. Vurpillot, B. Deconihout, *Numerical study of femtosecond laser-assisted atom probe tomography*, Appl. Phys. A 110 (2013) 703-707.

[45] H. Tamura, M. Tsukada, K. P. McKenna, A. L. Shluger, T. Ohkubo, and K. Hono, *Laser-assisted field evaporation from insulators triggered by photoinduced hole accumulation*, Physical Review B 86 (2012) 195430.

[46] L. Arnoldi, E. P. Silaeva, A. Gaillard, F. Vurpillot, I. Blum, L. Rigutti, B. Deconihout, and A. Vella, *Energy deficit of pulsed-laser field-ionized and field-emitted ions from non-metallic nano-tips*, Jour. of Appl. Phys. 115 (2014) 203705.

[47] M.I. Landstrass, K.V. Ravi, *Resistivity of chemical vapor deposited diamond films*, Appl. Phys. Lett. 55 (1989) 975.

[48] C.E. Nebel, *Electronic properties of CVD diamond*, Semicond. Sci. Technol. 18 (2003) S1–S11.

[49] H. Pernegger, V. Eremin, H. Frais-Kölbl, E. Griesmayer, H. Kagan, S. Schnetzer, R. Stone, W. Trischuk, D. Twitchen, A. Whitehead, *Charge-carrier properties in*

synthetic single-crystal diamond measured with the transient-current technique, J. Appl. Phys. 97 (2005) 073704.

[50] M. Nesládek, M. van ěček, L. M. Stals, *Defect-Induced Optical Absorption in CVD Diamond Films*, Physica Status Solidi (A) 154 (1996) 283-303.

[51] C.J.H. Wort, R. S. Balmer, *Diamond as an electronic material*, Materialstoday 11 (2008) 22-28.

[52] E. Rohrer, C. F. O. Graeff, R. Janssen, C. E. Nebel, M. Stutzmann, H. Güttler, and R. Zachai, *Nitrogen-related dopant and defect states in CVD diamond*, Physical Review B 54 (1996) 7874.

[53] L.Arnoldi, E.P.Silaeva, F.Vurpillot, B.Deconihout, E.Cadel, I.Blum, A.Vella, *Role of the resistivity of insulating field emitters on the energy of field-ionised and field-evaporated atoms*, Ultramicroscopy 159 (2015) 139-146.

[54] P. Gonon, A. Deneuville, F. Fontaine, and E. Gheeraert, *Electrical conduction and deep levels in polycrystalline diamond films*, J. Appl. Phys. 78 (1995) 6633.

[55] M. Girolami, A. Bellucci, P. Calvani, R. Flammini, and D. M. Trucchi, R*adiation-assisted Frenkel-Poole transport in single-crystal diamond*, Applied Physics Letters 103 (2013) 083502.

[56] Y. Muto, T. Sugino, J. Shirafuji, K. Kobashi, *Electrical conduction in undoped diamond films prepared by chemical vapor deposition*, Appl. Phys. Lett. 59 (1991) 843.

[57] R.S.Sussmann, J.R.Brandon, G.A.Scarsbrook, C.G.Sweeney, T.J.Valentine, A.J.Whitehead, C.J.H.Wort, *Properties of bulk polycrystalline CVD diamond*, Diamond and related materials 3(1994) 303-312.

[58] E. L. Murphy and R. H. Good, *Thermionic Emission, Field Emission, and the Transition Region*, Physical Review 102 (1956) 1464.

[59] R.G.Forbes, *Description of field emission current/voltage characteristics in terms of scaled barrier field values (f-values)*, Journal of Vacuum Science and Technology B. 26 (2008) 209.

[60] R. Gomer, *Field Emission and Field Ionization*. Harvard University Press 1961, Cambridge, Mass.

[61] K. Hadley, M. J. G. Lee, *Influence of shank profile on laser heating of a field emitter*, Journal of applied physics, 57 (1985) 2617–2625.

[62] M. R. Bionta, B. Chalopin, A. Masseboeuf, B. Chatel, *First results on laser-induced field emission from a CNT-based nanotip*, Ultramicroscopy, 159 (2015) 152–155.

[63] M. R. Bionta, S. J. Weber, I. Blum, J. Mauchain, B. Chatel and B. Chalopin, *Wavelength and shape dependent strong-field photoemission from silver nanotips*, New Journal of Physics, 18 (2016) 103010.

[64] M. Marchand, C. Journet, C. Adessi, and S.T. Purcell, *Ring patterns in high-current field emission from carbon nanotubes*, Physical Review B 80, 24 (2009) 245425.

[65] J. Houard, A. Vella, F. Vurpillot and B. Deconihout, *Optical near-field absorption at a metal tip far from plasmonic resonance*, Physical Review B 80 (2010) 125411.

[66] A.Vella, B. Mazumder, G. Da Costa, and B. Deconihout, *Field evaporation mechanism of bulk oxides under ultra fast laser illumination*, Joural of Applied Physics 110, 4 (2011) 044321.

[67] H. Yanagisawa, *Site-selective field emission source by femtosecond laser pulses and its emission mechanism*, Annalen der Physik 525 (2013) 126–134.

[68] H. Yanagisawa, M. Hengsberger, D.Leuenberger, M. Klöckner, C. Hafner, T. Greber, and J. Osterwalder, *Energy Distribution Curves of Ultrafast Laser-Induced Field Emission and Their Implications for Electron Dynamics*, Physical review letters, 107 (2011) 087601.

[69] M. R. Bionta, B. Chalopin, J. P. Champeaux, S. Faure, A. Masseboeuf, P. Moretto-Chapelle, B. Chatel, *Laser-induced electron emission from a tungsten nanotip: identifying above threshold photoemission using energy-resolved laser power dependencies*, Journal of Modern Optics, 61 (2014) 833–838.